UNIVERSITÀ DEGLI STUDI DI PADOVA

DIPARTIMENTO DI INGEGNERIA ELETTRICA

SCUOLA DI DOTTORATO DI RICERCA IN INGEGNERIA INDUSTRIALE
INDIRIZZO ENERGETICA
CICLO XX

Particle transport in Reversed Field Pinch plasmas

Direttore della scuola: prof. Paolo Bariani
Supervisori: prof. Antonio Buffa
ing. Stefano Martini

Dottorando: Fulvio Auriemma

31 gennaio 2008

Se guardo il tuo cielo, opera delle tue dita,
la luna e le stelle che tu hai fissate,
che cosa è l'uomo perché te ne ricordi
e il figlio dell'uomo perché te ne curi?
Eppure l'hai fatto poco meno degli angeli,
di gloria e di onore lo hai coronato:
gli hai dato potere sulle opere delle tue mani,
tutto hai posto sotto i suoi piedi
(Sal 8, 4-7)

a Tania e Toni

Contents

Summary

The standard of living of each human being is determined by many factors: the environment quality, the health, the political and social stability, the richness of his interpersonal relationships, the availability of basic goods like food, drinkable water, clothes, medicine, house, etc. It is quite difficult to quantify all these contributions and, in general, the global quality of life but several studies suggest that one good indicator is the energy consumption pre capita: higher levels of energy availability generally correspond to higher standard of living. From this point of view the energy production for civil purpose is a central issue in the quality of life of the whole mankind. The increase of the energy production were obtained, in the past, burning larger quantity of fuel, such as wood, or more recently, coal, oil and natural gas. Nowadays this is no longer possible: shortage of fossil fuels, climate changes consequent to CO_2 increase in the atmosphere and, above all, the exponential increase in energy demand of developing countries requires to find alternative lines for energy production. At the present time, the basket of energy sources is composed of renewable sources (solar, wind, hydroelectric, geothermal power, to name the most important ones) and no-renewable ones, such as fossil fuels and nuclear power. The renewable sources are CO_2-free but have the disadvantage that they cannot cover the whole world energy demand. Also the nuclear fission technology, that is CO_2-free, presents some problems like the scarcity of Uranium and the radioactive wastes disposal. Hence new energy options must be developed, systems which are optimally safe, environmental and economical friendly. Controlled thermonuclear fusion is one of these rare options.

This thesis is aimed at studying the transport of particles in magnetically confined thermonuclear plasma. The understanding of the transport properties in devices for fusion plasmas is one of the key factor to keep the correct operating conditions in a future fusion reactor. Indeed one of the open issues in magnetic fusion studies, which prevents the realization of an efficient thermonuclear reactor, is the high level of energy and particle transport in the direction perpendicular to the confining magnetic field. This phenomenon reduces confinement properties and has to be solved in order to obtain energy from thermonuclear fusion processes. The amount of particle

and energy transport experimentally observed cannot be interpreted in the framework of the classical theory. Understanding the underlying physics of this *anomalous* transport remains the outstanding critical physical issue in fusion research. Nowadays it is generally accepted that anomalous transport is partially due to magnetic chaos owing to the magnetic perturbations of the equilibrium magnetic fields. The *Reversed Field Pinch* (RFP) configuration, with its wide spectrum of magnetic perturbations, offers a suitable testbed to verify the theory and to reveal the inner mechanism underlying the transport in fusion magnetic devices. The magnetic perturbations, also dubbed *dynamo* or *MagnetoHydroDynamic* (MHD) modes, sustain the RFP configuration against the resistive magnetic diffusion. Unfortunately they have global negative effects: as already stated they lead to the stochastization of the equilibrium magnetic field over a large part of the plasma core and moreover their phase locking generates an interference pattern that results in a global distortion of the plasma column: the so-called *Locked Mode* (LM) that has its maximum effect at a well defined toroidal position. Many techniques have been tested with the aim of reducing the MHD modes. The most effective are the *Pulsed Poloidal Current Drive* (PPCD) that modifies the internal current profile and the active control of the radial field at the edge by means of a system of active coils, the so-called *Virtual Shell* (VS). All the transport mechanisms acting inside the plasma modify the shape of the density profile. The density is measured by means of interferometer: a non-perturbative diagnostic that utilizes electromagnetic waves to probe the plasma.

A part of this thesis will be addressed to determine the global particle diffusion coefficients in relation to the magnetic perturbations amplitude. This analysis has been carried on TPE-RX device: a large RFP machine sited in Tsukuba (Jp). In order to study the global confinement properties, the transport analysis has been carried out analyzing data collected far from to the LM, where its local effect could be neglected. A transport code (in our case TED, acronym of TEmperature and Density) computes the density profile according to transport parameters supplied by the user. The computed profile is compared to the experimental one, determining the correctness of the model assumed to provide the transport coefficients. With this analysis it has been confirmed that damping the MHD modes amplitude by means of the PPCD the particle confinement globally improves and the diffusion coefficient is strongly reduced in the central zone of the plasma. This result has been further confirmed by the density behaviour during pellet injection experiments, where the particles released by the pellet in PPCD discharges are better confined inside the plasma than in plasmas with standard magnetic perturbations.

The dynamo modes, as already stated, generate a global distortion of the *Last Close Flux Surface* (LCFS) of the plasma: the LM. The plasma cross section results shrunk in a wide toroidal region of about 100° and bulging in

another region of the similar toroidal range. Moreover an helical distortion of the column with magnetic lines that directly hit the wall is present. The VS system installed at RFX-mod (the largest RFP device in the world with design maximum plasma current of 2 MA[1], located in Padova) provides an important reduction of the helical perturbation but is less effective on healing the shrinking of the LCFS, highlighting for the first time its effects on plasma confinement. The two toroidal regions with different cross section have been characterized studying the density profile, the density fluctuations and the magnetic fluctuations: the shrunk region shows an improved transport, providing the first experimental evidence of toroidal asymmetric confinement properties in an RFP plasma. Moreover the RFX-mod pulses are affected by spontaneous reorganization of the internal current and magnetic profiles, the so-called *Dynamo Relaxation Events* (DREs). The density behaviour and the magnetic topology during the DREs have been analyzed, confirming the different nature of the shrunk and the bulging region of the plasma.

The thesis is organized as follows:

- Chapter 1: introduces the issue of energy production, highlighting the most important features that a new energy source must have: the thermonuclear magnetic fusion is presented as an effective actor in the future energetic outline. A description of the physics of magnetic confinement equilibria and, with more detail, of the *Reversed Field Pinch* is given, characterizing the effects of the magnetic perturbations on the plasma column and in particular on the confinement properties. The *Reverse Field eXperiemnt* modified (RFX-mod) and the *Toroidal Pinch Experiment* (TPE-RX) are described at the end of the chapter.

- Chapter 2: gives an overview of the transport mechanism acting in a thermonuclear plasma, distinguishing the classical, the neoclassical and the anomalous contribution to transport, with particular attention on the theory of transport in a stochastic magnetic field developed by Rechester and Rosenbluth. Then the most important techniques aiming at reducing the magnetic perturbation are described: the PPCD and the VS system.

- Chapter 3: introduces the diagnostic and the numerical tools needed

[1]SI units are used throughout the thesis, or common derived units, such as centimeters and megampere. The only exception is the temperature usually expressed in electron-volts (eV) in the plasma community. For the sake of comparison, the energy of 1 eV corresponds to a temperature of 11600 K

to carry out transport analyses. The heterodyne interferometric technique, vibrations compensated with a two color system, is explained and the RFX-mod and TPE-RX interferometers are described. Afterwards the numerical tools used in the thesis are described: the inversion code to reconstruct the density profile from the interferometric measurements, the transport code TED to compute the diffusion coefficients and the *Field Line Tracing* FLiT code used to study the magnetic topology.

- Chapter 4: reports the analyses on global confinement properties of TPE-RX plasma, comparing the confinement time and the diffusion coefficient in standard conditions with values obtained in the improved confinement regimes realized by the PPCD technique.

- Chapter 5: describes the experimental evidences of toroidal asymmetric transport properties of the RFX-mod plasma in VS discharges. In particular the analysis on the density profile and on the density and magnetic fluctuations are reported.

- Chapter 6: reports the confinement properties during the DREs in RFX-mod: the particles influx behaviour and the density reaction during the events are described, analyzing also the change in magnetic topology.

- Chapter 7: summarizes the results and gives some conclusions, presenting the future developments.

Riassunto

Lo standard di vita di ciascun essere umano è determinato da molti fattori: la qualità dell'ambiente, la salute, la stabilità politica e sociale, la ricchezza delle sue relazioni interpersonali, la disponibilità di beni basilari come il cibo, l'acqua potabile, i vestiti, i medicinali, la casa, ecc. È piuttosto difficile quantificare tutti questi contributi e, in generale, la qualità di vita globale ma numerosi studi suggeriscono che un buon indicatore è il consumo di energia pro capite: livelli più alti di disponibilità energetica corrispondono generalmente ad uno standard di vita più elevato. Da questo punto di vista la produzione di energia per scopi civili è un punto centrale nella qualità di vita dell'intera umanità. L'aumento della produzione di energia si otteneva, nel passato, bruciando maggiori quantità di combustibile, come il legno e, più recentemente, il carbone, il petrolio e il gas naturale. Al giorno d'oggi questo non è più possibile: la scarsità dei combustibili fossili, i cambiamenti climatici dovuti all'aumento della CO_2 nell'atmosfera e, soprattutto, l'incremento del fabbisogno energetico delle nazioni in via di sviluppo richiedono di trovare linee alternative per la produzione di energia. L'attuale paniere energetico è composto da fonti rinnovabili (il solare, l'eolico, l'idroelettrico, il geotermico, per nominare i più importanti) e da risorse non rinnovabili, come i combustibili fossili e l'energia nucleare. Le fonti rinnovabili non rilasciano CO_2 ma presentano lo svantaggio che non possono coprire l'intero fabbisogno energetico mondiale. Anche l'energia nucleare da fissione, che non genera CO_2, presenta alcuni inconvenienti come la scarsità di uranio e lo stoccaggio delle scorie radioattive. Quindi una nuova opzione per la produzione di energia deve essere sviluppata, un sistema che sia sicuro, ambientalmente sostenibile ed economicamente utilizzabile. La fusione termonucleare controllata è una di queste rare possibilità.

Questa tesi è finalizzata allo studio del trasporto di particelle in plasmi di tipo termonucleare. La comprensione delle proprietà di trasporto nei dispositivi per i plasma da fusione è uno dei fattori chiave per mantenere le corrette condizioni operative in un futuro reattore a fusione. Infatti una delle questioni aperte nello studio della fusione, che impedisce la realizzazione di un reattore termonucleare efficiente, è il livello elevato di trasporto di energia e particelle in direzione perpendicolare al campo magnetico confinante.

Tale fenomeno riduce le proprietà di confinamento e deve essere risolto se si vuole estrarre energia dal processo di fusione termonucleare. Il tasso di perdita di particelle ed energia osservato sperimentalmente non può essere interpretato nel contesto della teoria classica del trasporto. la comprensione della fisica che soggiace a tale trasporto *anomalo* resta un argomento critico e centrale nello ricerca sulla fusione. Attualmente è accettato in generale che il trasporto anomalo sia dovuto in parte al caos magnetico dovuto alle perturbazioni magnetiche ai campi di equilibrio. La configurazione magnetica *Reversed Field Pinch* (RFP), con il suo ampio spettro di perturbazioni magnetiche, offre un letto di prova idoneo a verificare la teoria e a svelare i meccanismi intimi che soggiacciono al trasporto nei dispositivi per la fusione magnetica. Le perturbazioni magnetiche, chiamate anche modi di *dinamo* o modi *magnetoidrodinamici* (MagnetoHydroDynamics, MHD), sostengono la configurazione RFP contrastando la diffusione magnetica resistive. Purtroppo essi hanno degli effetti globalmente negativi: come già affermato producono la stocastizzazione dei campi magnetici di equilibrio in un'ampia zona al centro del plasma ed inoltre il loro bloccaggio in fase produce una figura di interferenza che porta ad una distorsione dell'intera colonna di plasma: il *modo bloccato* (Locked Mode, LM) che presenta il suo massimo effetto in una particolare posizione toroidale. Numerose tecniche sono state provate con l'obiettivo di ridurre i modi MHD. Le più efficaci si sono rivelate essere il *Pulsed Poloidal Current Drive* (PPCD) che modifica i profili interni di corrente e il controllo attivo dei campi magnetici radiali al bordo per mezzo di un sistema di bobine attive, detto *Virtual Shell* (VS). Tutti i meccanismi di trasporto che agiscono all'interno del plasma modificano la forma del profilo di densità di plasma. La densità viene misurata per mezzo dell'interferometro: una diagnostica non perturbativa che utilizza onde elettromagnetiche per sondare il plasma.

Una parte di questa tesi sarà indirizzata a determinare i coefficienti globali di diffusione della particelle in relazione all'ampiezza delle perturbazioni magnetiche. Tale analisi è stata svolta sull'esperimento TPE-RX: una macchina RFP di grandi dimensioni situata a Tsukuba (Giappone). Analisi di trasporto sono state svolte per studiare le proprietà globali di confinamento, analizzando dati misurati lontano dal LM, così da poter trascurare i suoi effetti locali. Un codice di trasporto (chiamato TED nel nostro caso, acronimo di *TEmperature and Density*) calcola il profilo di densità in accordo con i parametri di trasporto forniti dall'utente. Il profilo calcolato è confrontato con il profilo sperimentale, valutando così la correttezza del modello usato per il calcolo dei coefficienti di trasporto. Con questa analisi si è confermato che riducendo le perturbazioni MHD per mezzo del PPCD il confinamento di particelle migliora globalmente e il coefficiente di diffusione è fortemente ridotto nella zona centrale del plasma. Tale risultato è stato ulteriormente confermato del comportamento della densità di plasma durante gli esperimenti di iniezioni di pellet, dove le particelle rilasciate dal

pellet nelle scariche con PPCD sono confinate meglio all'interno del plasma rispetto ai plasmi con perturbazioni magnetiche standard.

I modi di dinamo, come già detto, generano una distorsione dell'ultima superficie di flusso del plasma (*Last Close Flux Surface*, LCFS): il modo bloccato o LM. La sezione trasversale del plasma risulta strizzata in un'ampia zona toroidale di circa 100° e allargata in un'altra regione di ampiezza simile. Inoltre è presente una deformazione elicoidale della colonna, con le linee magnetiche che colpiscono direttamente la prima parete. Il sistema VS presenta ad RFX-mod (il maggior dispositivo di tipo RFP al mondo, con una corrente massima di plasma di 2 MA[2], con sede a Padova) produce una riduzione importante della perturbazioni elicoidale mentre è meno efficace nel curare la strizione della LCFS, evidenziandone per la prima volta gli effetti sul confinamento del plasma. Le due regioni toroidali con diversa sezione sono state caratterizzate studiando i profili di densità, le fluttuazioni di densità e le fluttuazioni magnetiche: la regione strizzata mostra un trasporto aumentato, fornendo così la prima evidenza sperimentale di una asimmetria toroidale nelle proprietà di confinamento di un plasma RFP. Inoltre le scariche di RFX-mod sono affette da eventi di riorganizzazione spontanea dei profili di campo magnetico e di corrente, detti *eventi di rilassamento di dinamo* (Dynamo Relaxation Events, DREs). Sono stati analizzati il comportamento della densità e la topologia magnetica durante i DREs, confermando la differente natura della zona di plasma allargata e di quella strizzata.

La tesi è strutturata secondo il seguente schema:

- Capitolo 1: introduce il problema della produzione di energia, evidenziando le principali caratteristiche che una nuova fonte di energia deve avere: la fusione termonucleare a confinamento magnetico è presentata come un attore importante nel futuro panorama energetico. È fornita la descrizione della fisica degli equilibri magnetici per il confinamento e, con maggior dettaglio del *Reversed Field Pinch*, evidenziando gli effetti delle perturbazioni magnetiche sulla colonna di plasma e in particolare sulle proprietà di confinamento. Alla fine del capitolo sono descritti gli esperimenti *Reverse Field eXperiment modified* (RFX-mod) and the *Toroidal Pinch Experiment* (TPE-RX).

- Capitolo 2: fornisce una visione di insieme dei meccanismi di trasporto che agiscono in un plasma termonucleare, distinguendo il contributo classico, neoclassico ed anomalo, con una particolare attenzione alla

[2]Durante tutta la tesi verrà utilizzato il Sistema Internazionale (SI) di misura eccezion fatta per la temperatura che verrà fornita in electron volts (eV) come d'uso nella comunità fusionistica. Come paragone si tenga conto che l'energia di 1 eV corrisponde ad una temperatura di circa 11600 K

teoria sviluppata da Rechester e Rosenbluth sul trasporto in un campo magnetico stocastico. Dopodiché vengono descritte le tecniche principali per la riduzione delle perturbazioni magnetiche: il PPCD e la Virtual Shell.

- Capitolo 3: presenta la diagnostica e gli strumenti numerici necessari per svolgere un'analisi di trasporto. La tecnica di misura interferometrica in eterodina, con il sistema la compensazione a due colori è spiegata e sono descritti gli interferometri di RFX-mod e di TPE-RX. Dopodiché vengono presentato i codici numerici usati nella tesi: il codice di inversione per ricostruire il profilo di densità dalle misure interferometriche, il codice di trasporto TED per il calcolo dei coefficienti di diffusione e il codice FLiT *Field Line Tracing* usato per studiare la topologia magnetica.

- Capitolo 4: riporta le analisi sulle proprietà globali di confinamento di TPE-RX, confrontando il tempo di confinamento e il coefficiente di diffusione in condizioni standard con i valori ottenuti nei regimi di confinamento avanzato realizzati con la tecnica del PPCD.

- Capitolo 5: descrive le evidenze sperimentali di asimmetrie toroidali nelle proprietà di trasporto del plasma di RFX-mod in scariche con VS. In particolare è riportata l'analisi dei profili di densità e delle fluttuazioni magnetiche e di densità.

- Capitolo 6: descrive le proprietà di confinamento durante i DREs in RFX-mod: sono descritti il comportamento dell'influsso di particelle e la risposta della densità durante gli eventi, analizzando anche i cambiamenti nella topologia magnetica.

- Capitolo 7: riassume i risultati traendone le principali conclusioni e presentando gli sviluppi futuri.

CHAPTER 1

Thermonuclear magnetic controlled fusion.

In this chapter the worldwide problem of energy production for civil purpose is introduced, with some consideration on the characteristic which an energy source for future generations must have. The thermonuclear fusion is presented as an important actor in the energetic basket. The scientific community is doing big efforts to achieve this goal: the ITER project is presented as the next step in fusion research. Then, in more detail, the toroidal magnetic confinement is discussed and the tokamak and RFP magnetic configuration are presented as respectively the main line and an alternative configuration for a future fusion reactor.

1.1 Introduction.

The substantial increase in global energy consumption in the coming decades will be driven principally by the developing world. Today's developing countries (India and China over all), with almost three quarters of the world's inhabitants, consume only one fourth of global energy. Current annual per capita energy consumption differs markedly by country and region: Canada, in the high energy use region of North America, has a per capita consumption close to 8 tonnes of oil equivalent (toe), which is eight times greater than Brazil, where consumption is fifteen times more than in the United Republic of Tanzania or in Bangladesh, as shown in figure 1.1.

Strong economic growth in many developing countries is already leading to sharp increases in per capita energy consumption. Consumption will

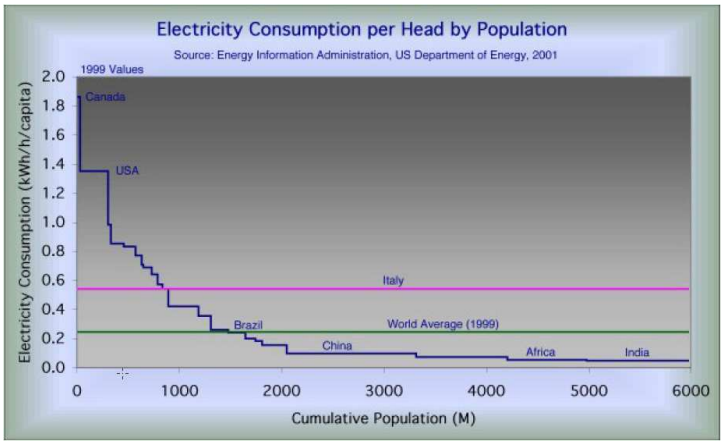

Figure 1.1: Electricity per head in different countries of the world.

continue to rise, driven also by the expected two-fold expansion in world population during the 21^{st} century that will occur in the developing regions.

On the other hand, the increase in energy consumption is limited by availability of non-renewable energy source and environmental constrain. Today, most of the worldwide electricity demand is satisfied by oil (41%), natural gas (22%), coal (16%), nuclear (15%), and renewables (6%). If this pattern does not change, the conventional oil and gas resources will last for approximately 50 years at present levels of consumption. Furthermore, for international political stability, nations will seek electricity supply solutions which allow them to become as independent as possible from the possessors of crucial fuel resources [1]. The large increase of CO_2 emissions over the last century, due to the intense use of traditional fossil flues led to considerable climate changes, resulting in a destabilization of the worldwide climate system. To stabilize CO_2 concentrations in the atmosphere at non dangerous level, the present energy supply system needs to change towards CO_2-free energy sources. Renewable resources will probably contribute much more to the world's energy needs than they do at present, but experts agree that they will not be able to satisfy the total demand [2]. In the past, nuclear energy based on fission has been adopted by many developed and most advanced countries. Technically, the ability to use fission as a longterm energy source has been demonstrated, and the fuel cycle economics and environmental impact are known. The long term wider deployment of fission depends on a full public appreciation of the options and alternatives. A number of countries consider fission a vital element in their current and future electricity supply combination. Anyway many disadvantages are related to fission: the shortage of Uranium that will last approximately for 200 years, the long half life of the radioactive waste that imply a lot of problems about their disposal and, not less important the fact that fission could

develop in a uncontrolled runaway reaction. Therefore new energy options must be developed, systems which are optimally safe, environmental and economical friendly needed. Controlled thermonuclear fusion is one of these rare options [2].

1.2 The thermonuclear fusion.

Thermonuclear fusion is referred to as the nuclear reaction among two light nuclei that fuse into a heavier one, releasing other reaction products such as neutrons. This is a widespread phenomenon in nature. It is well known, for example, that fusion reactions provide a huge source of energy to stars. For roughly seventy years, researchers have also studied the possibility of realizing controlled fusion reactions on Earth to produce energy for peaceful purposes and several encouraging results have been obtained. Two light nuclei can fuse together if they are brought sufficiently close for the short-range attractive nuclear force to overcome the Coulomb repulsion among them. This is possible if the two nuclei collide with high enough kinetic energy. For a significant fraction of fusion reactions to occur, matter has thus to be brought to sufficiently high density and temperature for a sufficiently long time. In such conditions, matter is in the plasma state, a quasi-neutral ensemble of ions and electrons [3]. The main research line to pursuit nuclear fusion on the Earth is the *magnetic confinement fusion*. It uses strong magnetic fields to confine matter in the plasma state. It is well known that a charged particle in a strong magnetic field makes a spiraling motion around the magnetic field lines. In absence of collisions, and by using magnetic closed geometry, it is thus possible to confine plasmas for relatively long times.

The magnetic fusion is the central focus of this thesis. An other important method, not more deeply explained in the following, is the *inertial confinement fusion*: a small amount of solid matter is compress by means of high power source (usually lasers or ion beams) that hit it from many direction, bringing it to the critical condition to activate the fusion reaction.

1.2.1. Energy from thermonuclear fusion reactions.

The most promising fusion reactions involve light nuclei such as Deuterium (^2_1D), Tritium (^3_1T) and Helium ^3_2He. Examples of fusion reaction are:

$$\begin{array}{lcl} {}^2_1D + {}^2_1D & \rightarrow & {}^3_2He + {}^1_0n + 3.3\,\text{MeV} \\ {}^2_1D + {}^2_1D & \rightarrow & {}^3_1T + {}^1_1p + 4.0\,\text{MeV} \\ {}^2_1D + {}^3_2He & \rightarrow & {}^4_2He + {}^1_1p + 18.4\,\text{MeV} \\ {}^2_1D + {}^3_1T & \rightarrow & {}^4_2He + {}^1_0n + 17.6\,\text{MeV} \\ {}^3_1T + {}^3_1T & \rightarrow & {}^4_2He + 2{}^1_0n + 11.3\,\text{MeV} \end{array} \tag{1.1}$$

The fusion rates of the above reaction are shown in figure 1.2. The ${}^2_1D + {}^3_1T$ reaction has the highest reaction rates at lower temperature (E $\lesssim 20$ keV) hence it is the best choice for a fusion reactor.

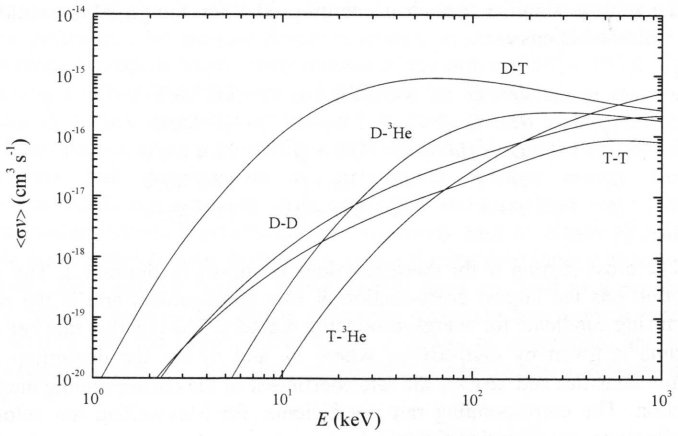

Figure 1.2: Fusion reaction rate $\langle \sigma v \rangle$ for couples of reactants.

Deuterium resources on Earth are practically endless, 0.0015% of hydrogen atoms in water being deuterium, even though extraction methods are not yet affordable. Tritium is also an isotope of hydrogen, but it occurs naturally in only negligible amounts due to its radioactive half-life of only 12.3 years. Tritium can be obtained from the two following reactions with lithium:

$$\begin{aligned} {}^6_3Li + {}^1_0 n &\rightarrow {}^3_1T + {}^4_2He + 4.8\,\text{MeV} \\ {}^7_3Li + {}^1_0 n &\rightarrow {}^3_1T + {}^4_2He + {}^1_0 n - 2.5\,\text{MeV} \end{aligned}$$

The adoption of a lithium blanket on the vacuum vessel of fusion reactors should be adequate to provide the necessary tritium source for an unlimited period of time, based on the present lithium resources. Compared to fossil fuel power plant, there is no production of greenhouse gases, since the main natural product of the fusion reaction is helium, which is completely harmless to life and does not contribute to global warming. In addition in a fusion reactor, unlike in a fission one, there is no risk of uncontrolled runaway of the reaction.

1.2.2. The burning criteria.

For the energy balance of a fusion reactor to be positive, the energy produced by fusion reactions has to exceed that required to create and sustain the plasma itself. One form of energy loss for a ${}^2_1D - {}^3_1T$ plasma with electron density $n_e (n_D = n_T = n_e/2)$ and temperature T_i is bremsstrahlung radiation

[3]. The power lost per unit volume due to bremsstrahlung emission is $P_b = bn^2T^{1/2}$, where b is a function of the effective charge $Z_{\text{eff}} = n_i^{-1}\Sigma_i n_i Z^2$ in a multi-species plasma. In addition, power losses due to confinement degradation, e.g. through collisional and turbulent transport phenomena, have to be considered in the power balance. A simple estimate of the energy losses due to mechanisms different from bremsstrahlung can be made as $P_t = 3nT/\tau_E$, by introducing the average energy confinement time τ_E. The power generated by fusion reactions can be written as $P_n = W_{DT}n^2\frac{\langle\sigma v\rangle_{T_i}}{4}$, where $W_{DT} = 17.6\,\text{MeV}$ is the energy released after a single $D-T$ reaction and $\langle\sigma v\rangle_{T_i}$ is the $D-T$ fusion reaction rate, that is function of the temperature T_i. Assuming that the reaction power P_n can be convert in electric power with an efficiency η then re-injected in the reactor in order to balance the energy losses, the self-sustainment condition is:

$$P_b + P_t \leq \eta(P_b + P_t + P_n) \tag{1.2}$$

which can be rewritten as:

$$n\tau_E \geq 3T\left(\frac{\eta}{1-\eta}\frac{W_{DT}}{4}\langle\sigma v\rangle_{T_i} - b\sqrt{T_i}\right)^{-1} \tag{1.3}$$

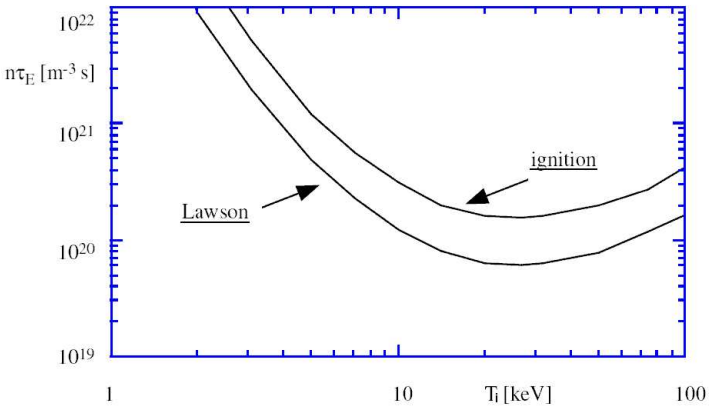

Figure 1.3: The minimum $n\tau_E$ curves for which the Lawson's and ignition criteria are satisfied. The Lawson's curve refers to an efficiency $\eta = 30\%$.

This last expression is also known as Lawson's criterion [4]. The right end side of equation 1.3 depends only on temperature, hence the product $n\tau_E$ where the equality is satisfied can be plotted as a function of T_i. In figure 1.3, the curve with efficiency $\eta = 30\%$ is reported, which has a minimum at $T_i \simeq 20\,\text{keV}$.

The most probable reactor scenario is one in which the α particles (^4_2He nuclei) produced by fusion reactions are confined by the magnetic field, and

replace all the energy losses by transferring their energy to the plasma, whereas neutrons escape the plasma volume and their energy is converted to electric energy. In this case the Lawson's criterion must be modified, it is called ignition criterion and is written as $P_b + P_t \leq P_\alpha$ which can be expressed as:

$$n\tau_E \geq 3T \left(\frac{W_\alpha}{4} \langle \sigma v \rangle_{T_i} - b\sqrt{T_i} \right)^{-1} \tag{1.4}$$

where $W_\alpha = W_{DT}/5$ is the energy of a single α particle after a fusion reaction. The $n\tau_E$ curve that corresponds to the equality is shown in figure 1.3. As the Lawson's criterion curve, the ignition curve has a minimum at $T_i \simeq 20$ keV. Isolating the temperature dependence in the right term of equation 1.4 we obtain the classical form of the so called *triple product*:

$$n\tau_E T_i \geq 3 \cdot 10^{21} \mathrm{m}^{-3} \text{ s keV} \tag{1.5}$$

For temperatures $T_i \simeq 20$ keV and electron densities $n_e \simeq 10^{20}\mathrm{m}^{-3}$, which are expected in a fusion reactor, the energy confinement time τ_E must be grater than 1s.

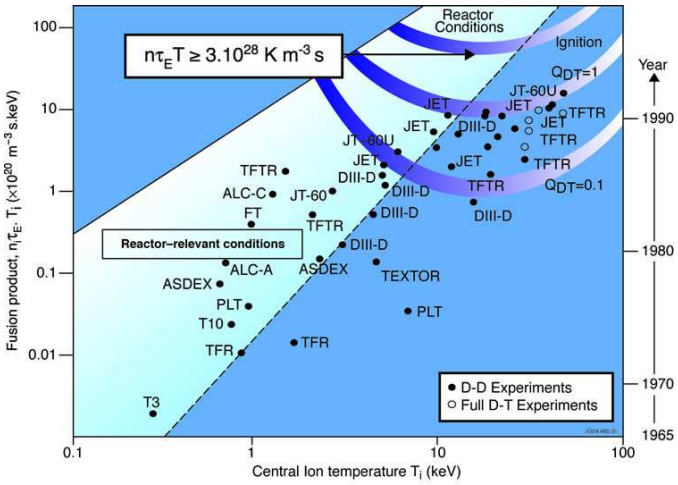

Figure 1.4: Values of the fusion triple product obtained in experiments as a function of the central ion temperature T_i.

Figure 1.4 shows the values of the triple product reached in fusion devices since the beginning of experiment in plasma physics. The clear trend shows the improvement in confinement achieved up to now and the goal that the scientific community must reach to provide a fusion power plant to the world. In paragraph 1.2.3, a description of the ITER project will be given to show which goal the fusion community is aiming at.

1.2.3 ITER: International Thermonuclear Experimental Reactor

1.2.3. ITER: International Thermonuclear Experimental Reactor

The large experimental database obtained in the last thirty years magnetic confinement device, and the improving capability of numerical simulations have provided the international community the physics basis for the design of a burning plasma experiment based on the tokamak concept, which is called International Thermonuclear Experimental Reactor (ITER). The principal physics goals of ITER are:

- to achieve extended burn in inductively-driven plasmas with $Q = Q_{fus}/Q_{aux}$ (fusion power over auxiliary power) of at least 10 for a range of operating scenarios and with a duration sufficient to achieve stationary conditions;

- to aim at demonstrating steady state operation using non-inductive current drive with a ratio of fusion power to input power for current drive of at least 5. In addition, the possibility of higher Q operation will be explored if favorable confinement conditions can be achieved.

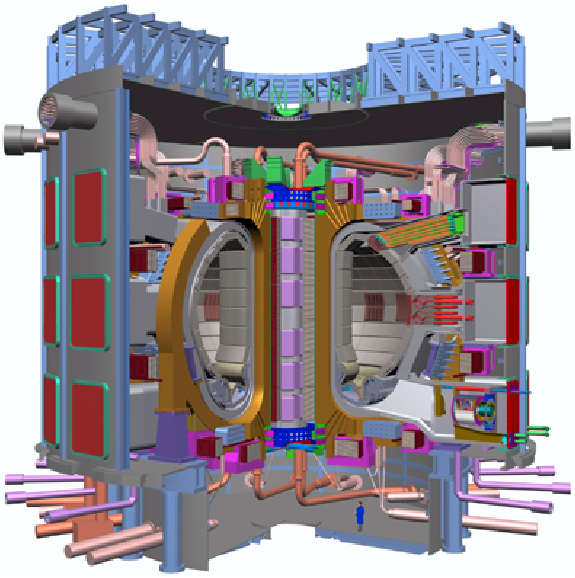

Figure 1.5: Schematic overview of the International Thermonuclear Experiment Reactor.

The ITER nominal fusion power output will be about 500MW. To achieve this goal, the main frame of the project is the following: a major radius $R_0 = 6.2m$, minor radius $a = 2m$, maximum magnetic field $B = 5.3T$ and plasma current $I_p = 15MA$. The discharge duration is designed to be about 400 seconds, which can be regarded as a stationary condition on the time scales characteristic of the plasma processes. All of these parameters have

been predicted for plasmas with density $n_e \approx 10^{20}$ m^{-3} and core electron and ion temperatures $T_e \approx 8.8$ keV and $T_i \approx 8$ keV respectively. ITER would explore many reactor relevant scientific and technological issues, which are beyond the present experimental capabilities. In particular, regimes in which the α particles contribute significantly to the plasma pressure are very interesting. In these conditions a class of plasma instabilities are predicted to be driven by the α particles, which can partially be studied in the present tokamaks. The study of plasma instabilities and their control is only one aspect of the research in burning scenarios. A variety of technological issues could also be studied in ITER, like for example the test of advanced materials facing very large heat and particle fluxes, the test of concepts for a tritium breeding module, the superconducting technology under high neutron flux and many others. The auxiliary systems needed to achieve the conditions expected in ITER are an external heating and current drive capability of about 73MW and several advanced diagnostics for both analysis and plasma control. All of these requirements are expected to solve many of the scientific and engineering issues concerning a burning plasma, and could allow us to make a significant next step towards the demonstration of a tokamak power-plant. A schematic view of ITER is displayed in figure 1.5.

1.3 The magnetic confinement.

Several magnetic field geometries have been investigated for many years in fusion research to seek the best conditions for plasma confinement. Examples are magnetic mirrors, linear and toroidal configurations, and many others. Up to now, the toroidal geometry has given the best confinement performances. This Section will be dedicated to a brief introduction to the principles of magnetic plasma confinement in toroidal devices, and in particular in the so called tokamak and reversed-field pinch (RFP [5]) configurations. We define in figure 1.6 the toroidal coordinates $(r;\theta;\phi)$, which

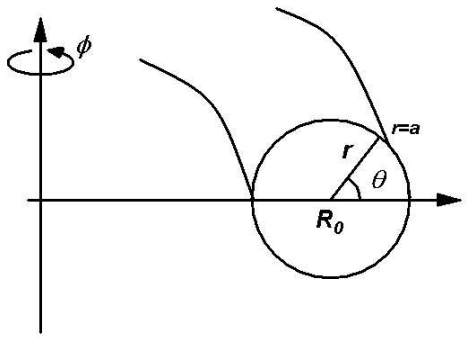

Figure 1.6: The coordinates system $(r;\theta;\phi)$ in toroidal geometry.

will be used in the rest of the thesis: r is called radial coordinate, θ and ϕ are the poloidal and toroidal angles, respectively. With R_0 and a we indicate the major and minor radius of the torus, respectively. Magnetic field lines in toroidal experiments have both a poloidal component B_θ (or sometimes B_p), which is mainly generated by an externally driven toroidal plasma current j_ϕ, and a toroidal component B_ϕ (or B_t), which in some configurations is only in part produced by currents flowing in external conductors. Magnetic field lines are thus helixes, which wind around the torus lying over toroidal surfaces called magnetic surfaces. Helical magnetic field lines are described by the so called *safety factor* q, which is defined as a function of radius as follows:

$$q(r) = -\frac{r}{R_0}\frac{B_\phi(r)}{B_\theta(r)} \tag{1.6}$$

The inverse of this quantity represents the number of poloidal turns done by a helical field line per one toroidal turn. The name safety factor comes from the fact that this quantity is crucial to determine several features of the plasma stability.

1.3.1. The MHD theory.

A large variety of plasma properties, such as the magnetic equilibria or several instabilities associated with them, can be described using a fluid model called *resistive MagnetoHydroDynamics* (MHD) [6].A brief introduction to this theory is given in the following. In the two-fluid MHD, where the two plasma is described as composed by ions and electrons, the mass and momentum continuity equations can be written as follows:

$$\frac{\partial \rho_\alpha}{\partial t} + \nabla \cdot (\rho_\alpha \boldsymbol{u_\alpha}) = 0 \tag{1.7}$$

$$\rho_\alpha \left(\frac{\partial \boldsymbol{u_\alpha}}{\partial t} + \boldsymbol{u_\alpha} \cdot \nabla \boldsymbol{u_\alpha} \right) = \sigma_\alpha \boldsymbol{E} + \boldsymbol{j} \times \boldsymbol{B} - \nabla p_\alpha + R_{\alpha\beta} \tag{1.8}$$

where $\alpha, \beta = i, e$ (i.e. ions or electrons), $\rho_\alpha = m_\alpha n_\alpha$ is the mass density, and $\sigma_\alpha = \pm e n_\alpha$ is the charge density of the single species. No particle or momentum sources are considered here for simplicity. The electromagnetic quantities $\boldsymbol{E}, \boldsymbol{B}$, and $\boldsymbol{j}$ have the usual meaning. The first two terms in the right hand side of equation 1.8 represent the electromagnetic forces, $-\nabla p_\alpha$ is the kinetic pressure force and $R_{\alpha\beta}$ is the rate at which momentum is gained or lost by species α due to collisions with species β.

A plasma can be described as a single fluid by introducing the following variables: the mass density $\rho = \rho_i + \rho_e$, the kinetic pressure $p = p_i + p_e$, the mass fluid velocity $\boldsymbol{u} = (\rho_i \boldsymbol{u_i} + \rho_e \boldsymbol{u_e})/\rho$, and the charge density $\sigma = e(n_i - n_e)$. By combining the two-fluid equations 1.7 and 1.8 and by using

the above relations, it is simple to derive the following fluid equations:

$$\frac{\partial \rho}{\partial t} + \nabla \cdot (\rho \boldsymbol{u}) = 0 \tag{1.9}$$

$$\rho \left(\frac{\partial \boldsymbol{u}}{\partial t} + \boldsymbol{u} \cdot \nabla \boldsymbol{u} \right) = \sigma \boldsymbol{E} + \boldsymbol{j} \times \boldsymbol{B} - \nabla p \tag{1.10}$$

$$\boldsymbol{E} + \boldsymbol{u} \times \boldsymbol{B} = \eta \boldsymbol{j} - \frac{\boldsymbol{j} \times \boldsymbol{B} - \nabla p_e}{ne} \tag{1.11}$$

Equation 1.9 is the mass continuity equation, equation 1.10 is the momentum continuity equation, also called single-fluid equation of motion, and equation 1.11 is the generalized Ohm's law, which is not strictly a single-fluid equation due to the presence of the ∇p_e term. What is usually referred to as *resistive MHD model* can be derived by the fluid equations 1.9, 1.10 and 1.11 under the following two approximations:

1. charge quasi-neutrality, $n_i \simeq n_e$, which permits to drop the term $\sigma \boldsymbol{E}$ in equation 1.10

2. small ion Larmor radius compared with the scale-length of the fluid motion, which causes the Hall and diamagnetic terms ($\frac{\boldsymbol{j} \times \boldsymbol{B} - \nabla p_e}{ne}$) in Ohm's law to be negligible with respect to the other terms.

The latter set of single fluid equation, combined with the Maxwell equations and a closure term for the heat flux, describes the behaviour of the plasma in a magnetic field. The heat flux is usually modeled by an equation of state for pressure of the form $p \propto n^\gamma$. The exponent γ can be chosen depending on the phenomena to be modeled. For example, $\gamma = 1$ represents isothermal compression and $\gamma = 5/3$ adiabatic compression. By combining Faraday's law ($\nabla \times \boldsymbol{E} = -\frac{\partial \boldsymbol{B}}{\partial t}$) with Ohm's law, it is simple to derive the following equation, which describes the coupled dynamics of the magnetic and fluid velocity fields in the resistive MHD framework:

$$\frac{\partial \boldsymbol{B}}{\partial t} = \nabla \times (\boldsymbol{u} \times \boldsymbol{B}) + \frac{\eta}{\mu_0} \nabla^2 \boldsymbol{B} \tag{1.12}$$

The first term on the right-hand side in equation 1.12 describes convection of the magnetic field with the plasma, and its amplification or reduction due to compressive motion perpendicular to the magnetic field. Starting from this equation, it is possible to show that, in the ideal MHD limit, i.e. in the case where the resistivity η is negligible, the magnetic field lines move like if they were frozen into the plasma. The second term describes instead resistive diffusion of the field across the plasma.

Magnetic surfaces

A magnetic surface is a surface which is ergodically covered by a magnetic field line as it goes around the torus. Between these surfaces we can identify some special magnetic surfaces, the so called *rational surfaces*,which are characterized by the fact that their field line close upon themselves after one or several transit around the machine. In toroidal geometry the magnetic surfaces are nested whose cross-section in a poloidal plane forms a set of smooth closed curves. The degenerate magnetic surface with the limiting zero values is called the *magnetic axis* (fig 1.7).

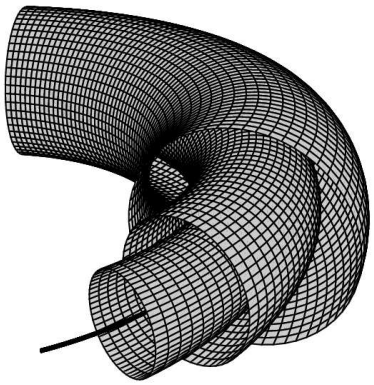

Figure 1.7: Magnetic surfaces and magnetic axis in toroidal geometry owing to the equilibrium fields.

Well defined nested magnetic surfaces are usually taken to be a requirement for adequate plasma equilibrium as described by MHD equation:

$$\boldsymbol{j} \times \boldsymbol{B} = \nabla p \tag{1.13}$$

These magnetic surfaces are constant pressure surfaces, since $\boldsymbol{B} \cdot \nabla p = 0$ and the current-density lines lie on these surfaces because $\boldsymbol{j} \cdot \nabla p = 0$.

A figure of merit for magnetic confinement is the so called β parameter, a dimensionless number introduced to estimate how much kinetic plasma pressure p is balanced by the magnetic field pressure:

$$\beta = \frac{p}{B^2/2\mu_0} \tag{1.14}$$

The toroidal or the poloidal magnetic field separately can be used in the above definition, and in this case the β parameter is called poloidal β_θ or toroidal β_ϕ respectively.

1.3.2. Perturbation to the equilibrium

The MHD equations introduced in paragraph 1.3.1 predict that under certain conditions a small perturbation in a fluid quantity, like for example the

density, the fluid velocity, or the magnetic field, can grow unstable in time. These phenomena are called MHD instabilities [17]. They are present also in toroidal fusion devices, where they influence in many ways the global plasma properties, and can deteriorate the plasma confinement performances. A perturbation $\tilde{\boldsymbol{A}}$ of a quantity $\boldsymbol{A}$ in a toroidal plasma can be Fourier analyzed as follows:

$$\tilde{\boldsymbol{A}}(r,t) = \sum_k \tilde{A}_k(r) e^{i(\boldsymbol{k}\cdot\boldsymbol{r}-\omega t)} = \sum_k \tilde{k}(r) e^{i(m\theta+n\phi-\omega t)} \tag{1.15}$$

where $\boldsymbol{k} = (k_r, k_\theta, k_\phi) = (k_r, m/r, n/R0)$ is the wavevector in toroidal coordinates, and m and n are the poloidal and toroidal mode number, respectively. Each couple (m; n) represents a helical perturbation, or mode. The angular frequency ω is in general a complex quantity, $\omega = \omega_R + i\omega_I$, of which the real part describes the propagation velocity, while the imaginary part represents an exponential growth ($\omega_I > 0$), or damping of the perturbation amplitude ($\omega_I < 0$). A helical magnetic perturbation with wavevector $\boldsymbol{k}$ can become unstable if it fulfills the resonance condition $\boldsymbol{k}\cdot\boldsymbol{B} = 0$, where $\boldsymbol{B} = (0, B_\theta, B_\phi)$ is the equilibrium magnetic field. In fact, a perturbation with $\boldsymbol{k}\cdot\boldsymbol{B} \neq 0$ would bend the mean magnetic field, and it would be thus energetically unfavored. The above resonance condition can be rewritten as follows:

$$\boldsymbol{k}\cdot\boldsymbol{B} = \frac{m}{r}B_\theta + \frac{n}{R_0}B_\phi = 0 \quad \rightarrow \quad q(r) = -\frac{r}{R_0}\frac{B_\phi(r)}{B_\theta(r)} = -\frac{m}{n} \tag{1.16}$$

This shows that helical instabilities can grow only at radial positions where the safety factor assumes rational values. For this reason, these positions are called rational or resonant radii. Like in neutral fluids, a plasma instability can be driven, for example, by a thermal gradient. Under certain conditions, this can provide the necessary free-energy for a whatever small perturbation to grow unstable. But also many other driving terms can be present in plasmas. An important example is given by the so called tearing mode [7], which is driven unstable by a gradient in the current density parallel to the magnetic field. The name of this instability comes from the fact that the magnetic field lines tear and reconnect during its evolution. It is possible to show that, when this gradient is sufficiently high, a tearing instability is triggered, which causes the magnetic field lines to bend and reconnect. The resultant magnetic configuration is characterized by the formation of a so called *magnetic island*. We do not add here more details on this instability. In the following Chapters, we will show that tearing modes play an important role in toroidal plasma dynamics, and particularly in the RFP, affecting its global confinement properties.

1.3.3. The tokamak and RFP equilibria.

Several toroidal configurations have been investigated in fusion research, which are characterized by different magnetic field and safety factor profiles, instability behavior, and maximum attainable β values at comparable input power. We will focus here on two such configurations, i.e. the tokamak [8] and the RFP [9]. The latter will be the main subject of this thesis. The tokamak and the RFP are similar under many aspects. In particular, they both belong to the class of toroidal pinch devices, in which a toroidal current is inductively driven by an external circuit, and generates a poloidal magnetic field that confines and compresses the plasma [6]. In both cases, the toroidal magnetic field is in part generated by external coils. But these two configurations have also some important differences, both in the basic physics processes underlying their dynamics and in more technical aspects. A description of them is presented in the following.

- Tokamak. This configuration is characterized by a relatively strong toroidal magnetic field B_ϕ and a much weaker poloidal magnetic field $B_\theta \simeq B_\phi/10$. The toroidal magnetic field can reach values up to 8T in high-field machines, like for example FTU in Rome (Italy). Superconducting coils are often needed to produce such strong magnetic fields for long tokamak operation, which represents a severe technological issue for future tokamak reactors. Given these magnetic profiles, the tokamak safety factor usually increases monotonically with the radial coordinate r, with typical values greater or close to unity in the core. For stability requirements tokamak operation is preferable at $q > 1$, which is called Kruskal- Shafranov limit. When a rational surface $q = 1$ is present in the plasma, a strong $(m = 1; n = 1)$ kink instability can grow unstable. This has usually a strong sawtooth dynamics, which causes severe confinement losses, and in some cases it can even produce violent current disruptions, which can severely damage the vessel components, especially at high current operation. Other types of safety factor profiles have been studied in advanced tokamak operation, like for examples non-monotonic dependencies, which uses magnetic and flow shear to stabilize the plasma instabilities and achieve enhanced confinement conditions [8]. We will not further enter these issues here. The Kruskal-Shafranov limit imposes a limitation on the maximum achievable plasma current and related Ohmic heating in tokamaks, so that additional complex heating methods, like for example neutral beam or radiofrequency heating, are needed to reach thermonuclear conditions.

- Reversed Field Pinch (RFP). The Reversed Field Pinch (RFP) magnetic configuration is a near minimum energy state to which the plasma spontaneously relaxes [10]. The force-free part of the magnetic field

distribution is described by $\nabla \times \boldsymbol{B} = \mu \boldsymbol{B}$, where μ describes the parallel component of the current density, $\boldsymbol{j}$, as $\mu = \mu_0 \boldsymbol{j} \cdot \boldsymbol{B}/B^2$. In the fully relaxed minimum energy state described by Taylor μ is uniform across the plasma, the plasma kinetic pressure is zero and the magnetic field profiles are given, by the zero- and first-order Bessel functions:

$$B_\theta = B_0 J_1(\mu r) \qquad\qquad B_\phi = B_0 J_0(\mu r) \tag{1.17}$$

Differently from the tokamak, the strength of the toroidal and poloidal components of the magnetic field in the RFP is comparable and relatively weak, $B_\theta \simeq B_\phi$, as shown in 1.8. These relatively weak mag-

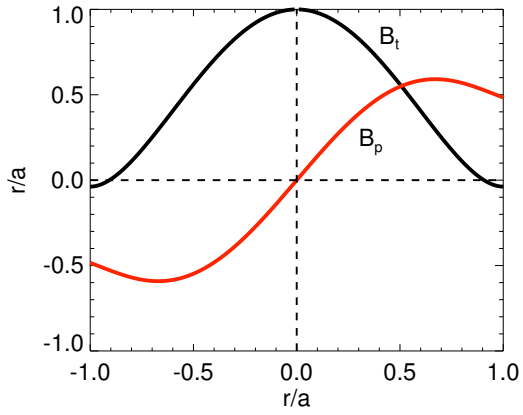

Figure 1.8: sketch of RFP equilibria magnetic fields radial profiles. The toroidal field B_t is displayed in black, whereas the poloidal B_p one is in red.

netic fields imposes less demanding technological issues in this device, which for example does not need in principle superconducting coils. The name RFP comes from the fact that the toroidal magnetic field reverses its sign near the plasma edge. As a consequence, the safety factor profile also changes its sign at the same radius, as shown in figure 1.9. Related to the equilibrium magnetic field, we introduce for future reference two dimensionless parameters that are often used to characterize the equilibria. These are the so called *pinch parameter* Θ and the *reversal parameter* F, and are defined as follows:

$$\Theta = \frac{B_\theta(a)}{\langle B_\phi \rangle} \qquad\qquad F = \frac{B_\phi(a)}{\langle B_\phi \rangle} \tag{1.18}$$

where the brackets indicates an average over the poloidal cross-section. In terms of these quantities, the tokamak is typically a low Θ device with $F > 0$, while the RFP is a relatively high Θ configuration, with $F < 0$.

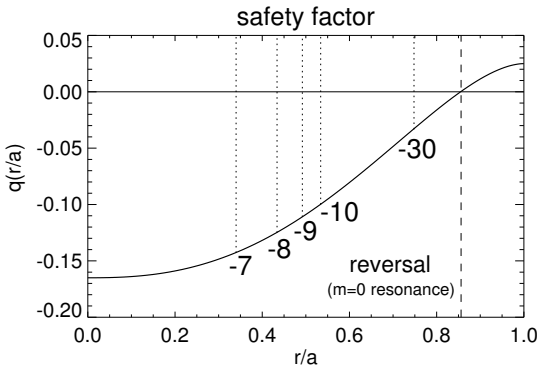

Figure 1.9: RFP safety factor radial profile. The resonance of the some m = 1 modes and the reversal surface are displayed.

The RFP is an intrinsically low safety factor device. For this reason, a broad spectrum of $(m = 1; |n| \leq 2R_0/a)$ magnetic modes is resonant throughout the plasma radius, and several $(m = 0;\ n \geq 1)$ modes are resonant at the reversal radius. This has many consequences on the dynamics of this configuration and on its transport properties due to the stochastization of magnetic field, as we will see in chapter 2. Moreover the presence of the MHD perturbation to the equilibrium magnetic field generates a distortion of the *Last Close Flux Surface*(LCFS) of the plasma: the unperturbed magnetic surfaces (fig. 1.7) are shrunk and enlarged by the m = 0 modes whereas the m =1 modes generates an helical deformation, as shown in figure 1.10.

Different from what happens in tokamaks, low safety factor operation in the RFP does not bring to dangerous disruptive behavior. This is due to the combined action of a high level of magnetic shear, which characterizes this configuration and has a strong stabilizing function on the magnetic modes, and to the presence of a conducting shell, which passively reacts against growing magnetic perturbations.

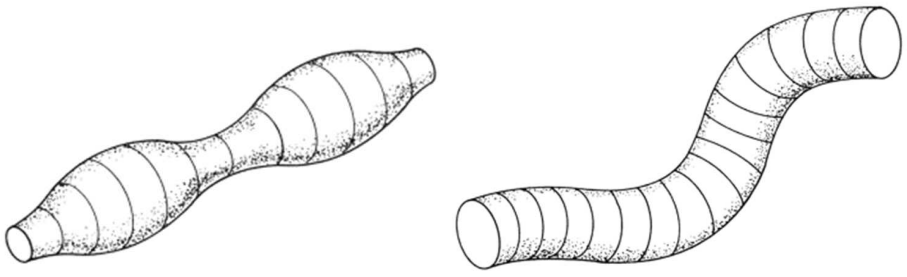

Figure 1.10: m = 0 (left) and m = 1 (right) deformations of the LCFS owing to the presence of a single mode.

For all the above reasons, the plasma current in the RFP is not limited by the Kruskal-Shafranov limit, as it happens in tokamaks. As an effect, the RFP can operate at plasma currents about ten times larger than in tokamaks, and it can reach $\beta \simeq 10\%$ through Ohmic heating only. In principle, ignition could be reached in the RFP through Ohmic heating only, and additional heating sources should not be needed, which represents an important advantage of this configuration.

A strong limit to the plasma current in the present RFP devices is the plasma wall interaction related to a characteristic behaviour of the magnetic modes: the so called *Locked Mode*.

1.3.4. Locking in phase and at the wall of the tearing mode: the Locked Mode (LM).

The modes dynamics are strongly related between themselves: in particular the phasing of the $m = 0$ and $m = 1$ modes produces an interference pattern known as *Locked Mode* or *Slinky Mode* [11, 12] that could be seen as a stationary deformation of the plasma column. Moreover, due to the braking torque entailed by the interaction of its radial fields with metal liner and stabilizing shell, the magnetic modes, and the LM as well, lock to the wall. The deformation of the LCFS is given by the sum of the deformation due to phasing of $m = 0$ modes and of the $m = 1$ component, as displayed in figure 1.11.

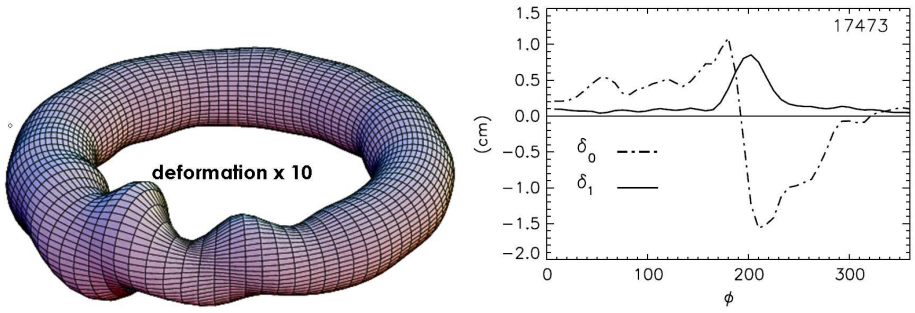

Figure 1.11: Left: Deformation (× 10) of the LCFS in a RFP owing to the locking in phase of $m = 0$ and $m = 1$ modes. Right: δ_0 and δ_1 toroidal profile. The ϕ_{lock} is the angle where the δ_1 reaches its maximum.

The distortion of the LCFS caused by the locking in phase of $m = 1$ modes can be represented as a non uniform, non-axisymmetric shift δ_1 that follows a helical path. The toroidal angle where δ_1 assumes its maximum value identifies the LM position ϕ_{lock}. The amplitude of δ_1 is significant in an interval of about 40 toroidal degrees around ϕ_{lock}, while it is negligible elsewhere. The deformation of the plasma column due to $m = 0$ modes

is observed as a bulging of the plasma radius δ_0 [13]. Both δ_0 and δ_1 are functions of the toroidal angle and in figure 1.11 an example of their toroidal profile is shown.

In RFX-mod the plasma column is usually enlarged at toroidal angles $\phi \leq \phi_{\text{lock}}$ and the maximum value is located at an angle very close but smaller than ϕ_{lock}. The bulging has a negative jump in correspondence to ϕ_{lock}; hence in the region at $\phi \geq \phi_{\text{lock}}$ the plasma column is shrunk.

1.3.5. The dynamo process.

If the RFP were dominated by resistive diffusion, the discharge duration would be limited in time. In fact the RFP, as a static conductor subjected to resistive diffusion, is described by the following equation:

$$\frac{\partial \boldsymbol{B}}{\partial t} = \frac{\eta}{\mu_0}\nabla^2 \boldsymbol{B} \tag{1.19}$$

Solution of the latter equation in cylindrical geometry for the toroidal and poloidal component of the magnetic field are:

$$B_\phi(t) = B_\phi(0)e^{-t/\tau} \tag{1.20}$$

$$B_\theta(t) = B_\theta(0)e^{-t/\tau} \tag{1.21}$$

It is worth noting that such solutions preserve the radial shape of the field; only its amplitude is varying in time, so that the stability properties of the configuration remain unchanged in time. In any case it is experimentally observed that a RFP discharge lasts much longer than the resistive diffusion time. In particular it has been proved that the reversed field configuration is maintained as long as the toroidal current lasts. This suggests that some mechanism is necessary to regenerate the magnetic field continuously lost through resistive diffusion. This mechanism is called *dynamo* [9, 14]. To understand the dynamo mechanism, let us consider the Ohm's law 1.11, and in particular its parallel form:

$$\frac{(\boldsymbol{E} + \boldsymbol{u} \times \boldsymbol{B}) \cdot \boldsymbol{B}}{B} = E_{||} = \eta j_{||} \tag{1.22}$$

Writing the magnetic and velocity fields as a sum of a mean-field plus a fluctuation term, $\boldsymbol{B} = \boldsymbol{B_0} + \tilde{\boldsymbol{b}}$ and $\boldsymbol{u} = \boldsymbol{u_0} + \tilde{\boldsymbol{u}}$, a new mean-field electric field term arises in the parallel Ohm's law, which is called dynamo electric field E_d, and is given by the coherent interaction of the velocity and magnetic field fluctuations:

$$E_{||} + E_d = E_{||} + < \tilde{\boldsymbol{u}} \times \tilde{\boldsymbol{b}} > = \eta j_{||} \tag{1.23}$$

The magnetic fluctuations, hence, appear to be a necessary ingredient in order to sustain the RFP magnetic configuration against the resistive diffusion: for this reason they are also dubbed *dynamo modes*.

1.4 Experimental devices

The main RFPs experiment presently at work in the world are:

- Extrap-T2R in Stockholm [15]: a relative small RFP device characterized by a high aspect ratio $R_0/a = 1.24m/0.183m \simeq 6.8$ and relatively low plasma currents ($I_p = 100\,\mathrm{kA}$).

- Madison Symmetric Torus [16], MST (Madison,Wisconsin,USA); aspect ratio $R_0/a = 1.5m/0.52m \simeq 3$ and plasma currents up to 600kA.

- Toroidal Pinch Experiment [17], TPE-RX (Tsukuba, Japan); aspect ratio was $R_0/a = 1.72m/0.45m \simeq 3.8$, intermediate between that of RFX and MST, operating to maximum plasma currents $I_p = 500\,\mathrm{kA}$.

- Reversed Field eXperiment modified [18], RFX-mod (Padova, Italy); the largest RFP device in the world, $R_0/a = 2m/0.459m \simeq 4.4$ with plasma currents up to 2 MA.

In this thesis we shall consider data from the RFX-mod experiment and TPE-RX. This is why we give in the following of this section a detailed description of these two devices and of their main features.

1.4.1. RFX-mod: Reversed Field eXperiment-modified.

The current RFX-mod device (see fig.1.12) is an upgraded version of the old experiment RFX [19]. Many features have been modified in the new device but, undoubtedly, the most important are the new power supply system and the set of 192 independently driven saddle coils aimed at actively controlling and contrasting local radial perturbations at the edge, as it will be explained in the following.

The main technical components in RFX-mod are:

vacuum vessel : the toroidal chamber containing the plasma. It is an all-welded, rigid structure made of INCONEL 625, with a major radius of 1995 mm and minor radius of 475 mm. It is bakeable up to 170°C, in order to eliminate the impurities of the first wall.

first wall : it's the inner side of the vacuum vessel, exposed to the plasma discharge. It is composed by 2016 graphite tiles that cover completely the inner part of the vacuum vessel (see fig. 1.13). In RFX-mod the shape of the tiles has been redesigned to minimize the emissivity due to plasma wall-interaction. Graphite has been chosen for its low

Figure 1.12: Picture of RFX-mod experiment.

atomic number Z. In fact, the presence of other elements different from the main gas, the impurities, contribute to increase Z_{eff} and thus to enhance the radiation emission with a reduction of the energy confinement. This effect is strongly dependent on the atomic number of the impurities in the plasma.

stabilizing shell : it has the main purpose of stabilizing MHD ideal instabilities. It is made of copper and it is 3mm thick, located at $1.11a$. It

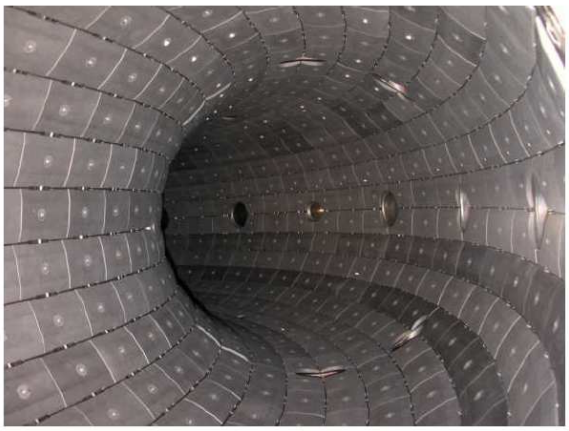

Figure 1.13: Picture of RFX-mod experiment with many diagnostic installed.

passively controls also the horizontal equilibrium of the plasma.

mechanical structure : the new shell is too thin to bears the weight of the vacuum vessel and of the toroidal windings, hence a new mechanical structure has been installed.

magnetizing coils : they provide the time varying poloidal magnetic flux that induces the plasma current during the discharge. It is composed by 40 coils that can carry a maximum current of 50kA and produce a 15Wb maximum flux.

toroidal coils : a set of 48 coils uniformly distributed along the toroidal direction, that surround the vessel and the shell. They are designed to generate the toroidal magnetic field needed to set-up and maintain the discharge (up to 0.7T). The coils are series-connected in 12 groups of 4: each group is connected to an independently controlled power supply unit.

field shaping coils : this set of poloidal coils is designed to generate a uniform vertical field aimed at controlling the position of the plasma column with respect to the vessel during the discharge.

active coils system : this new set of saddle coils is necessary in RFX-mod in order to control the instability arising on the shell time-scale. It is a set of 192 coils, distributed in 48 different toroidal positions and 4 poloidal positions; each coil extents 90° poloidally and 7.5° toroidally, for a full surface coverage. The power supply units are digitally controlled by a set of dedicated CPUs that can process 192 sensor inputs and generate 192 reference outputs at a rate of about 2.5kHz. The digital system allows for a great flexibility in the implementation of control system. A scheme of the saddle coils on a section of RFX-mod is displayed in figure 1.14.

In RFX-mod a full set of diagnostics is installed in order to measure many physical quantities, in their temporal a spatial variations. A brief description of the most important ones follows:

- a complete set of magnetic diagnostics: integral probes, situated between the vacuum vessel and the shell, which measure plasma current (by means of 4 Rogowski coils) and concatenated flux variations (using 8 toroidal and 6 poloidal voltage loops) providing information on loop voltage and toroidal flux, 196 bi-axial pick-up coils, distributed

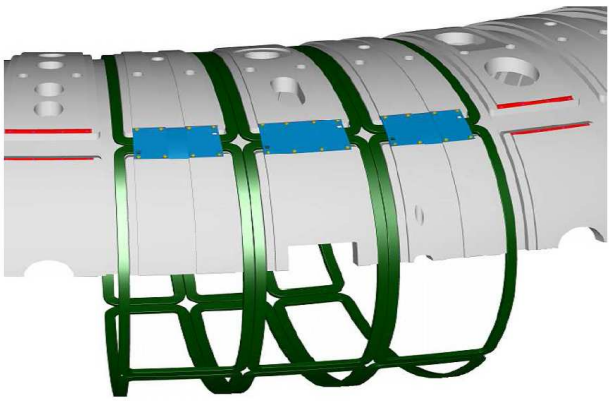

Figure 1.14: Set of 12 saddle coils (3 toroidal and 4 poloidal positions) surrounding the RFX-mod shell.

along 48 toroidal directions and 4 poloidal directions, which measure toroidal and poloidal components of magnetic fields; 48×4 saddle probes, measuring the radial component of the field, coupled to the active control coils;

- a Thomson scattering diagnostic [20], which provides a 84-point radial profile of electronic temperature by analyzing the scattering properties of the plasma when a high power laser beam is injected; the repetition rate is of about 25 ms, for a maximum number of 10 pulses in a discharge;

- a multichord interferometer [21, 22], which measures the electronic density averaged along 14 lines of sight. The density is evaluated measuring the phase variation induced in a CO_2 laser beam ($\lambda = 10.6\mu m$) that passes through the plasma. In this thesis we will use intensively data from interferometer, a detailed description of the interferometric technique shall be given in chapter 3;

- spectroscopic diagnostics [23], which measure line intensities of radiation emitted by main gas and by impurities, in order to calculate their influxes at the edge, the toroidal flow of the plasma and the effective charge;

- an Integrated System of Internal Sensors (ISIS) [24], which includes poloidal and toroidal arrays of magnetic pick-up coils and electrostatic

(Langmuir) probes (used to measure and correlate fluctuations of electric and magnetic fields), and 8 calorimetric sensors. The complete set of probes are presented in table 1.1: The magnetic probes are located

ISIS probes ($f_s = 2$ MHz)	**number**
toroidal field toroidal arrays	2 x 24
poloidal field poloidal arrays	1 x 8
toroidal field poloidal arrays	1 x 8 + 1 x 6
radial field poloidal array	1 x 8
toroidal array of single e.s. probes	1 x 72
poloidal array of triple e.s. probes	1 x 7
toroidal array of calorimetric sensors	1 x 8

Table 1.1: Set of probes of the Integrated System of Internal Sensor.

behind the graphite tiles, which cover the first wall of the machine, and consist of pick-up coils measuring the time derivative of the magnetic field $\boldsymbol{B_T}$. The sampling frequency is 2 MHz, while the estimated bandwidth of the measurement is up to 400 kHz.

- a Soft-X Rays multifilter diagnostic [25], used for measuring electronic temperature at the center of the plasma by means of comparing SXR emissions measured by differently filtered silicon detectors; it allows a higher time resolution with respect to the Thomson scattering, but with a lower spatial resolution; 4 chords with different filter thicknesses are used, in order to measure temperature in a wider range of emission levels.

- a Soft X-Rays tomographic system [26] for the reconstruction of the poloidal emissivity map. The diagnostic is composed by 3 vertical fans each with 19 lines of sight and 1 horizontal fan with 21 lines of sight. The total 78 lines of measurements almost entirely cover the plasma cross section.

The data from all these diagnostics are collected during the discharge and are then analyzed and used as input to several numerical codes. In particular we are interested in the data from the interferometer.

1.4.2. TPE-RX: Toroidal Pinch Experiment-RX.

The plasma in TPE-RX has minor radius $a = 0.45$ m and major radius $R_0 = 1.72$ m. The design values of the maximum I_p and pulse duration time are 1MA and 100 ms, respectively. The maximum achieved I_p is 500 kA,

Figure 1.15: Picture of TPE-RX device.

limited by the energy of the power supply. The vacuum vessel consists of 16 bellows sections and 16 connected port sections, and it is made of stainless steel 316L. It acts also as first wall and it is protected by 244 mushroom-shaped Molybdenum limiters installed inside of the vacuum vessel, covering almost the 30% of the first wall. The shell is a double-layered system made of an inner thin copper shell (0.5 mm thick) and an outer thick (50 mm) Aluminium shell. The inner shell is mainly devoted to suppression of MHD instabilities. The outer thick shell is mainly dedicated to passive equilibrium control, and, for this reason, its centre is shifted by 17.5mm inwards from the centre of the vacuum vessel and the thin shell. The toroidal winding is made by 32 coils, producing a magnetic field made of two sector of 16 coils connected in series. Each sector can be connected to the other both in series or in parallel, allowing the changing of the reversal time of the toroidal field at the edge. Figure 1.15 shows a picture of the TPE-RX device: the torus, surrounded by the toroidal field coils and the field shaping coils is visible. The blue structure is the Iron core of the magnetizing system, composed by a set of poloidal field coils that provides also the equilibrium vertical field. The maximum flux provided by the poloidal coils is much lower than the RFX one ($\Phi_{max} \simeq 4Wb$), sufficient to reach 1 MA of plasma current, thanks to the iron core.

The main diagnostic installed at TPE-RX are:

- interferometer: the electron density is measured by means of a two chords Mid InfraRed interferometer [27]. The measure beam is provided by a CO_2 laser ($\lambda = 10.6\mu m$), whereas an HeNe one ($\lambda = 3.39\mu m$)compensates the vibration. The normalized impact parameter are $h/a = 0$ for the central chord and $h/a = 0.69$ for the edge

one.

- D_α detection system: a toroidal array of 13 D_α monitors installed in the inner side of the torus (high field side) detects the brightness of radiation emitted by Deuterium neutral atoms along a radial line of sight.

- Soft X Rays [28]: SXR is measured by a diagnostic composed of two arrays of surface barrier diodes. The vertical array has 13 parallel lines of sight with impact parameters laying between $r/a = -0.8$ and $r/a = 0.8$ and the horizontal array has 11 lines of sight laying between $r/a = -0.614$ and $r/a = 0.614$. With this diagnostic we can measure the line integrated soft X- ray emissivity (the brightness) and we can calculate the bidimensional map of the SXR emissivity by tomographic inversion.

- Thomson scattering [29]: It is a single point, single pulse measurement system using a ruby laser with energy of about 4 J.

CHAPTER 2

Transport phenomena in fusion plasma.

Theories of particle and energy transport in magnetic confined plasma are presented in this chapter, that study classical and neoclassical (including toroidal effects) transport properties. The confinement in such devices is worse than that predicted by classical and neoclassical theory, hence some additional mechanism must be invoked. Many theories of anomalous transport were developed in the past: here the Rechester and Rosembluth model, integrated with the Harvey contribution, is explained and some experimental method to check it are presented. Since the anomalous transport is related to magnetic fluctuations, some techniques to reduce them are discussed. Moreover, with the aim to perform transient transport studies, the modification of the particle source in the plasma by means of pellet injection is described.

2.1 Classic, neoclassic and anomalous transport

To pursue the production of energy by means of thermonuclear fusion it is crucial to confine a hot, dense plasma for enough long time, as stated in paragraph 1.2.2. The transport of matter and energy perpendicular to the unperturbed magnetic surfaces is responsible, with the electromagnetic radiation, of the deterioration of the conditions favorable for the nuclear fusion. The understanding of the fundamental mechanism behind these losses will lead to an improved action to counter them and reach a better confinement in the plasma.

The *classical transport* includes, generally speaking, three ways in which plasma particles can cross magnetic surfaces:

a) collisions that cause the diffusion

b) drift motion arising from curvature or gradients of the field

c) electric field inside the plasma

Including also the more complicated orbits to be found in toroidal configuration, it is dubbed *neoclassical transport*.

The diffusion flux along $\hat{x}$ direction, due to collision is $\Gamma_x = nv_x = (\frac{-D}{\partial n/\partial x})$ [3]. The diffusion coefficient $D \approx \rho_l^2 \nu$, where ρ_l is the gyroradius of a charged particle along a magnetic field line. For a uniform, straight field B:

$$\rho_l = \frac{v_{th} m}{ZeB} \qquad [\mathrm{m}] \tag{2.1}$$

with v_{th} thermal velocity of the charged particle of mass m and charge Ze. The electron-ion collision frequency ν_{ei} [30] is:

$$\nu_{ei} = 2.92 \times 10^{-12} Z_{\mathrm{eff}} n T^{-3/2} \ln \Lambda \qquad [\mathrm{s}^{-1}] \tag{2.2}$$

where $\ln \Lambda = \ln(T_e^{3/2}/\sqrt{\pi} Z e^3 n_e^{0.5}) \approx 15$ is the Coulomb logarithm [3].

In a toroidal devices for magnetic plasma confinement the magnetic field is non-uniform. The orbit of a charged particle is not only a simple helical motion around a field line but also a drift arising from curvature and gradients of the magnetic field. The combined drift motion of the guiding centre of the particle is [3]:

$$v_d \propto \frac{1}{q} \frac{\boldsymbol{B} \times \nabla \boldsymbol{B}}{B^3} \tag{2.3}$$

This drift, proportional to q, generates a charge separation into the plasma, hence an electrical field $\boldsymbol{E}$. A global radial motion of the plasma (independent on charge sign) owing to $\boldsymbol{E} \times \boldsymbol{B}$ drift is present and a poloidal field is needed to obtain a null mean displacement of the plasma.

When the guiding centre of a particle is moving almost parallel to the field, it experiences the magnetic field gradient going from the low field side to the high field side. In the case that its parallel velocity is high enough, the particle is passing and its orbit, projected on the poloidal plane, is a displaced circle. If the parallel velocity is below a threshold, hence it is performing a spiral motion with a small pitch around the line, the particle is reflected by the "mirror effect". This latter class of particle, called trapped, has a characteristic banana-shaped orbit, as shown in blue in figure 2.1

The radial excursion of a banana orbit may exceed the Larmor radius: $\Delta r \approx \frac{r}{R}^{\frac{1}{2}} \rho_p$ where ρ_p is the gyroradius in the poloidal field B_p, according to equation 2.1.

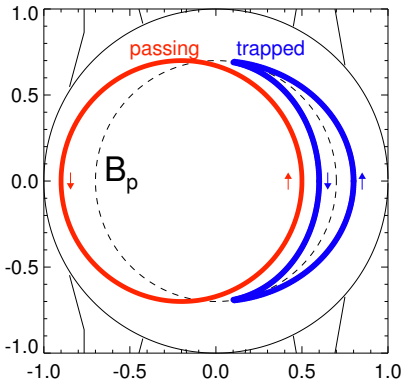

Figure 2.1: Sketch of passing (red) and trapped (blue) orbit projected on the poloidal plane. The dashed line represent the poloidal magnetic field. Displacement are oversized to clarify the concept.

The diffusion related to banana orbit $D_B \propto \left(\sqrt{(2r/R)}\rho_p^2\nu\right)$ is higher than the classical one. However, for this term to be important, the collision frequency must be low enough to permit the charged particles to complete banana orbits.

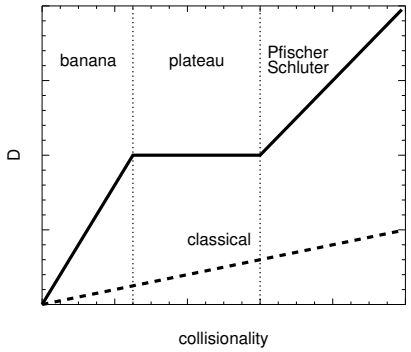

Figure 2.2: Schematic view of the dependence of the neoclassical and classical diffusion coefficient D on collision frequency, with the three different neoclassical regimes.

It is usual to define three diffusion regions as function of the collisionality of the plasma: the collisional regime, dubbed as Pfirsch-Schulter where banana effects are unimportant, the collisionless (or banana) regime and the intermediate one the so called plateau regime. A scheme of the form of the diffusion coefficient is given in figure 2.2.

Unfortunately the observed transport in toroidal device for thermonuclear fusion is *anomalously* high compared to neoclassical transport predictions. Anomalous transport in toroidal plasmas results from instabilities that are driven by source of free energy in the plasma e.g. pressure, density, temperature, resistivity, etc. gradients which are involved in plasma configurations. Various theoretical approaches have been developed and proposed in the past. Each of them has its own peculiarity and it is related to one or more sources of free energy in the plasma.

There has been only limited success in identifying particular mechanisms candidates to explain transport in certain region of toroidal devices. Anyway the Rechester and Rosembluth [31] approach, with the contribution of Harvey [32], explains quite well the transport in RFP plasma [33].

This thesis is based on data of RFP experiments, hence a deep understanding of the transport mechanism is needed: the theory of transport of charged particles in stochastic magnetic field is presented in the following section.

2.2 Transport theory in a stochastic magnetic field

The actual confinement properties of toroidal devices devoted to study the magnetic confinement of fusion plasma, is known to be much worse than that predicted by classical and neoclassical theory. Since parallel transport of charge particles along magnetic lines is very efficient, a system where lines can wander from the centre to the edge it is affected by an enhanced radial transport, with strong leakage of energy and particles. The Rechester and Rosembluth theory [31] indeed models electron parallel transport in a plasma with destroyed magnetic surfaces, that is to say with stochastic magnetic field.

The equilibrium field in cylindrical geometry is $\boldsymbol{B} = B_z\boldsymbol{z} + B_\theta\boldsymbol{\theta}$. In order to model toroidal periodicity, the system is periodic along $\boldsymbol{z}$, with period $2\pi R$. The perturbation $\delta\boldsymbol{B}$ to $\boldsymbol{B}$ can be written in the form:

$$\delta\boldsymbol{B} = \sum_{m,n} \boldsymbol{b}_{m,n}(r) \exp\left[i\frac{m\theta - nz}{R}\right] \tag{2.4}$$

where m is the wave number in poloidal direction and n is the one in toroidal direction. The magnetic surface associated to each harmonic of the equation 2.4 has the shape of a so-called magnetic island. Its position along the minor radius is localized near the rational cylindrical surfaces $r_{m,n}$ defined by the condition that the safety factor $q(r_{m,n}) = \frac{r_{m,n}B_z}{RB_\theta} = \frac{m}{n}$.

When many harmonics are present, conserved magnetic surfaces exist if the point of intersection of a single field line with the plane at fixed z lies on a smooth closed curve. If the intersection points do not identify a curve but are rather randomly distributed to fill the whole area, then we can consider

that the magnetic surfaces are destroyed and the magnetic field is stochastic. This condition corresponds to magnetic islands that overlaps to each other. The effect of the overlapping of the magnetic island could be seen in figure 2.3: on the left a magnetic surface mapped by an unperturbed magnetic line on the poloidal plane is shown, whereas on the right one can see the trace of the same field line when $m = 1; n = (-7 \div -23)$ perturbations are added: the conserved magnetic surface is entirely destroyed by radial displacement of the field lines. If one considers a small circle of radius r_e

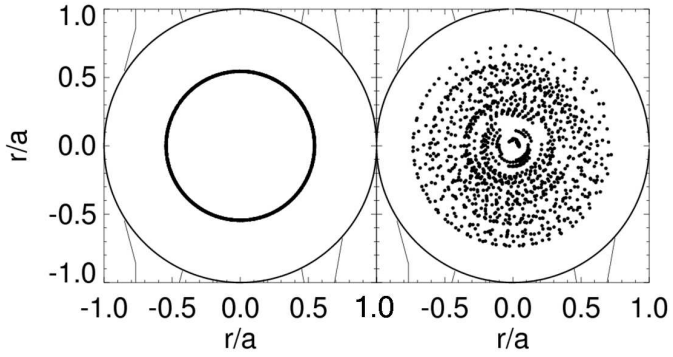

Figure 2.3: Poloidal cross section of unperturbed magnetic surface, on the left and effect of the presence of $m = 1$ perturbation, on the right.

(magnitude of the electron gyroradius) and maps it by solving the equation $\left(\frac{dr}{dz} = \frac{B_r}{B_z}; r\frac{d\theta}{dz} = \frac{B_\theta}{B_z}\right)$, because of the relation $\boldsymbol{\nabla} \cdot \boldsymbol{B} = 0$, the mapping is area preserving. One can imagine two different evolutions of the area: the first moves it as a whole and the second deforms its shape, contracting it in one direction and stretching it in the other. Hence, following the circle area along the z direction, it goes from shape shown in figure 2.4 (a), to (b) and finally to something similar to (c).

The width δ of the area will exponentially decrease in order to conserve the total area: $\delta(z) = r_e \exp(-z/L_c)$ where L_c is the correlation length. If a fixed m and various n island is present in the plasma, the analytic form for the correlation length exists: $L_c = \pi R/\ln(\pi s/2)$, where s is the stochasticity parameter. In general there is no explicit formula but the correlation length would be smaller. The distance $l_0(z) = r/m$ for a fixed m represents the distance over which different parts of the area move almost independently, hence we can define the correlation length for the area $L_{c0} = L_c \ln(r/mr_e)$. It can be shown [31] that the average radial displacement of the area can be described by a diffusion formula:

$$\langle (\Delta r)^2 \rangle = 2LD_M \tag{2.5}$$

where L is the distance in $\boldsymbol{z}$ direction, with $L \gg L_{c0}$. The stochastic dif-

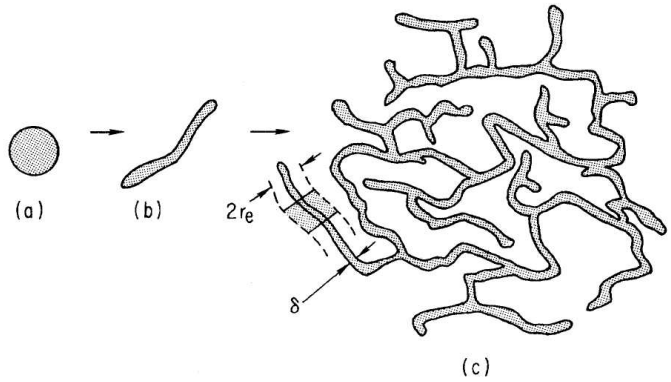

Figure 2.4: Sketch of the evolution of area mapping in a braided magnetic field [31].

fusion coefficient for magnetic lines D_M can be derived in a quasilinear approximation, resulting:

$$D_M(r) = \pi R \sum_{m,n} \frac{|b_{mn-r}(r)|^2}{B_z^2} \delta\left(\frac{m}{q(r)} - n\right) \tag{2.6}$$

It is important to underline that the mapping described above is strictly reversible but because of the very small width reached by the area, any small spreading perpendicular to the magnetic field line (e.g. the Larmor motion) leads outside of the mapped area, jumping into another one.

If we mark many electrons inside the area of initial width r_e and then follow their radial distribution in the time t, we will state that the radial thermal conductivity is, as for a Brownian process, $\chi_r = \langle(\Delta r)^2\rangle/2t$. The χ_r can be determine in a collisionless limit: the collision mean free path λ is bounded by $L_c \ll \lambda \ll r^2 v/\chi_r$.

To study the behavior in the collisionless limit, we assume that the guiding centre of the particles coincide with the field line and consider, instead of many discrete particles, just one particle which is spread with equal probability over the initial area of dimension r_e. The rapid parallel motion produces a continuous mapping of the area. The collision process occurs periodically after the time interval τ and, as result of the collision, the parallel velocity can remain the same or change its direction. At the same time, thanks to the scattering process, the whole area is spread radially at a distance r_e (in the toroidal case, the jump would be equal to the width of an electron "banana" orbit): this is the modeling of the perpendicular jump of the particle owing to a collision.

The initial small circle of radius r_e moves a distances $\lambda = v\tau$ mapping into a region with shape shown in figure 2.4 (c) or similar. The width of each branch is $\delta(z) = r_e \exp(-\lambda/L_c) \ll r_e$ and the squared average radial

displacement before colliding is $\langle(\Delta r)^2\rangle = 2\lambda D_M$. The effect of a collision is to increase the width of the area from δ to r_e. Cutting the new "thick" area in pieces of size r_e we obtain number of pieces that will evolve as the original circle area, almost independently from their previous history: this is due to the characteristic of the collisionless scenario, where $\delta(\lambda) \ll r_e$. The diffusion of the initial area follow the random walk scheme and the radial or perpendicular diffusion coefficient is

$$\chi_r = \frac{\langle(\Delta r)^2\rangle}{2\tau} = \frac{\langle(\Delta r)^2\rangle}{2\lambda} v = D_M v \tag{2.7}$$

The relation 2.7 shows that, in the collisionless frame, the particle diffusion coefficients can be written as the diffusion coefficient of the magnetic lines multiplied by the ion thermal velocity: $v = \sqrt{\frac{2T_i}{m_i}}$.

2.2.1. Transport properties related to ambipolar electric field arising from stochastization of the magnetic field.

As already stated, it has been theoretically demonstrated that very small non-axisymmetric perturbation to the flux surfaces can lead to magnetic lines which, after some turn, wander out of the plasma. In such case the fast parallel transport is coupled to radial displacement of particles. The faster transport of electrons relative to ions gives rise to a radial ambipolar electric field [31, 34], adjusting the electron flow rate to equal the ion rate. Hence particle transport is constrained by the ambipolarity requirement: the positive potential established in the centre relative to the edge reduces electron particle transport and slightly increases the ion radial loss.

In [32] the ambipolarity constrained particles flux are derived from the kinetic equation, including the ambipolar radial electric field E_a. The distribution function $f(\epsilon, r)$ depends on position r and energy $\epsilon = \frac{1}{2}mv_\parallel^2/2 + \mu B + qE_a$ of the guiding-centre of the particles, where $\mu = \frac{1}{2}mv_\perp^2/B$ is the magnetic moment. The guiding-centre kinetic equation is simply:

$$\frac{\partial f}{\partial t} + \boldsymbol{v} \cdot \nabla f = 0 \tag{2.8}$$

with $\boldsymbol{v}$ guiding-centre velocity. The rate of change of f, derived by Harvey, under assumption that are detailed in [32], is:

$$\left(\frac{\partial f}{\partial t}\right) = \frac{|v_\parallel|}{r}\mathcal{L}(r) D_M \mathcal{L}(f) \tag{2.9}$$

where the operator $\mathcal{L} \equiv \frac{\partial}{\partial r} + \frac{qE_a}{mv_\parallel}\frac{\partial}{\partial v_\parallel}$, with r radial coordinate, q and m respectively charge and mass of the particles. D_M is the diffusion coefficient related to the stochastic magnetic field due to magnetic perturbations, as stated in previous section.

Computing the zeroth order moment of the 2.9, assuming a Maxwellian distribution function, one can determine the particle flux Γ by comparison with the particle source free continuity equation $\frac{\partial n}{\partial t} = -\frac{1}{r}\frac{\partial}{\partial r}(r\Gamma)$, obtaining two equation, one for electrons and one for ions:

$$\Gamma_e = -D_M \frac{v_{th}^e}{\sqrt{\pi}} n_e \left(\frac{n_e'}{n_e} + \frac{T_e'}{2T_e} - \frac{eE_a}{T} \right) \tag{2.10}$$

$$\Gamma_i = -D_M \frac{v_{th}^i}{\sqrt{\pi}} n_i \left(\frac{n_i'}{n_i} + \frac{T_i'}{2T_i} + \frac{eE_a}{T} \right) \tag{2.11}$$

where $v_{th} = \sqrt{2T/m}$ is the thermal velocity and the prime notation represents differentiation. The ambipolar field E_a can be obtained from the 2.10 by setting $\Gamma_e = 0$:

$$eE_a \simeq -T_e(\frac{n_e'}{n_e} + \frac{T_e'}{2T_e}) \tag{2.12}$$

Replacing the ambipolar field in the 2.11 the ion flux is obtained. Assuming the quasineutrality $n_e \simeq n_i$ and $T_e \simeq T_i$, gives:

$$\Gamma_i = -2D_M \frac{v_{th}^i}{\sqrt{\pi}} n_i \left(\frac{n_i'}{n_i} + \frac{T_i'}{2T_i} \right) \tag{2.13}$$

The first term of equation 2.13 is related to *diffusion*, being proportional to the density gradient, whereas the second term take account the *convective* mechanism arising from the temperature gradient.

In conclusion, in the framework of the theory of particle transport in a stochastic magnetic field, we are allowed to write the particle flux as a diffusive term and a convective term entailing the ambipolar field and the $(\boldsymbol{E} \times \boldsymbol{B})$ drift contribution:

$$\begin{aligned} \Gamma_i = \Gamma_{\text{diff}} + \Gamma_{\text{conv}} &= \Gamma_{\text{diff}} + (V_{st} + V_{E\times B}) n_i = \\ &\quad -2D_M \frac{v_{th}^i}{\sqrt{\pi}} n_i \left(\frac{n_i'}{n_i} + \frac{T_i'}{2T_i} \right) + V_{E\times B} n_i \end{aligned} \tag{2.14}$$

where D_M is the magnetic diffusion coefficient and, in the framework of the behaviour of charged particles in stochastic magnetic field, can be computed by the equation 2.6. We can write the particle diffusion coefficient as (cfr. eq 2.7):

$$D_{st} = D_M v_{th}^i \simeq \frac{\delta \boldsymbol{B}^2}{\boldsymbol{B}} L_{\text{eff}} v_{th}^i \tag{2.15}$$

where the L_{eff} is the effective connection length, which for the RFP can be assumed to be of the order of the minor radius of the torus [35].

2.3 Transport experiment

Notwithstanding the number of different mechanisms responsible of the particle transport in a thermonuclear plasma, it is always possible to describe the particle transport with a continuity equation: $\frac{dn}{dt} = S_{\text{tot}}$. It means that any variation of the density $n = n_e = n_i$ (quasineutrality) of the plasma must be equal to the total source term S_{tot}:

$$\frac{dn}{dt} = \frac{\partial n}{\partial t} + \boldsymbol{v}\cdot\boldsymbol{\nabla} n = \frac{\partial n}{\partial t} + (\boldsymbol{\nabla}\cdot(n\boldsymbol{v}) - n(\boldsymbol{\nabla}\cdot\boldsymbol{v})) = \frac{\partial n}{\partial t} + \boldsymbol{\nabla}\cdot\boldsymbol{\Gamma} = S_{\text{tot}} \quad (2.16)$$

where the term $(\boldsymbol{\nabla}\cdot\boldsymbol{v}) = 0$ because of the incompressibility hypothesis. The continuity equation, written explicitly in cylindrical coordinates and assuming that the plasma is homogeneous in poloidal and toroidal direction, is

$$\frac{\partial n(r,t)}{\partial t} = -\frac{1}{r}\frac{\partial r\Gamma(r,t)}{\partial r} + S(T_e(r,t))n_n(r,t)n(r,t) - \alpha(T_e(r,t))n^2(r,t) \quad (2.17)$$

where $S(T_e)$ is the ionization rate, that gives the particle source term due to ionization of the neutral (n_n is the neutral density) due to electron impact. The term $\alpha(T_e)$ is the total recombination rate, that considers both radiative recombination and three-body processes. The particle flux $\Gamma = n\boldsymbol{v}$ can be written, according to equation 2.14, as the sum of a diffusive term and a convective term:

$$\Gamma(r) = -D(r)\frac{\partial n(r,t)}{\partial r} + V(r)n(r,t) \quad (2.18)$$

The confinement properties of the plasma can be studied imposing the D and V values according to a transport model: the density behaviour predicted by the theory can thus be compared with the experimental evolution. Moreover, in order to perform a more significant check of the model, we can actively modify some terms of the equation 2.17. In the framework of the Rechester, Rosembluth and Harvey theory, presented in section 2.2, the diffusion coefficient is related to the normalized squared magnetic fluctuation $\left(\frac{\delta \boldsymbol{b}}{\boldsymbol{B}}\right)^2$ hence, reducing or enhancing the magnetic stochasticity should lead to different confinement properties. The other term on which we can operate is the particle source term: the neutral density n_n can be modified by means of gas puffing or pellet injection. The action on magnetic perturbation and on particle source will briefly discussed in next paragraphs 2.3.1 and 2.3.2.

2.3.1. Reduction of magnetic fluctuation: PPCD and the system of active coils.

An example of external control of global magnetic perturbation, such as MHD modes, is the Pulse Poloidal Current Drive (PPCD). This technique,

applied for the first time in the MST experiment [36, 37], is based on the application of a poloidal electric field, driven inductively at the plasma edge by varying the current in the toroidal field coils. The direction of the current pulses in the toroidal coils is such that a negative variation of the toroidal magnetic field flux is induced in the plasma. This has the main effect of increasing the toroidal magnetic field reversal and inductively modifying the current density profile, in such a way to reduce the free-energy source for the tearing modes. This transient modification of the magnetic field and current density profiles reduces the magnetic fluctuations and thus the anomalous transport which has a strong effect on the confinement properties of the plasma. The PPCD is a technique extremely interesting conceptually, but a practical limit is its intrinsically transient nature. In fact, in order to drive a poloidal electric field in the plasma one has to ramp the external toroidal field toward more and more negative values. After a few milliseconds the toroidal field reversal is so deep that spontaneous large relaxation events occur and the PPCD has to be stopped anyway. Further details on this technique can be found in [38, 39].

To overcome the transient nature of the PPCD and to have a fine spatial and temporal *active control* of the MHD modes, a new approach is required. RFX machine have been recently modified to pursuit the reduction of the radial field at the boundary in order to study the induced plasma mode rotation, the prevention of mode phase locking and the stabilization of resistive wall modes. This allows to study all their consequences on the global transport properties of RFX-mod plasma. The radial field perturbation are controlled by a set of 192 (4 poloidally and 48 toroidally) feedback controlled saddle coils with independent power supplies [18]. Each coil is coupled with a radial field sensor mounted in the same position in order to measure the local perturbation to the axisymmetric magnetic field. The 192 coils system allows mimicking an ideally conducting wall by locally opposing the radial field (Virtual Shell, VS) or actively controlling individual MHD modes (mode control, MC). They can generate magnetic field harmonics with $m = 0; n = 0 \div 24$ and $m = 1; n = -23 \div 24$.

The Virtual Shell operation is characterized by a feedback law that is set up in order to minimize the radial component of the field at the sensors for every helicity (excluding the equilibrium field m = 1, n = 0) [40]. The Virtual Shell configuration is obtained performing a two dimension FFT on B_r and B_p measurements in order to compute the amplitude and phase of the MHD mode affecting the plasma. These quantities are compared with a given reference value for each mode and, with an inverse FFT, the current on each active coils is computed to perform the local correction of the radial field. This method allows us to control the whole spectrum of MHD perturbations present in the plasma or to choose to damp only a subset of modes. In the latter case the method is named Selective Virtual Shell (SVS).

In the following of the thesis only RFX-mod plasma pulses in VS configuration are analyzed, more details on Mode Control can be found in [41].

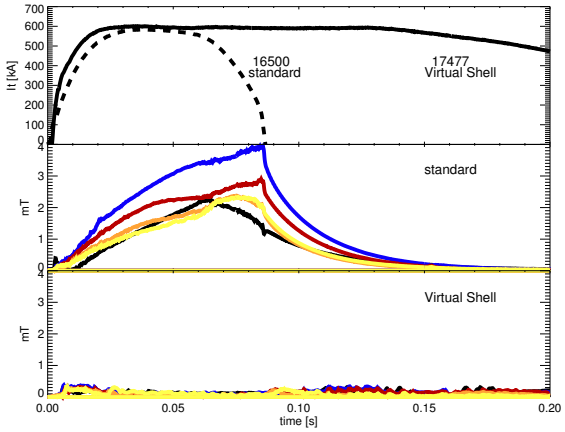

Figure 2.5: Comparison of m=1 modes amplitude for a discharge without Virtual Shell (16500) and a discharge with active coils system in action (17477). First panel shows the plasma current for VS (—) and standard (- -) pulse.

In figure 2.5 the effect of operating in VS mode is shown: two discharges at $I_t = 600$ kA are compared. The standard discharge (meaning with no active control of radial field) is shorter than the Virtual Shell pulse. The main B_r modes behaviour, shown in second and third panel, clearly displays the damping owing to the active coils: their amplitude in VS case is ten times lower.

2.3.2. Modification of the particle source: pellet injection.

In the stationary phase of the plasma pulses the particles losses are entirely balanced by the incoming flux from the first wall Γ_{in} and the total particle content is kept constant. In order to actively act on the plasma density, many refueling methods have been developed in the years, with the aim of providing particles to the plasma and controlling their radial deposition. The most important are gas puffing and pellet injection. It was recognized early in the magnetic fusion development program that fueling of hot plasmas by the traditional method of puffing hydrogenic (H_2, D_2, T_2) gas into the vacuum vessel would be problematic because the gas molecules do not penetrate deeply into the plasma core where the hot and dense plasma is and where, in a fusion reactor, they are most needed to replenish hydrogenic ions consumed by the deuterium-tritium (D-T) fusion reactions. In this thesis pellet injection experiments will be discussed, hence only this technique will be presented in the following. A complete review of pellet injection

techniques can be found in [42].

Injection of frozen macroscopic pellets has become the leading technology for refueling magnetically confined plasmas for controlled thermonuclear fusion research. The process of plasma fueling by this approach has been tested on a number of toroidal magnetic confinement devices, including tokamaks, stellarators and reversed field pinches. The principle is quite simple: a small (order of 10^{21} atoms) hydrogenic iced pellet is created and accelerated by means of a pneumatic system using light gas or a centrifuge system in a velocity range $100 \div 3000$ meter per second and injected in the plasma. Once the pellet has entered the plasma, the ablation of the material from its surface starts, becoming more and more efficient as the pellet goes toward the hot and dense plasma in the centre of the torus.

A complete description of the penetration of a cryogenic pellet in a hot, magnetized plasma takes into account mechanisms related to neutral gas dynamics around the pellet, atomic physics processes, charging of the ablated cloud and diamagnetism of the cold plasma cloud (plasmoid) surrounding the pellet.

The models developed to study the penetration of a pellet in the plasma can be grouped in two families:

Neutral Gas Shielding NGS model [43] makes several simplifying assumptions to describe the penetration of a pellet in a plasma. The ablation, due to electron impact, is reduced considering only the shielding of the neutral cloud expanding spherically from the pellet surface. Moreover, the Maxwellian distribution of the incident electrons is approximated by a mono-energetic beam. Other mechanisms are not modeled except for allowing an additional global reduction of the electron heat flux, hence of the ablation rate In spite of this simplified scheme, the penetration depths predicted by the NGS model are generally in good agreement with the experimental measurements for a wide range of plasma (density and temperature) and pellet (mass and velocity) parameters. The pellet surface regression velocity predicted by NGS model is:

$$\frac{dr_p}{dt} = 10^{-16/3} \times 1.72 \times 10^{-8} \times n^{1/3} \times T^{5/3} \times r_p^{-2/3} \tag{2.19}$$

where r_p is the equivalent spherical pellet radius.

Neutral Gas and Plasma Shielding Under the name of NGPS scaling law, a numbers of more sophisticated models are included. In general the NGPS describes the ablation considering not only the presence of a spherical neutral cloud around the pellet, but also a cold plasma (plasmoid). The plasmoid, experiencing the presence of the magnetic field, is elongated and aligned with the local magnetic lines, providing

an additional shielding effect. Moreover the local Maxwellian distribution of the energy of bulk electrons is considered, hence relative to NGS, NGPS provides a more physical description of the heat flux on the pellet. The NGPS model presented in [44] gives the following law for the ablation rate:

$$\frac{dr_p}{dt} = 5.286 \times 10^{-18} \times B^{-0.02} \times V_p^{0.05} \times n^{0.57} \times T^{1.61} \times r_p^{-0.48} \quad (2.20)$$

where B is the magnetic field and V_p is the pellet velocity.

In Tokamak experiments NGS and NGPS models, despite the more accurate description given by the NGPS, provide comparable results on pellets penetration depth and ablation rate [45].

CHAPTER 3

Transport study: diagnostic and numerical tools.

The interferometric technique to measure the electron density of a plasma is presented in this chapter. Furthermore the interferometers installed at RFX-mod and at TPE-RX are described.
Then the numeric tools used in this thesis are introduced: the inversion code to compute the electron density profile from the integral line interferometric data, the transport code TED (TEmperature and Density), the Monte-Carlo program for the diffusion of neutral particles in the plasma NENÈ (NEutral and NEutral) and the Field Line Tracing FLiT.

3.1 Interferometric measurement of plasma density

A reliable measurement of the plasma density is a key factor in the study of the nuclear fusion: as stated in paragraph 1.2.2, the feasibility of obtaining energy from fusion is subject to the capability of reaching and maintaining the triple product $n\tau_E T_i$ at values above $3 \cdot 10^{21} \mathrm{m}^{-3}$ s keV (eq. (1.5)). The most used technique to measure plasma density in present fusion experiments is the interferometric one: an active diagnostic method that uses an electromagnetic wave as a probe. The technique is not perturbing since the energy of the radiation is negligible with respect to the plasma energy.

Since the electromagnetic wave has a sufficient high frequency, we can consider the ions to be stationary because their inertia is too large for them to respond to a high frequency wave and we neglect the electron pressure: these approximations are named *cold plasma* condition. It is equivalent to assuming $T_e = T_i = 0$. With this approximation the refractive index μ is

described by the theory of propagation of electromagnetic waves in a cold plasma, neglecting the particles thermal velocity, that is much lower than the phase velocity of the wave [46]. For a wave propagating perpendicularly to the magnetic field $\boldsymbol{B}$, the expression for μ depends on the polarization of the wave. For the so-called *ordinary wave*, polarized whit the electric field $\boldsymbol{E_w}$ parallel to the plasma magnetic field $\boldsymbol{B}$, the refractive index is:

$$\mu_{\text{ord}} = \left(1 - \frac{\omega_p^2}{\omega^2}\right)^{1/2} \tag{3.1}$$

whereas, if the wave has the $\boldsymbol{E_w}$ perpendicular to $\boldsymbol{B}$ (*extraordinary mode*), the expression of μ_{ex} is:

$$\mu_{\text{ex}} = \left(1 - \frac{\omega_p^2}{\omega^2}\frac{\omega^2 - \omega_p^2}{\omega^2 - \omega_p^2 - \omega_{ce}^2}\right)^{1/2} \tag{3.2}$$

where $\omega_p = \left(\frac{n_e e^2}{\epsilon_0 m_e}\right)^2$ is the *plasma frequency* and $\omega_{ce} = \frac{eB}{m_e}$ is the *cyclotronic frequency*. The expression (3.1) set the first boundary to the frequency of the electromagnetic radiation used: $\omega > \omega_p$ so that the wave can propagate in the plasma, the so called *transparency condition*.

The RFP is characterized by a high magnetic shear: the magnetic field greatly changes its direction moving along a straight direction through the plasma cross section, hence the relation $\boldsymbol{E_w} \parallel \boldsymbol{B}$ is only locally satisfied. Anyway for typical plasma parameters $\omega_p \gg \omega_{ce}$, which allow us to approximate equation (3.2) with equation (3.1) in all the fusion relevant cases.

Phase difference measurement.

Figure 3.1 shows the general scheme for plasma density measurement: a laser beam is divided by a beam splitter into two beams, one that pass through the plasma, named *scene beam*, and the other, the *reference beam*, that cover the same optical path outside the plasma.

The change in the phase of the scene beam is proportional to the electron density integrated through the plasma:

$$\phi_p = \frac{2\pi}{\lambda}\int_l (\mu_{\text{v}} - \mu_{\text{ord}})dl \simeq \frac{\lambda e^2}{4\pi c^2 \epsilon_0 m_e}\int_l n(l)dl \simeq (2.82 \times 10^{-15}\lambda)\int_l n(l)dl \tag{3.3}$$

where μ_{v} is the vacuum refractive index, λ is the wavelength of the beam and $n(l)$ is the local density along the line l. The phase difference ϕ_p can be measured by means of interferometric technique with a scheme displayed in figure 3.3. The so-called *heterodyne* measurement requires that a laser or microwave beam of radiation probing the plasma is divided into two components: the *scene* and the *reference* beams where the reference one

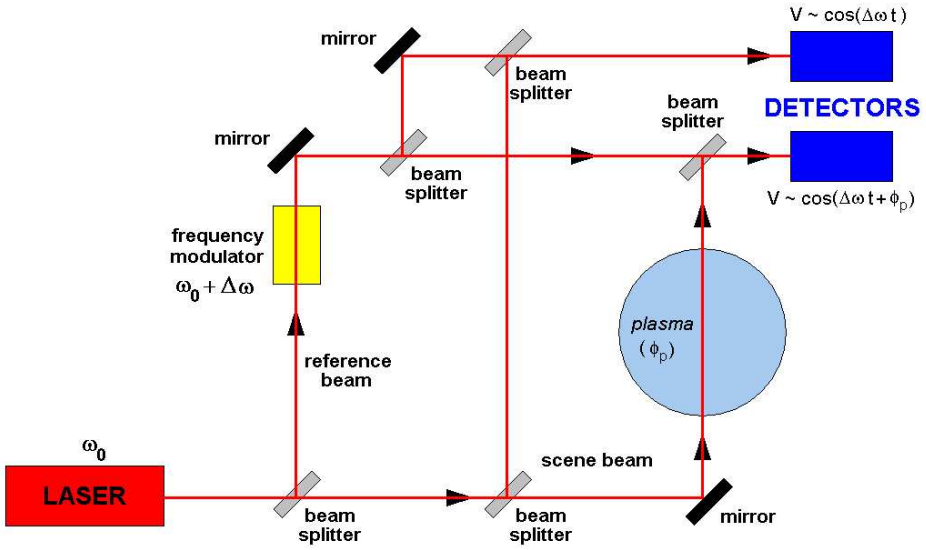

Figure 3.1: Schematic layout of the interferometer. The laser beam of frequency ω_0 is split into two beams, and recombined at the detectors. The plasma introduces a phase delay ϕ_p proportional the the plasma density. The frequency modulation $\Delta\omega$ generates a beating signal, improving the reliability of the measurement.

is shifted in frequency of a quantity $\Delta\omega$. Recombination of the reference and the scene beam produces a beat signal at the difference frequency $\Delta\omega$. One can obtain the phase shift due to the plasma ϕ_p comparing the signal from a couple of beams probing the plasma to the interference signal of a couple of beams passing outside the plasma. The analytic value of the phase difference ϕ_p is given by equation (3.3), from which the line integral of the density may be deduced. The beat frequency is chosen to be sufficiently high to allow a good time resolution in the phase measurement and sufficiently low to be electronically tractable (typically 10 kHz - 100 MHz for infrared systems [8]).

As already stated, the relation (3.1) requires that the wavelength probing the plasma should be short enough. On the other hand, the requirement that the interferometer should be sensitive to the electron density and insensitive to mechanical vibrations favors long wavelengths, as discussed in the following.

$$\phi_p \simeq (2.82 \times 10^{-15}\lambda)\int_l n(l)dl \Rightarrow \int_l n(l)dl \simeq \frac{3.50 \times 10^{14}}{\lambda}\phi_p = \bar{n}L_p \quad (3.4)$$

where L_p is the optical path length in the plasma and $\bar{n}$ is the mean line plasma density. When mechanical vibrations change the optical paths of the

reference beam relative to the scene beam of a quantity δL an error phase difference is induced:

$$\phi_{err} = \frac{2\pi\delta L}{\lambda} \tag{3.5}$$

Hence the relative error $\frac{\phi_{err}}{\phi_p} \propto \frac{1}{\lambda^2}$.

For typical fusion plasma parameters: $\bar{n} = 10^{20}\mathrm{m}^{-3}$, $L_p = 1$ m, $\delta L = 5\mu$m, in order to have a relative error lower than 1% the wavelength should be $\lambda > 100\mu$m. This condition counteracts the *transparency condition* that requires short wavelengths.

The choice of the radiation wavelength is then determined as a compromise between these competing requirements: for typical fusion plasma parameters, wavelengths of the order of hundreds of micrometer are chosen.

Two-color vibrations compensation technique.

The two-color or vibrations compensation technique allows using shorter wavelengths, extending the measurable density range and reducing the risk of a fringe jump (that occurs when a too large variation in density induces $\phi_p > 360°$ between two samples). The effects of vibrations on interferometric measurements is eliminated in principle using two coaxial lasers at different wavelengths. The phase differences ϕ_{err} due to a modification of the optical path δL depends on λ (eq. (3.5)). Using two different wavelengths λ_1 and λ_2, the total phase differences due both to plasma and to vibrations, are respectively:

$$\Phi_1 = \phi_{1p} + \frac{2\pi\delta L}{\lambda_1} \tag{3.6}$$

$$\Phi_2 = \phi_{2p} + \frac{2\pi\delta L}{\lambda_2} \tag{3.7}$$

By a linear combination of the two latter equation one obtains:

$$\Phi_1\lambda_1 - \Phi_2\lambda_2 = K(\lambda_1^2 - \lambda_2^2)\int_l n(l)dl \Rightarrow \int_l n(l)dl = \frac{\Phi_1\lambda_1 - \Phi_2\lambda_2}{K(\lambda_1^2 - \lambda_2^2)} \tag{3.8}$$

where $K = 2.82 \times 10^{-15}$, as defined in equation (3.3). In equation (3.8) the effects of the vibrations is canceled.

3.1.1. RFX-mod interferometer

The main measurements of electron density on RFX-mod is provided by two color, Mid InfraRed (MIR) interferometer [21, 22]. The interferometer, shown in figure 3.2, is composed by 2 modules mounted on the same structure (a C shaped granite frame, with dimensions 3x2x0.2 m and mass 3 tons approximately). Granite has been chosen for its good dimensional stability

and to eliminate any interaction with magnetic fields, since the table is inserted between the magnetizing and field shaping coils of the machine. The table is supported by a stainless steel structure on 6 pneumatic vibration insulators. The interferometer stands on a carriage-rail system by which it can be easily inserted/extracted from the experiment for maintenance of both the diagnostic and the machine. The two faces of the granite bench host respectively the laser and the optical components. Only non-magnetic materials (Aluminium, stainless steel or brass) have been used for the optical mounts, which are all lockable. All the components are then mounted on interface stainless steel plates, which can be easily modified or substituted, for the maximum flexibility of the optical scheme. In the present configuration the module A measures the central zone of the plasma with 8 horizontal or nearly horizontal double-pass chords, whereas module B, with its 6 chords, is mainly dedicated to the outer plasma region on the low field side. The original designed of module B provided 8 chords but actually chords 3B and 5B are not yet installed. Figure 3.3 shows the active chords scheme and the table reports the impact parameter h, defined as the distance from the centre of the chamber, and the poloidal angle Θ for each line of sight.

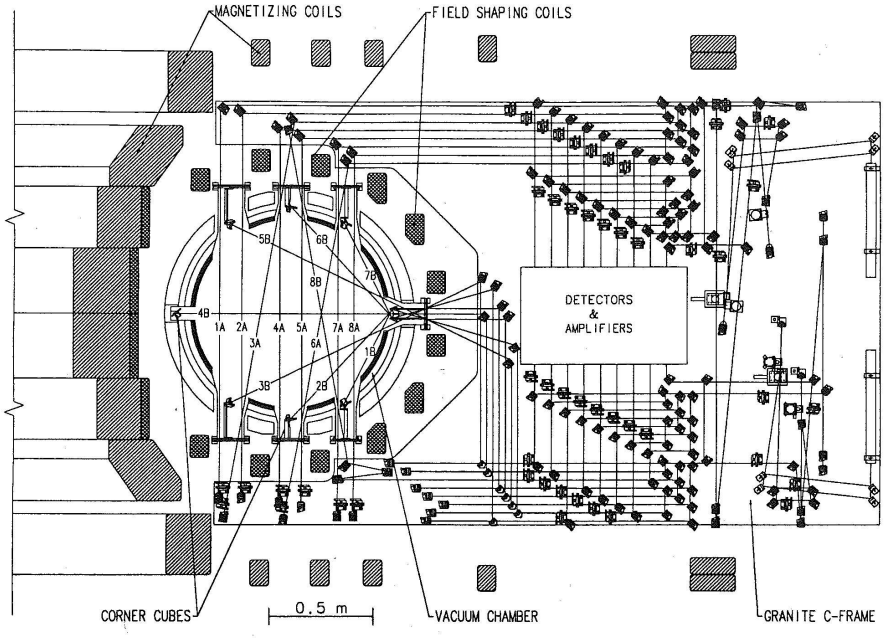

Figure 3.2: Drawing of the front side of the interferometer with components and optical scheme for module A and module B.

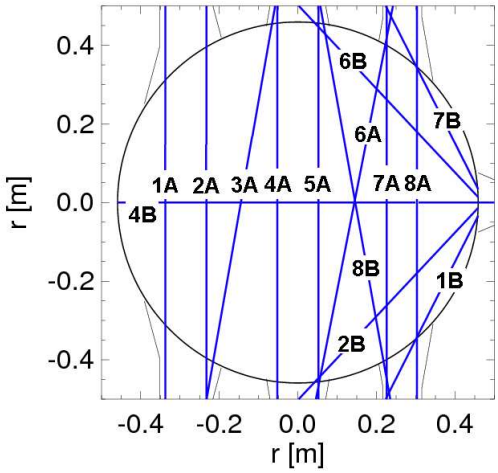

chord	**1A**	**2A**	**3A**	**4A**	**5A**	**6A**	**7A**	**8A**
h(m)	-0.3375	-0.233	-0.143	-0.053	0.053	0.144	0.226	0.304
Θ (°)	0.0	0.0	-9.9	0.0	0.0	-11.1	0.0	0.0
chord	**1B**	**2B**	**4B**	**6B**	**7B**	**8B**		
h(m)	0.425	0.344	0	0.344	0.425	0.144	-	-
Θ (°)	-26.8	-43.2	90	43.2	26.8	10.1		

Figure 3.3: Scheme of the two modules of the RFX-mod interferometer. The table shows, for each chord, the impact parameter h and the poloidal angle Θ.

Module A

The module A, installed since the beginning of activity of RFX, uses a CO_2 laser ($\lambda = 10,58$ μm; output power $P_{out} \simeq$ 10W) for the measure and a HeNe laser ($\lambda = 3,39\mu m$ for the compensation; output power $P_{out} \simeq$ 5mW). Each color is split into a beam scene and a reference beam. A Bragg cell provides the frequency modulation at 40 MHz, to perform the heterodyne measurement, as shown in figure 3.1. All the mirrors and the optical components of module A are mounted on the granite frame. The scene beam is divided in 8 chords that pass twice into the plasma. After that, each beam interferes with its own reference beam and the interference signals are sent to automatic gain amplifiers, with 10 MHz passing band centered at 40 MHz. The amplified signals are sent to electronic phase comparators that give back, for each chord and for each wavelength, a signal proportional to $\sin(\phi_p)$ and an other proportional to $\cos(\phi_p)$. The error on ϕ_p due to phase comparators is less than 0.5° [47]. The main source of error is related to the not completely compensated mechanical vibrations caused by the quickly varying magnetic field induced during machine operation. The average measurement error, estimated as RMS of the signal at the end

of the discharge, is less than $1 \times 10^{17}\mathrm{m}^{-3}$, as shown in figure 3.6.

The signals are acquired by two different systems: the first one by means of "slow" ADC, with sampling rate of 10 kHz and buffer memory of 16 kB per channel. The second system has a sampling rate of 250 kHz, thanks to fast acquiring modules. They can perform real time data elaboration, supplying also an analogical output signal proportional to the electronic density, that it could be used, as example, in a feedback system to control of the plasma density (e.g. acting on the gas valves). The data acquired by the highly reliable, low sampling rate system, guarantee the density measure even if the fast modules fail the acquisition.

Module B

The RFX-mod plasma is characterized by a central zone with almost flat profile, and by an external ring of thickness of some centimeters in which strong gradient and high levels of density fluctuations are present. The chords of the module A, mostly cross the plasma in the central zone as shown in the figure 3.3. The module B, installed in 1996, has been designed to study with high detail the edge plasma region. The most external chords of module B (i.e. 1B and 7B) are 21 mm far from the first wall, as average. Chord 8B is the only one with low impact parameter: it provides the central density when the module A does not work. All the other chords enter and exit the vacuum chamber through the same equatorial port and are reflected back by metal corner cubes fixed inside the vacuum chamber, as shown in figure 3.4

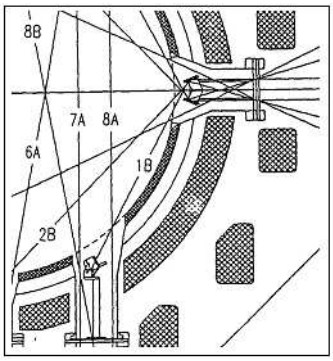

Figure 3.4: Detail of the optical scheme for the chords of the module B that enter the chamber from the equatorial port.

The corner cubes mounted inside the vacuum chamber are subjected to high level of vibrations. To compensate the vibrations a two color scheme has been designed. The main laser is a CO_2 laser similar to the one of module A whereas the compensation radiation is provided by a CO laser ($P_{out} = 1$W, grating tuned at 5.4 μm). The CO wavelength is short enough

to allow a good evaluation of the vibration but is long compared to the He-Ne used in module A. The longer wavelength is important to keep the interferometric signal stable, since the dependence of the interference signal to misalignment of the beams is approximately inversely proportional to the wavelength. Moreover, in order to correct the error usually present in two-color interferometers due to mechanical vibrations of non-shared optical components, a local oscillator has been implemented: a chord, named 0B, passing outside the plasma is acquired in order to subtract its signal to the other chords. To follow the greater and faster plasma fluctuations and the mechanical vibration due to the invessel components an high sampling rate is needed: the module B is sampled at 250 kHz. Despite the large vibrations amplitude, the residual error seen in the line integral is less than 2×10^{18} m^{-2} which is an acceptable error for each chord of the module B.

Main features of the RFX-mod density

Figure 3.6 shows the mean line density along each chord of the interferometer for the VS pulse #22781 of RFX-mod. The density range of RFX-mod is $1 \div 10 \times 10^{19}$ m^{-3}. The shape of the density profile can be computed by an inversion code, as explained in paragraph 3.2.1. Anyway an estimator usually used to evaluated the shape of the density profile is the so called *peaking factor* P_f (sometimes only P). The peaking factor is defined as the ratio between the density measured by a central chord and the density seen by an edge chord, typically:

$$P_f = \frac{\mathrm{ne}_{4A}}{\mathrm{ne}_{1A}} \tag{3.9}$$

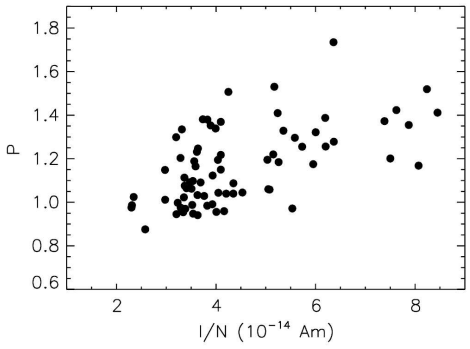

Figure 3.5: Increasing trend of the peaking factor versus the I/N parameter

In RFX-mod P_f assumes values in the range $0.9 \div 1.4$, indicating that the profile is variable. It depends on many conditions, as shown for example in chapter 5. In the past [33], the peaking factor of RFX density profile

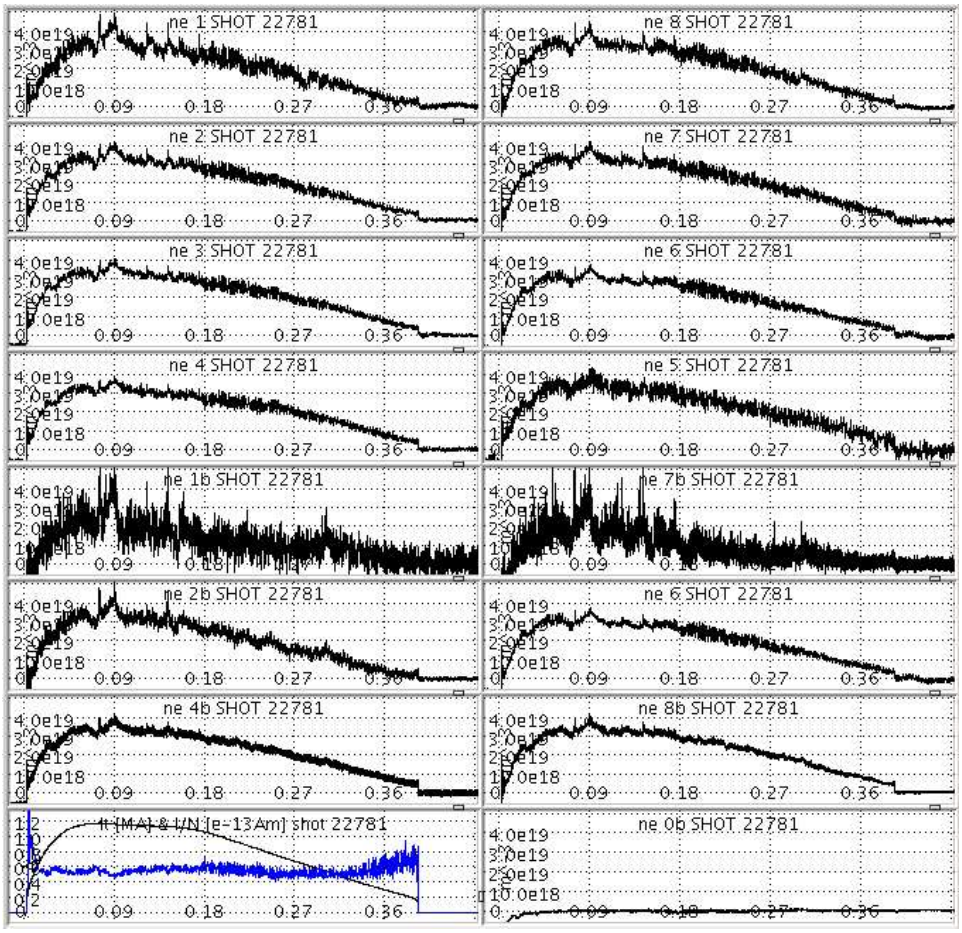

Figure 3.6: Average line density along the 14 chords of the RFX-mod interferometer for 1.2 MApulse #22781. Current and I/N parameter are also displayed.

showed a strong correlation with the I/N parameter, where I is the plasma current and N is the line density ($N = \int_A \mathrm{ne}_{4A} dA = \mathrm{ne}_{4A}\pi a^2$, A is the plasma poloidal cross section): P_f increases with I/N, meaning that peaked profiles ($P_f \geq 1$) are obtained at high current and low density, whereas *hollow* profile ($P_f \leq 1$, characterized by a higher density at the edge than in the centre) can be achieved in high density operation. The same behaviour has been found in RFX-mod [48, 49], as shown in figure 3.5

3.1.2. TPE-RX interferometer

The TPE-RX machine operates in a density range lower than the RFX-mod one: $1 \times 10^{18} \leq n_e \leq 1 \times 10^{19}$. The TPE-RX density is measured by a MIR two color compensated interferometer [27]. The lasers are similar to

the ones of module A of RFX-mod: a CO_2 laser ($\lambda = 10.6\mu$m) provides the measure beam, whereas a HeNe laser ($\lambda = 3.39\mu$m) is used for the compensation of the vibration. The plasma density is measured by means of two vertical lines of sight: a central chord and an edge chord, with normalized impact parameter 0 and 0.69, respectively. To partially heal measurements error, a third chord that act as local oscillator is installed. The bandwidth for the signals is 10 MHz, thanks to heterodyne detection at 40 MHz and the sampling rate is 250 kHz. The experimental setup entails double pass measurements: the beams are sent in the chamber, reflected back by corner cubes mounted inside the chamber and collected by mirrors that send them back to interfere with the reference beams. All the optical components are fixed on a granite frame, with the exception of the corner cubes: these elements are subject to high amplitude vibration during machine operation. The resolution of measurement of the line integrated density is as good as 1×10^{18} m^{-2} and the typical relative error on the central chord is $\leq 8\%$.

3.2 Numerical tools

3.2.1. Electron density profile: the inversion code.

The electron density profile can be reconstructed starting from interferometric line integral data by means of an inversion code. The inversion algorithm developed at RFX [33] determines the best fit of the measurements using a simple class of analytical functions. In order to avoid amplifications of the measuring errors, it has been chosen to keep the number of free parameters of the fitting function less, or equal to half, the number of measuring chords. In the present set-up of the RFX-mod interferometer 14 chords are available, but some of them have the same impact parameter (figure 3.3), so that the number of chords with different impact parameters is 10, which leads to introducing only 5 parameters in the fitting algorithm. The function depends on the radial coordinate ρ, which is the normalized radial coordinate relative to a circle horizontally shifted by Δ and with a radius $r_p = a - \Delta$:

$$n(\rho) = n_0 - (n_0 - n_a - n_1)\rho^\alpha - n_1\rho^\beta \tag{3.10}$$

for $1 < \alpha < \beta$, $0 \leq \rho \leq 1$. As stated, the density profile depends on the 5 parameters n_0, n_1, α, β and Δ. Peaked or hollow profiles can be described, respectively, with $0 < n_1 \leq n_0 - n_a$ and $n_1 > n_0 - n_a$, as shown in figure 3.7. It is clear that, with the choice made, more complex density profiles with, for example, flux points or more than one peak cannot be reproduced.

The inversion algorithm consists in varying the α, β, Δ parameters on a grid, and choosing the n_0 and n_1 values with a least square method. For each set of parameters, i.e. for each profile, the line integrals $N_i(h_i)$ are

computed. The best fitting profile is chosen minimizing the quantity:

$$\chi^2 = \sum_{i=1}^{N} \frac{[N_i(h_i) - I_i]^2}{\sigma_i^2} \tag{3.11}$$

where I_i are the experimental values and σ_i the related errors of chord with impact parameter h_i. The error σ_i are computed as the root mean square of the line integral signal. The density profiles whose $\bar{\chi}^2$ is lower than $(\chi^2 + 1)$ are considered as the "error bar" of the best inverted profile.

Typically the shift Δ is varied in step of 1 mm in the range $-0.5 \div 1$ cm. The α parameter ranges between 1.5 and 30 in step of 1 and β between 1 and 80 in step of 5. Figure 3.8 shows the output of the code. A characteristic RFX-mod hollow profile is shown [33]. In the example the plasma pulse

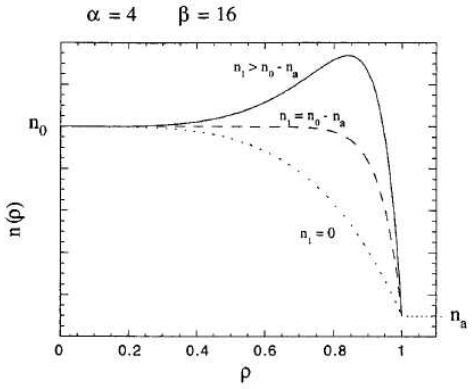

Figure 3.7: Examples of profiles obtained with the inversion algorithm, with the class of function (3.10).

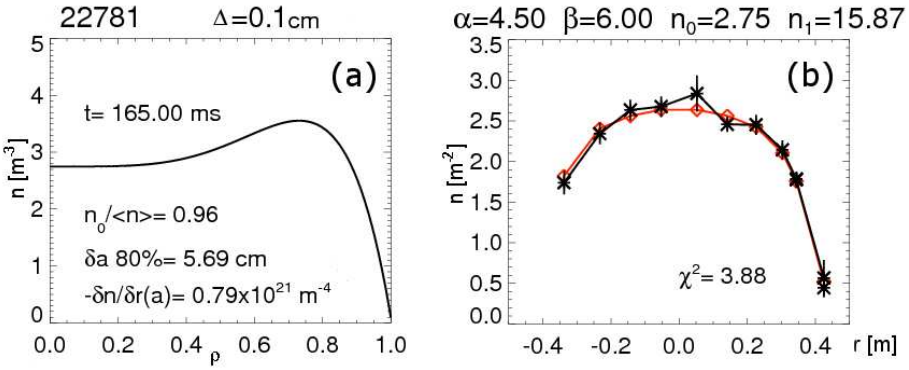

Figure 3.8: Example of graphic output of the inversion code: (a) example of an inverted profile. In panel (b) the comparison between I_i (black line and asterisks and error bars) and N_i(red line with diamonds) is shown.

22781 is inverted at 165 ms. The profile has an hollow shape, with higher density at $r/a \sim 0.8$. The magnetic shift Δ is 1 mm, the other parameters are $\alpha = 4.50$, $\beta = 6.00$, $n_0 = 2.75\text{m}^{-3}$ and $n_1 = 15.87\text{m}^{-3}$. In panel (a) the inverted profile and its important main features are shown: the ratio of the central density n_0 with the mean volume density $\langle n \rangle$, the distance between the 80% of the maximum density value and the wall ($\delta a 80\%$) and the edge gradient $\frac{dn}{dr}|_{r=a}$.

3.2.2. TED: TEmperature and Density.

Several studies [33, 50] have shown that the transport model described in chapter 2 is able to reproduces with good agreement the experimental density profiles. In these studies the value of the transport coefficients is obtained solving, by means of a one dimensional transport code TED (acronym of *TEmperature and Density* [51]), the continuity equation for the density 2.17, rewritten here for reference:

$$\frac{\partial n(r,t)}{\partial t} = -\nabla \cdot \Gamma(r,t) + S(r,t) \tag{3.12}$$

where $\Gamma(r,t)$ is the particle influx and $S(r,t)$ is the particle source term. The computation of the particle source will be described in the paragraph 3.2.3. The particle flux inside the plasma is parameterized as:

$$\Gamma(r,t) = -D(r,t)\frac{\partial n(r,t)}{\partial r} + V(r,t)n(r,t) \tag{3.13}$$

where D is the diffusion coefficient and V accounts for the pinch term. In the TED code, the parameterization of D and V is provided by the user, according to the transport model that have to be tested and the equation (2.17) is numerically integrated.

If a *stationary* solution is needed (i.e. $\frac{\partial n(r,t)}{\partial t} = 0$) at each temporal step of the evolution of the density profile, the code compares the actual profile with the previous one. If the difference between the two profiles is below a certain threshold, the simulation ends: a stationary profile has been reached. At the end of the simulation the χ^2 of the final density profile is computed, comparing the experimental line integrals with the simulated ones. When the χ^2 of the simulation is similar or lower than the χ^2 of the inverted profile, the simulation is considered correct.

In *evolutive* configuration the experimental time evolution of the density is compared with the modeled density evolution obtained as the integration of the equation (3.12). In this case the temporal evolution of D and V is tuned to agree at each time with the experimental density. The quality of the agreement is evaluated with the χ^2 computed at each time on the line integral data.

3.2.3. Computation of the particles source: NENÈ .

The particle source term S in equation (2.17) is the number of charged particles produced, per unit of volume and time, by ionization events. In a hydrogen plasma, when no external fuel is supplied and the contribution of impurities is negligible, the ionizations are the result of the collisions between the hydrogen atoms recycled at the wall and the electrons of the plasma. The source term S can be expressed as

$$S(r,t) = R_I(T(r,t))n_e(r,t)n_n(r,t) \tag{3.14}$$

where R_I is the electron impact ionization reaction rate that depends on local temperature, n_e is the electronic density and n_n is the neutral atoms density. Since n_e is measured by the interferometer and R_I is tabulated [52, 53], a code to computed the diffusion of neutral atoms in fusion plasma has been developed.

The model, named NENÈ [54], is a MonteCarlo code and is based on the work presented in ref. [55]. In the NENÈ code the plasma is assumed to be infinite and symmetrical in the toroidal direction. This symmetry can be assumed in RFX if the analyses concern plasma regions far from the LM position, where the plasma is greatly distorted. In this case the profiles of the plasma parameters, such as density and temperature, depend only on the radius r, which varies from zero to the minor radius a, because they can be considered also poloidally symmetric. NENÈ accounts for the charge-exchange reaction (CX), electron impact ionization and reflection of neutral atoms by the first wall. The plasma is divided into M concentric cylindrical surfaces of radius r_j and the plasma parameters between two adjacent surfaces are kept constant. Hence the plasma is divided into M concentric zones of volume $V_j = 2\pi^2 R_0 \Delta r^2$, where $\Delta r = r_j - r_k$, with $k = j - 1$.

The test particle follows a straight trajectory in the plasma until it has a collision with a ion, an electron or the wall. The path length between two collision is evaluated by the following relation:

$$\int_0^l \frac{ds}{\lambda} = -\ln \xi \tag{3.15}$$

where ξ is a random number uniformly generated in the interval $[0, 1]$ and λ is the local mean free path:

$$\lambda = \frac{v}{n_e(R_{CX} + R_I)} \tag{3.16}$$

v is the atom thermal velocity and R_{CX} is the charge exchange rate [56].

When the test particle ends the path l, if it did not collide with the wall, it can be ionized by electron impact or has a charge exchange as a consequence

of a ion-neutral scattering. In order to choose the reaction, a random number ζ is generated uniformly between 0 and 1 and compared with the charge exchange probability $P_{CX} = \frac{R_{CX}}{R_{CX}+R_I}$. If $P_{CX} > \zeta$ the charge exchange occurs, otherwise the atom is ionized and a new test particle is launched in the plasma. Ionization and charge exchange reaction rates are displayed in figure 3.9 as function of the particle energy, i.e. of the temperature. If

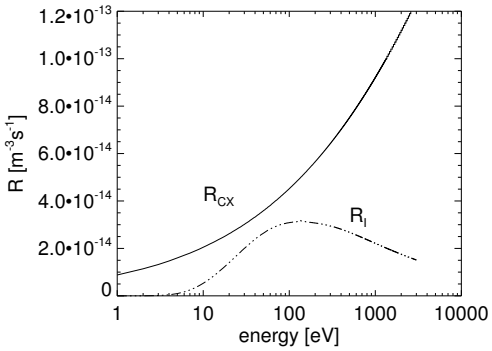

Figure 3.9: Charge exchange and electron impact ionization reaction rate for Hydrogen atom.

the particle hits the wall, its interaction is modeled using the result of the TRIM (TRansport of Ions in Matter) code [57] a program for simulation of sputtering, ion reflection, and ion implantation in structureless solids. It gives the probability of implantation and reflection as functions of incident energy and angle besides of the particle mass and wall material. If a particle reflects on the wall the code follows it, otherwise it stops its path and a new particle is generated.

When all the N test particles end their path in the plasma, the neutral density $\tilde{n}_j$ in the j-th zone is computed as

$$\tilde{n}_j = \frac{1}{V_j} \sum_{i=1}^{N} t_{ij} \tag{3.17}$$

where t_{ij} is the time spent by the i-th particle in the j-th zone. Figure 3.10 shows a test particle trajectory in the plasma with two CX reactions, a reflection and the position where the particle is ionized.

3.2.4. Tearing eigenfunctions reconstruction and FLiT: Field Line Tracing.

In RFX-mod the B_r and B_ϕ magnetic field components measured at the shell are used by a code based on the solution of the Newcomb equilibrium equation [58] which computes the internal tearing eigenfunctions in toroidal geometry for a force-free plasma with circular cross section. In the model, in

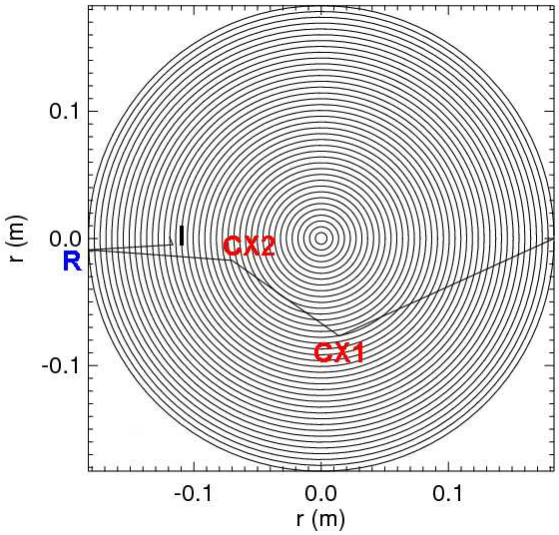

Figure 3.10: Poloidal projection of the trajectory followed by a neutral test particle in the plasma. The two CX reactions, the reflection (R) and the ionization (I) positions are highlighted.

order to properly take into account the toroidal geometry, flux coordinates (r, θ, ϕ) are adopted together with the contravariant representation of the magnetic field via two independent potentials F and Ψ:

$$\boldsymbol{B} = \nabla F \times \nabla\theta - \nabla\Psi \times \nabla\phi \tag{3.18}$$

The radial coordinate r is the radius of the unperturbed flux surfaces whose centres are shifted on the equatorial plane relatively to the shell centre by the quantity Δr. The two independent potentials are Fourier decomposed up to the maximum m and n allowed by the 48x4 measurements :

$$F(r, \theta, \phi) = F_0(r) + \sum_{n \neq n,m} f^{m,n}(r) e^{(m\theta - n\phi)} \tag{3.19}$$

$$\Psi(r, \theta, \phi) = \Psi_0(r) + \sum_{n \neq n,m} \psi^{m,n}(r) e^{(m\theta - n\phi)} \tag{3.20}$$

The model solves a systems of Newcomb-like equations in the two independent potentials for the modes with the same n-number, coupled by toroidicity. The contravariant components of the magnetic fields are finally computed by the relations :

$$B^\theta = \frac{1}{\sqrt{g}} \frac{\partial \Psi}{\partial r} \qquad B^\phi = \frac{1}{\sqrt{g}} \frac{\partial F}{\partial r} \qquad b^r = \frac{1}{\sqrt{g}} \left(\frac{\partial F}{\partial r} + \frac{\partial \Psi}{\partial r} \right) \tag{3.21}$$

where g is metric tensor $1/\sqrt{g} = \nabla r \times \nabla\theta \cdot \nabla\phi$.

Once the internal tearing eigenfunctions have been computed they can be used as input for a field line tracing code which evaluates the local degree of magnetic stochasticity in the plasma. To this end a Field Line Tracing code (FLiT) has been developed [59]. We preserved in the computation of the internal field line trajectory the toroidal geometry solving the field line equation in the same flux coordinates. In these coordinates the field line trajectories have been computed integrating the field line equations in the contravariant components:

$$dr = \frac{b^r}{|\boldsymbol{B}|}dl \qquad d\theta = \frac{B^\theta}{|\boldsymbol{B}|}dl \qquad d\phi = \frac{B^\phi}{|\boldsymbol{B}|}dl \tag{3.22}$$

In the previous equations the module of the magnetic field $|\boldsymbol{B}|$ is computed considering the metric of the toroidal coordinates:

$$|\boldsymbol{B}| = \sqrt{g_{rr}b^r b^r + g_{\theta\theta}B^\theta B^\theta + 2g_{r\theta}B^r B^\theta} \tag{3.23}$$

CHAPTER 4

Transport analysis on TPE-RX.

The global transport properties of a magnetic confinement device are strongly affected by the level of magnetic fluctuations, as stated in chapter 2. In order to damp the amplitude of the MHD modes, the technique of the Pulsed Poloidal Current Drive [36] (PPCD, introduced in paragraph 2.3.1) has been applied on TPE-RX plasma. The comparison of the confinement properties in discharges with and without PPCD are presented in this chapter. Despite the lack of spectrometric measurements, an estimate of the Z_{eff} has been obtained by computing a global helicity balance. The result is that, even if the impurities contribution to electron density is not negligible both in standard and in PPCD pulses, the PPCD pulses shows longer particle confinement time.
Moreover particle transport analysis in standard and PPCD discharges have been carried on, including the effect of impurities. The comparison of the result confirms the strong reduction of the transport when the magnetic fluctuations are damped.
In the last section an analysis on particle confinement in PPCD plasma pulses with injection of iced Deuterium pellets is presented, comparing the particle confinement time in discharge with and without pellet.

Magnetic fluctuations are intrinsic to the RFP, since the configuration is maintained by a strong dynamo mechanism, explained in paragraph 1.3.5, which converts part of the energy externally supplied to the poloidal magnetic field component B_θ into energy associated with the toroidal component B_ϕ. This process regenerates toroidal magnetic flux lost by resistive diffusion. Magnetic fluctuations in the RFP are then intimately connected to the

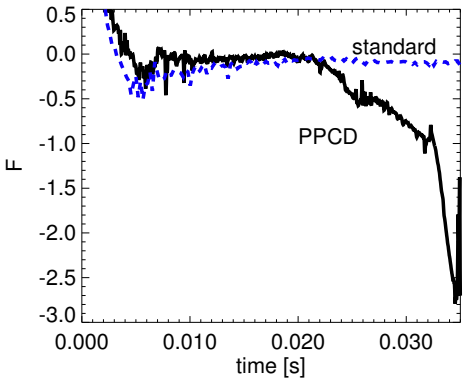

Figure 4.1: Reversal parameter for standard and PPCD pulse.

dynamo, and in standard conditions they are somewhat unavoidable. Unfortunately the magnetic perturbations have a global negative effect: they lead to the stochastization [35] of the equilibrium magnetic field over a large part of the plasma core (see figure 2.3).

In order to reduce the amplitude of the magnetic fluctuation, the Pulsed Poloidal Current Drive (PPCD) has been applied to the TPE-RX plasma. This technique, presented in paragraph 2.3.1, consists in driving poloidal currents inductively by pulsing current in the toroidal field coils: this modifies the internal density current profile, reducing the free-energy source for the tearing modes, hence their amplitude. The effect of low level of MHD modes amplitude on particle transport is presented in this chapter.

4.1 300 kA standard and PPCD discharges at TPE-RX

The TPE-RX PPCD system [39] consists of 6 capacitor banks that allow to drive the additional current on the toroidal field coils. For the pulses analyzed in this chapter the first bank starts at 18 ms and the last at 32.5 ms. The effect of this technique on the toroidal magnetic field is shown in figure 4.1: the reversal parameter $F = \frac{B_t(a)}{\langle B_t \rangle}$, becomes deeper and deeper with an almost constant slope up to 32.5 ms when the sixth, more energetic bank, is connected and F reaches a very deep value. In the figure, the comparison between standard and PPCD value of F is displayed.

The transport analysis presented in this chapter have been carried on standard and PPCD Deuterium plasma pulses at $I_p = 300$ kA, $\langle n_e \rangle \approx 5 \times 10^{18}$ m^{-3}, typical central electron temperature T$_e \geq 200$ eV and $F \simeq -0.1$.

4.1.1. Main plasma parameters

Figure 4.2(a) shows the plasma current, the density behavior, the electron density peaking factor P_f (defined as the ratio of the density measured by the central chord and by the edge chord), the amplitude of the main $m = 1$ tearing modes and the toroidal average particle influx computed from the D_α brightness signals for a standard discharge, whereas figure 4.2(b) shows the same plasma parameters for a typical PPCD pulse.

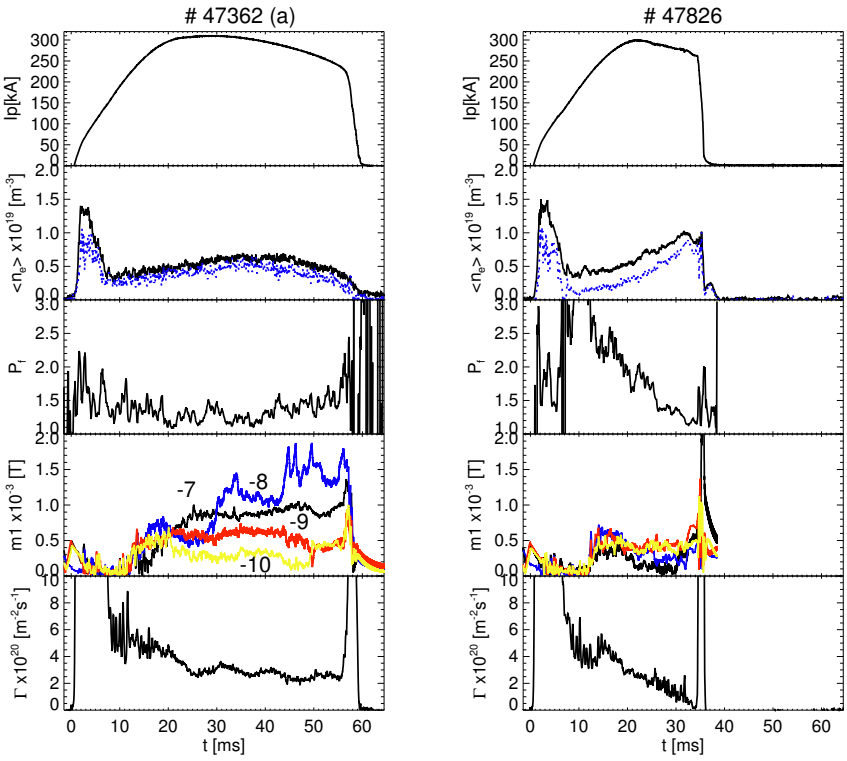

Figure 4.2: 4.2(a) standard shot #47362, 4.2(b) PPCD shot #47826 parameters: plasma current; line integral density signals (solid line: central chord; dashed line: edge chord); peaking factor of the density profile; amplitude of the $m = 1$; $n = 7 - -10$ tearing modes and toroidal average particles influx.

In standard discharge, the flat-top phase of the plasma current and the electron density lasts for about 30 ms. The shape of the density profile, evaluated with the peaking factor P_f does not change during the plasma pulse: its value of about 1.5 means that the profile is centrally peaked.

The $m = 1$ MHD tearing modes, displayed in the fourth panel, start their growth after the ionization phase of the pulse, at about 10 ms. Their amplitude, quickly saturates and remains generally stable up to the end of

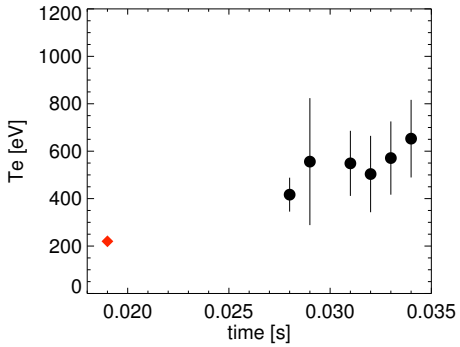

Figure 4.3: Temporal trend of central electron temperature Te(0). Each point is averaged on many PPCD discharges. Red diamond represents standard case and full circles represent the PPCD discharges.

the pulse: only the $m = 1; n = 8$ shows some negligible variations that do not affect the magnetic topology.

The last panel in figure 4.2 shows the particles influx Γ from the first wall. After the ionization, the influx stabilizes at a value in the range $2 - 4 \times 10^{20}$ m^{-2} s^{-1} up to the end of the discharge.

The central electron temperature for this discharge is $T_e(0) = 220$ eV, measured at 34 ms.

Concerning the PPCD discharge the general behavior is rather different: the PPCD starts at 18 ms and the pulse duration is shorter than the standard one. The discharge ends because of the very deep value of the reversal parameter, when a spontaneous large relaxation event occurs and the current has a sudden termination.

The electron density starts increasing after 18 ms, reaching a central mean value of about 1×10^{19} m^{-3}. The profile changes from peaked to flat, as shown by the evolution of the peaking factor that ranges from $P_f \simeq 2$ to $P_f \simeq 1$.

The amplitude of the MHD modes is similar to the standard discharge up to the application of the PPCD: after 18 ms the modes appear strongly damped: indeed their amplitude is less than half the amplitude of the standard case. Moreover the measurements of the on-axis electron temperature by means of the Thomson scattering shows an increasing trend: as displayed in figure 4.3, in the PPCD phase the Te(0) increases from standard value (200 eV, red diamond) up to more than 600 eV at the end of the pulse. In figure 4.3 each point is the average over about 10 shots with same setup and same timing of the TS. The error bars represent the standard deviation of the data set. The red diamond is representative of the standard discharge value, hence of the pre-PPCD temperature, and the error is very small,

thanks to the good reproducibility of standard pulses.

Considering the higher n_e and T_e we can see that the reduction of the magnetic perturbation, responsible for transport, during the PPCD phase brings the plasma in a good confinement regime. Another confirmation of the good confinement regime induced by the PPCD is the behavior of the influx: after the ionization it decreases till the end of the discharge as a consequence of the reduced particle loss. Moreover the deformation of the plasma column due to the phase and wall locking of the MHD modes (Locked Mode - LM) is strongly reduced during the PPCD, as demonstrated in figure 4.4: after the start of the PPCD action, the particle influx is generally damped and in particular does not show the strong localized plasma-wall interaction that is a characteristic sign of the LM.

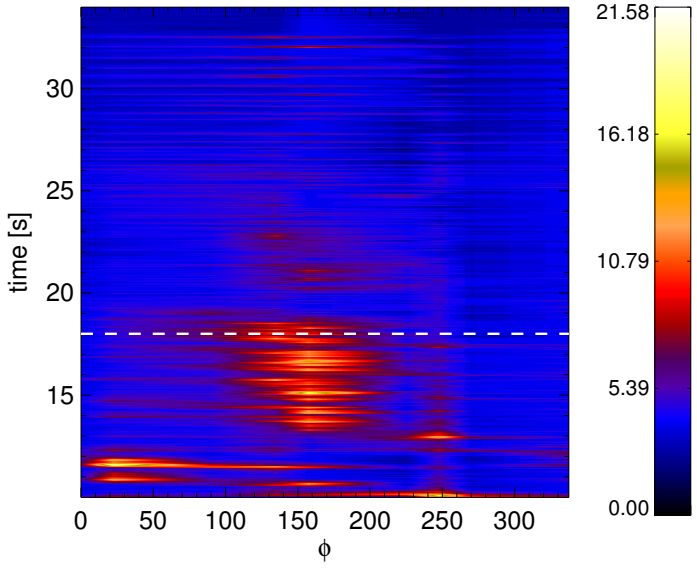

Figure 4.4: Toroidal distribution of the Deuterium influx [a.u.] versus the pulse time in the PPCD discharge: after the PPCD application the influx is strongly reduced. The dashed line indicates the stating time of the PPCD.

4.1.2. Helicity balance and Z_{eff}

Absolute calibrated measurements of impurity concentration are not available at TPE-RX. In order to get an estimate of the Z_{eff}, we used a method based on the *helicity balance* [60].

Taylor theory [10] describes the RFP magnetic configuration assuming

the conservation of the total helicity

$$K = \int \boldsymbol{A} \cdot \boldsymbol{B} dV \tag{4.1}$$

where $\boldsymbol{A}$ is the vector potential and integral is on the torus volume V. Nonetheless, both magnetic helicity and energy would decay over the longer resistive time scale. In particular, in laboratory experiments, the plasma volume cannot generally be regarded as a closed system since voltages are applied to create and maintain the magnetic distribution. The power required to keep constant the total helicity is

$$P_k = \frac{I_p}{\Phi} \int \eta \boldsymbol{j} \cdot \boldsymbol{B} dV \tag{4.2}$$

where Φ is the toroidal magnetic flux, $\boldsymbol{B}$ is the total magnetic field, $\boldsymbol{j}$ is the current density and η is the plasma resistivity. For a fully relaxed state with, it turns out that $P_k = P_{\text{OHM}}$ i.e. no extra power is required to maintain the helicity content of the magnetic configuration, whereas for a partially relaxed state, typically $P_k > P_{\text{OHM}}$. For typical profiles, P_k is about twice the amount corresponding to Ohmic dissipation of the plasma current I_p, given by $P_{\text{OHM}} = \int_V \eta j^2 dV$, and can better explain the experimental values of the loop voltage.

A rough estimate of the Z_{eff} can hence be obtained equalizing P_k to the total input power $P_{\text{IN}} = V_{\text{loop}} I_p$ (V_{loop} is the loop voltage) and computing the resistivity η. Using its Spitzer form η_{Sp}, the Z_{eff} value can be calculated:

$$\eta_{Sp} = \left(0.53 \times 10^{-4} \ln \Lambda\right) Z_{\text{eff}}(r) T_e(r)^{-3/2} \tag{4.3}$$

where $\ln \Lambda = \ln(T_e^{3/2} / \sqrt{\pi} Z e^3 n_e^{0.5}) \approx 15$ is the Coulomb logarithm. The Z_{eff} is defined as:

$$Z_{\text{eff}} = \frac{\sum (Z_i^2 n_i)}{\sum (Z_i n_i)} \tag{4.4}$$

being n_i the density of the ion of charge eZ_i. Its radial profile, used in eq. (4.3), is taken flat [61]. Using equation (4.2) the effective charge of TPE-RX plasma results $Z_{\text{eff}} \simeq 4$.

4.1.3. Impurity concentration

Typical impurities present in fusion machine with metallic first wall are Oxygen and metal, such as Iron, Chromium, Tungsten, Molybdenum. In TPE-RX machine, the plasma heat and particle flux is mainly concentrated on the Molybdenum limiters, hence erosion processes due to physical sputtering are reasonably acting during plasma pulses. Moreover the low density regime of TPE-RX and the high V_{loop} allows the presence of a large population of suprathermal electrons that enhances the erosion of the limiters. For

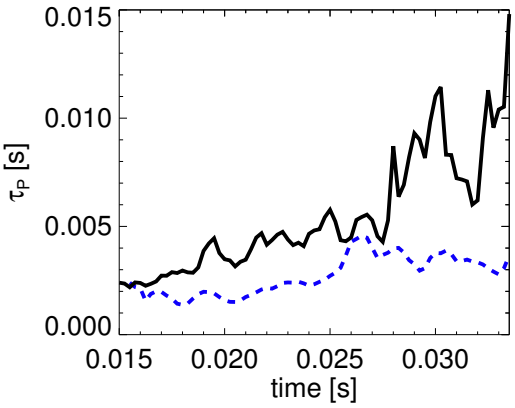

Figure 4.5: τ_P for standard discharge (dashed line) compared to τ_P trend in PPCD pulse (solid line).

these reasons the assumption of Molybdenum as main impurity in TPE-RX plasma is reasonable.

To compute the electron density contribution from Molybdenum ions, the atomic collisional radiative model [62] has been used: the main species for TPE-RX standard plasma parameters is MoXVI. The Z_{eff} value, from equation (4.4), implies that the Molybdenum 15^+ ion density n_{Mo} is about 1.5% of the electron density n_e and the principal gas ion density n_D is about $80\% n_e$.

This means that we cannot assume, as usual, that $n_D = n_e$ because the impurity contribution to n_e is not negligible hence $n_e = n_D + Z_{Mo} n_{Mo}$, where $Z_{Mo} = 15$ is the impurity ion charge.

4.2 Particle confinement time τ_P and transport analysis

4.2.1. Particle confinement time

The particles confinement time is a good indicator of the quality of the confinement for a certain plasma configuration. It is defined as $\tau_P = N/(\Gamma_{tot} - (dN/dt))$, where N is the total number of particles in the plasma, $\Gamma_{tot} = \langle\Gamma\rangle A_t$ is the total influx from the wall ($A_t = 4\pi^2 a R_0$ is the total surface of the torus). During the flat top of the standard case the dN/dt term is negligible, while in the PPCD case it has a positive value up to the end of the pulse. Nevertheless the most important contribution to the computation of the τ_P comes from the influx: in the standard discharge it remains stable, whereas in the PPCD discharge it is strongly damped at least by a factor 10.

Figure 4.5 shows the comparison of the τ_P computed for the standard

and PPCD discharges. The dashed line represents the standard case: $\tau_P \approx 3$ ms for all of the discharge.

The estimate of the τ_P during the PPCD (solid line in figure 4.5) is much more difficult because the electron temperature increases, as shown in figure 4.3: further ionization of impurities present in the plasma releases electrons, increasing the n_e value measured by the interferometer. This adds to the effect of the probable higher confinement of Deuterium ions. Hence we cannot simply state as in the standard discharge $n_D \simeq 0.8 n_e$. In order to know the total number of Deuterium atoms N, and its variation in time $\frac{dN}{dt}$, one should distinguish the two different contributions to the electron source. The Molybdenum present before the PPCD is sufficient to account for all the electron density increase measured by the interferometer: T_e rises up to 600 eV and, according to the collisional radiative model, the main impurities ions change from MoXVI to MoXXV, releasing 9 electrons for each atom, on average. Because of these large uncertainties on the actual n_D temporal evolution during the PPCD, we estimate the lower limit of τ_P considering that all the growth in particle content seen by the interferometer is due exclusively to the ionization of the Molybdenum ions, hence the deuterium content does not change during the discharge. Even under this extremely conservative assumption, the reduced amplitude of the magnetic fluctuations leads the plasma to a high confinement regime, characterized by low level of Deuterium influx from the first wall Γ_{tot} and high value of τ_P that increase at least by a factor 5: it rises up to 15 ms at the end of the pulse, as shown in figure 4.5.

4.2.2. Transport analysis

Particle transport analysis of the main gas has been carried on the standard discharge of TPE-RX, with temperature and density radial profiles displayed in figure 4.6. According to remarks expressed in paragraph 4.1.3, $n_D = 0.8 n_e$. In panel (b) both ion and electron density are displayed: n_D is the simulated density, whereas n_e is measured and used to compute by NENÈ the diffusion in the plasma of the neutral atoms, evaluating the particles source radial profile. The temperature profile is taken with the same shape of the density profile, as shown in figure 4.6 (a).

The low density level and the mild density gradient at the edge (r/a > 0.8) allow a deep penetration of the neutral atoms. Hence the particle source, even if it has its maximum at r/a≈ 0.9, is able to reach the centre of the plasma, as shown in black line, in figure 4.7(a). The central particle source and the transport mechanisms, presented in the following, result in the peaking of the density profile.

The radial profile of the diffusion coefficient is parameterized as

$$D(\rho) = D_{st} \cdot (1 - \rho^6) + D_e \cdot \rho^{10} \mathrm{m}^2\ \mathrm{s}^{-1} \tag{4.5}$$

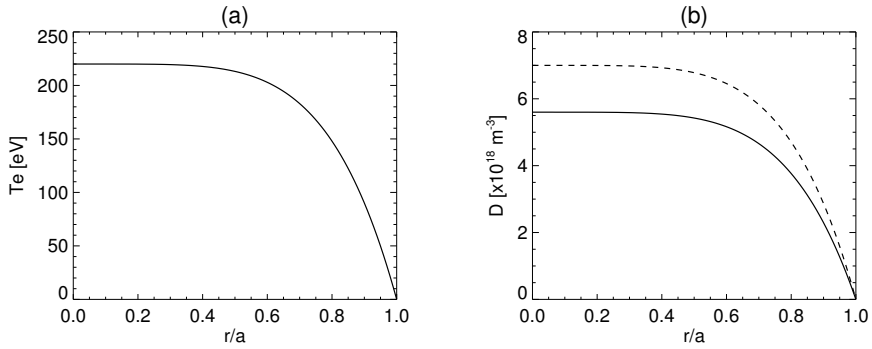

Figure 4.6: Temperature (a) and ion density (b) radial profiles for transport analysis on standard shot #47362. The dashed line in plot (b) represents the electron density radial profile, used to computed the particle source.

where D_{st} is the diffusion coefficient proportional to the magnetic fluctuation level and D_e is the electrostatic term acting at the edge of the plasma, as presented in section 2. The best fit of interferometric data is obtained by the D profile displayed in figure 4.7(b). The error bars are represented by the Grey area: each profile within the area is compatible with the experimental data within $\chi^2 + 1$. The diffusion coefficient needed to maintain the central density is $D_{st} = 6.75 \pm 0.30$ m^2 s^{-1} whereas the gradient at the edge, according to the parameterization $D_e = (\frac{\Gamma_{tot}}{\partial n/\partial t})$, is sustained by $D_e = 2.3 \pm 0.5$ m^2 s^{-1}. We can conclude that the region of good confinement in TPE-RX in standard configuration is the edge region, beyond the reversal radius. The stochastic centre, where dynamo modes are resonating, is affected by higher level of transport.

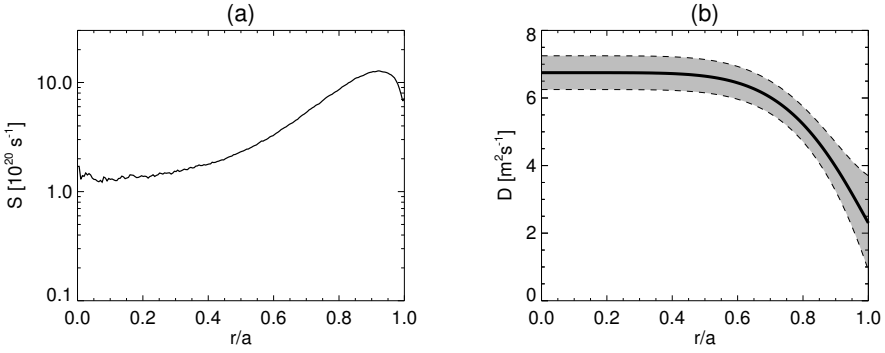

Figure 4.7: (a) Particle source and (b) diffusion coefficients radial profile. Shaded area represents the error bars for the diffusion coefficient radial profile.

Concerning the PPCD shot, the analysis has been carried out considering the assumptions stated in paragraph 4.2.1. In this way we have found the upper limit for the diffusion coefficient, because only the effect of a reduced Deuterium influx is considered.

The simulation has been carried out in evolutive configuration of the TED code, modifying the D_{st} and D_e values in order to keep the content of Deuterium in the plasma constant, while the influx goes down. The simulation starts at t=15 ms, before applying the PPCD and it follows the discharge till the end of the pulse. The electron density n_e increases in agreement to the interferometer data and it is used to evaluate the ionization of the Deuterium neutral atoms from the wall.

The results are displayed in figure 4.8: D_{st} (a) and D_e (b) have a similar trend, going from typical value of standard discharges before the application of the PPCD, down to less than 1 m^2 s^{-1} when $t > 32.5$ ms and the diffusion becomes comparable to neoclassical prediction. In particular the D_{st} experiences beneficial effects of the reduced stochasticity: at the end of the PPCD its value is reduced of a factor ~ 10.

It is interesting to note that the effect of the PPCD is visible since 18 ms: the D_{st} suddenly decrease to half of its standard value, in agreement to the damping of the magnetic modes (see figure 4.2), resonating in the core of the plasma. The D_{ed} is slightly less affected by the application of the PPCD: a possible explanation is that the electrostatic fluctuations, responsible of the edge diffusion, experience only the indirect beneficial effect due to reduction of the global level of fluctuation [63]. Anyway the low spatial resolution on density radial profile, especially at the edge, due to the presence of only two chords in the interferometer, does not allow us to discuss in more details the transport properties at the edge of TPE-RX plasma.

We can state that the reduction of the magnetic perturbation extends inwards the region of good confinement of the RFP configuration: the central stochasticity is reduced and the particle transport becomes comparable with neoclassical prediction along the whole minor radius.

4.3 Pellet injection experiment: plasma performance.

At the end of the present chapter first evidences of good confinement in PPCD discharges with pellet injection are presented. In this section the density behaviour and the particle confinement time after pellet injection in standard discharge is compared to that in PPCD pulses [64].

On TPE-RX a cryogenic pellet injector is installed. It is composed of a double layer cryostat. In the external chamber liquid Nitrogen cools down inner volume that is filled with liquid Helium. A system of 5 heaters keeps the temperature in the correct range in order to obtain a soft mixture of iced Deuterium. A piston presses the mixture extruding a single pellet per shot. Once the pellet is created, a metallic blade cuts a cylinder approximately 1

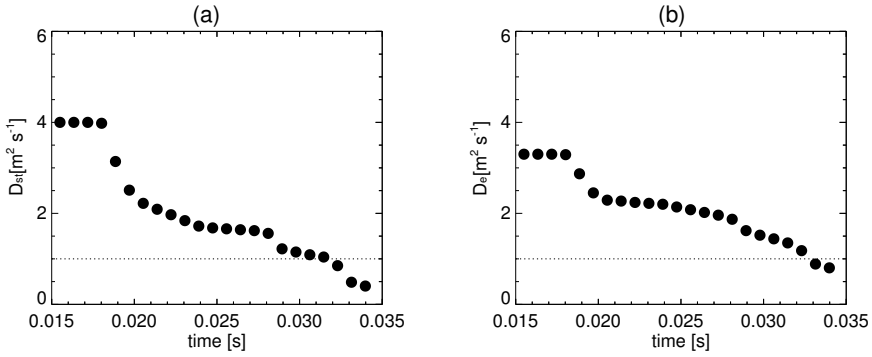

Figure 4.8: Temporal trend of the (a) stochastic and (b) electrostatic diffusion coefficients during the PPCD phase. The dashed line indicates the neoclassical limit.

mm long and then the temperature is lowered in order to harden the pellet. The pellet mass is typically $m_p \leq 10^{20}$ atoms. The pellet is injected radially from a horizontal port of TPE-RX, with an inclination of 10° downward in order to correct the deflection owing to the rocket effect during the ablation, allowing ablation closer to the plasma centre. A pneumatic system accelerates it at a maximum velocity of about 450 m/s. The mass of the pellet is measured by means of a resonant microwave cavity and the velocity is computed by the time of flight between an optical detector and the cavity. The trajectory of the pellet in the plasma in the poloidal and toroidal directions is reconstructed by a 4 channels position sensitive device (PSD) [65], whereas the radial position is computed assuming constant radial speed during the ablation. Figure 4.9 shows the launch geometry and the position of the main component described above.

4.3.1. density evolution: standard and PPCD discharges

Approximately 150 pellets have been launched in TPE-RX 300 kA plasma during the campaign. A subset of well diagnosticated 15 pulses has been selected to perform the analysis. The subset is representative of the whole database for pellet mass and velocity, as shown in figure 4.10. Left and right panels in figure 4.11 display the main plasma parameters respectively for a standard and for a PPCD discharge, compared with similar discharges with pellet. When a pellet is launched in a standard shot the density and the D_α line brightness increases in about 1 ms and. After the ablation, an enhanced recycling from the wall is observed, as highlighted by the D_α increase, that lasts for about 10 ms. Also the density recovers its original value in about 10 ms, therefore the particles deposited by the pellet are completely lost after that time. The behaviour in PPCD pulses is different: without the pellet the phenomenology is already well known and discussed in detail in previous

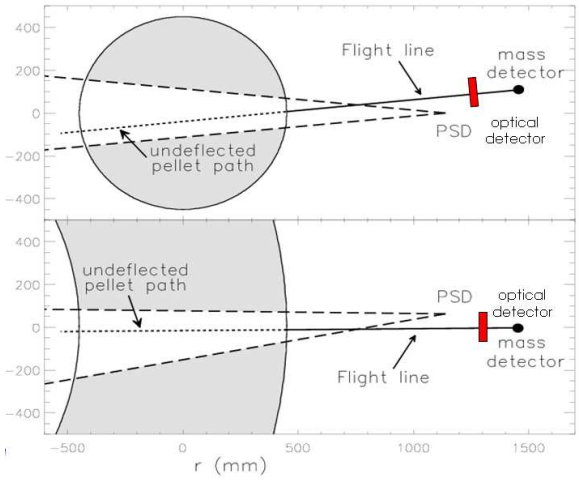

Figure 4.9: Geometry of the launch line of the pellet injector of TPE-RX. The upper panel presents a poloidal view whereas the lower one shows a toroidal section.

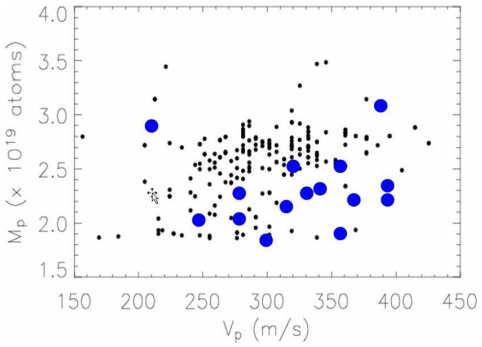

Figure 4.10: Complete pellet database. Blue dots represent the subset of 15 shots on which the analysis has been carried out.

sections. Concerning the shot with pellet, after the ablation the D_α signals decrease but the density stabilizes at a value about 3 times higher than the pre-injection level, confirming that the good confinement regime induced by PPCD is not destroyed by pellet injection. This is not obvious because after a pellet enters the plasma an enhanced MHD activity is usually observed [51] as a dynamo relaxation event where the internally resonant $m = 1$ tearing modes tend to increase as well as the $m = 0 - n = 1$ mode resonant at the reversal surface.

The particle confinement time τ_p in discharge with pellet has been computed neglecting the presence of impurities because the additional source, provided by the pellet, dilutes their concentration and cool down the plasma, making the further ionization negligible: indeed in pellet pulses the $Z_{\text{eff}} \simeq 1$

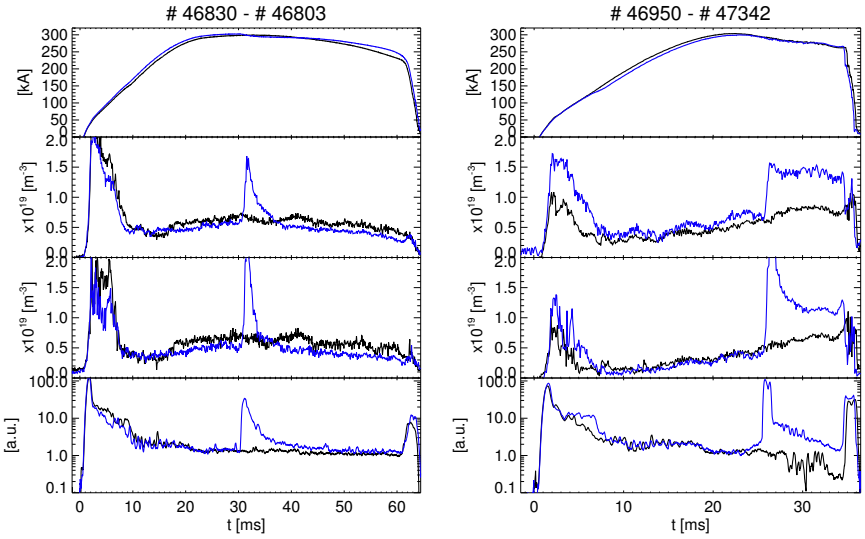

Figure 4.11: Plasma current I_p, central and edge line density and D_α brightness in standard (left) and PPCD (right) with pellet injection (blue traces) and without (black traces).

after the injection. Figure 4.12 displays the comparison between τ_p in different experimental configurations:

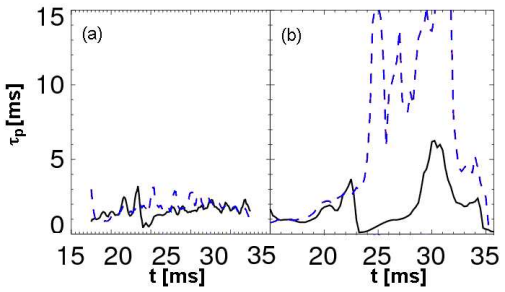

Figure 4.12: Particle confinement time in standard discharges (a) and in PPCD pulse (b). Blue dashed lines represent reference pulses without pellet, black solid lines shows τ_p when a pellet is launched.

In panel 4.12(a) the τ_p of a standard discharge is displayed in dashed blue line and compared to particle confinement time when a pellet is injected (black solid trace) in a similar discharge: the effect of the pellet is a reduction of τ_p due to the increased particle source during the ablation. After approximately 10 ms the effect of the pellet disappears: all the particles released by the pellet are lost and no effect on influx are observed, indeed

the τ_p is comparable to that of the standard pulse without pellet.

In the PPCD discharge 4.12(b) the reference τ_p increases starting from 18 ms, reaching about 15 ms at the end of the pulse. When the pellet enters the plasma, the confinement time drops down to 1 ms but, after the ablation phase, it starts increasing with a trend similar to the reference PPCD discharge, reaching $\tau_p \simeq 5$ ms, twice the standard discharge particle confinement time.

We can conclude that the good confinement properties owing to the reduction of the MHD modes during the PPCD phase are only slightly affected by the pellet injection. Indeed most of the particles released by the pellet in a PPCD discharge are confined inside the plasma.

CHAPTER 5

Toroidal asymmetric transport properties owing to mode locking in RFX-mod.

The particle and energy transport in reversed field pinch experiments is affected by the presence of the tearing modes (cfr. chapter 2), and by their locking in phase. The locking in phase of $m = 1$ tearing modes produces a strong plasma-wall interaction and a consequent high losses of particles that account for a significant fraction of the total particle outflux. The impact of of the locking in phase of $m = 0$ modes is less well-known: the purpose of this chapter is to present a study on the effect of the locking in phase of $m = 0$ modes on the transport properties of the plasma. The locking in phase of $m = 0$ modes modifies the plasma radius, shrinking and enlarging the plasma cross section in two wide toroidal regions of about 100 degrees.

This study has been carried out investigating the shape of the density profile in the RFX-mod experiment. The analysis shows that the profile exhibits a dependence on the deformation of the plasma column: milder density gradients at the edge are found where the plasma column is shrunk and where enhancement in density and magnetic fluctuations at the edge are present. This result can be considered the first experimental evidence of an instability localized where the plasma column is shrunk. This result has been published in [49].

In the past the transport properties and, more in general, the RFP magnetic configuration have been considered toroidally symmetric. The first evidence of the presence of a toroidal asymmetry was the *slinky mode*, a non-uniform helical magnetic perturbation, studied in the OHTE machine. The slinky mode is due to the locking in phase of the MHD modes characterizing the RFP [11]. Indeed their locking in phase forms a toroidally localized structure in the perturbed magnetic field, also called *Locked Mode* (LM, see paragraph 1.3.4).

The m = 1 distortion of the plasma column [66] is responsible for enhanced, plasma-wall interaction (PWI) localized at ϕ_{lock}, which has an indirect effect on global confinement via e.g. the impurity content and Z_{eff} . It has been shown by means of numerical simulations [67] that the phase locking of the $m = 1$ modes, besides causing magnetic stochasticity in the plasma core, is expected to result in a toroidally localized particle loss channel, which punches through the good confinement region located in the vicinity of the field reversal region.

In the past, numbers of studies (e.g. [33]) were aimed at understanding the average transport properties of the plasma, neglecting the effect of LM and of the Last Close Flux Surface (LCFS) deformation. The density profile were determined from interferometric data collected when LM was far $(\phi_{\text{interf}} - \phi_{LM}) > 40^\circ$ from the diagnostic, hence it was not affecting the measurements.

The purpose of the analyses presented in the next two chapters is to study the effects of the LM on the transport properties of RFP configuration.

5.1 Locked mode in VS discharge.

The level and spectrum of magnetic fluctuation in RFX-mod can be well determined thanks to a large set of magnetic field pick-up coils: the system can measure both the toroidal and radial components by means of the magnetic sensors coupled to the active coils system (see paragraphs 1.4.1 and 2.3.1).

As already stated in paragraph 1.3.4, the LCFS of the plasma is distorted by the phasing of both the $m = 0$ and $m = 1$ modes, identifying besides the LM position, two wide toroidal regions, one shrunk and one bulging. Figure 5.1 displays the distance of the LCFS from the first wall in a VS discharge at 600 kA. The point of contact of the plasma surface on the wall is localized at $\phi_{\text{lock}} \approx 95^\circ$, where the δ_1 helical deformation has its maximum. The δ_0 deformation is visible below the δ_1 as a shrunk region at angles $150^\circ \leq \phi \leq 280^\circ$ and a bulging region elsewhere.

In the RFX-mod the VS is very effective in reducing the m = 1, as underlined by the reconstruction of the LCFS [58]: the maximum value of δ_1 is lower than 1 cm, while in the RFX experiment the typical value at 600 kA was $3 \div 4$ cm [66] However, the VS is less effective in controlling the m =

0 modes, because of the geometry of the coils. The effect is that the jump of the plasma bulging in the VS discharges has an average value of 2 cm which is comparable to the values found in RFX.

The VS operation of RFX-mod leads to a significant reduction of the localized PWI, related with total $\delta_0 + \delta_1$ deformation, e.g with the LM. Conversely the amplitude of dynamo modes in the core is reduced by a factor of $2 \div 3$ and their phase locking is still present. Hence these conditions are optimum for analyzing the effect of the LM on transport, discriminating it from the influence of PWI.

5.1.1. The $m = 0$ phasing effects

The VS, being more effective on the $m = 1$ perturbation than on the $m = 0$, highlights the effect of the natural phasing of the$m = 0$ modes. As already stated, the $m = 0$ component modifies the plasma radius in an asymmetric way with respect to ϕ_{lock}. Besides modifying the LCFS radius, the locking in phase of $m = 0$ modes is believed to change also the topology of the magnetic surfaces in the region external to the reversal radius: according to the reconstruction of the flux surfaces presented in [68] and shown in figure 5.2 the bulging region is characterized by large magnetic islands, whose amplitude is reduced in the shrunk region. In this context it seems natural to seek experimental evidence of non-axisymmetric transport effects related to m = 0 phase locking in the RFP. To this end we verified the presence of toroidal asymmetries performing a statistical analysis on the density profiles of RFX-mod. The study had to be carried on paying attention in order to separate pure geometrical effects due to the non-axisymmetric magnetic surfaces from the actual transport effects. Moreover we were aware that the asymmetry of the magnetic configuration might create the conditions for an instability to develop only in a limited region of the plasma torus. This is the case, for example, of the multifaceted asymmetric radiation from the edge instability (MARFE) [69] in tokamak machines. Indeed a recent analysis on RFX-mod radiation pattern [70] suggests that a thermal instability,

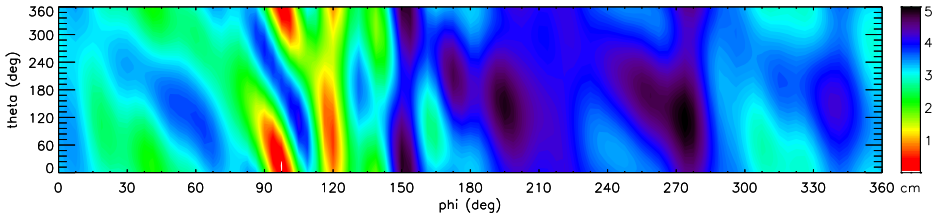

Figure 5.1: Distance of the LCFS from the first wall of RFX-mod: it is clearly visible the LM region with the point of contact and the m = 0 effect with the shrunk and the bulging region

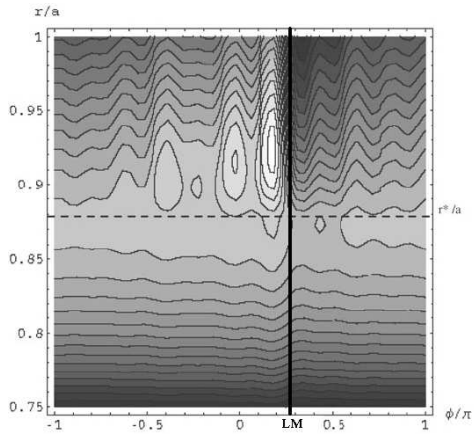

Figure 5.2: Toroidal cross section of the flux-surfaces near the reversal surface. Asymmetric size of the magnetic island with respect to the LM position is clearly visible.

analogous to the tokamak MARFE could be present at the LM position. To investigate if the asymmetry created by the m = 0 modes gives the origin of a localized instability we also analyzed the behavior of density and magnetic fluctuations.

5.2 Density behavior.

For the data analyzed in this chapter only the module A of the interferometer was operational so that the normalized impact parameter h/a of the eight, nearly vertical interferometer chords ranges from 0.05 to 0.74 (see paragraph 3.1.1 for reference). The chords are located both on the high field side and on the low field side of the torus, so that they provide information on the whole plasma cross section. In order to investigate the presence of toroidal asymmetries in the shape of density profiles, a statistical analysis has been performed on a set of about 60 VS discharges at $I_p = 600$ kA and a set of about 15 discharges at 800 kA, whose density is in the range $1.5 - 3 \times 10^{19} m^{-3}$. Generally the interferometer chords with $h/a < 0.6$ measure almost the same line-averaged density, indicating that the density profiles in RFX-mod are nearly flat in the plasma core and that the gradients are located at the edge. As an indicator of the profile shape we used the peaking factor P, defined as the ratio between the time averaged central and edge density (equation 3.9). P is calculated as the ratio between the measurements of the central (h/a = 0.05) and the outermost chord (h/a = -0.74 where the minus stands for the inner side). In figure 5.3, on the left, we show the typical profiles of two discharges at 600 kA with low ($P \approx 1$) and high ($P \approx 1.3$) peaking factors. The data used for each inversion are averaged over a time interval of 20 ms during the plasma current flat top.

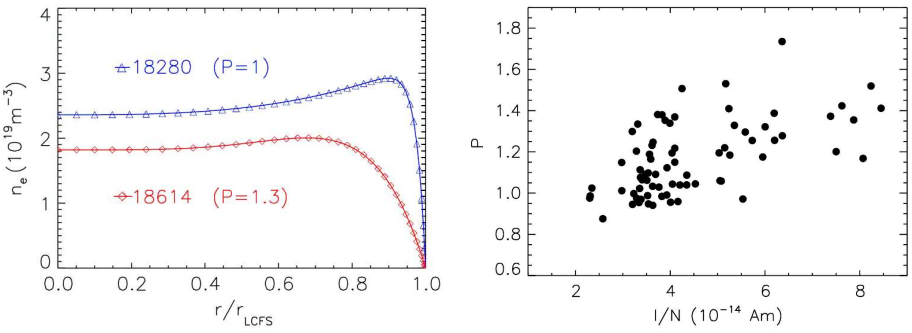

Figure 5.3: Examples of two density profiles at low (P=1) and high (P=1.3) peaking factor (left) and general behavior in RFX-mod: increasing trend of the peaking factor versus the I/N parameter (right)

The two profiles are nearly flat in the core while, as indicated by the different values of P, they differ in the outer region. The profile of pulse 18280 ($P \approx 1$) is edge peaked, i.e. the maximum of the density is in the outer region of the plasma, and the density gradient is localized in a region of a few centimeters from the edge ($r/r_{\rm LCFS} > 0.9$). The profile of pulse 18614 ($P \approx 1.3$) is nearly flat and the density gradient extends up to $r/r_{\rm LCFS} \approx 0.7$. An analogous variation of the profile was previously observed in the RFX experiment [33] as already mentioned in section 3.1.1, where the peaking factor was found to depend mainly on the I/N parameter, whereas no significant dependence on other typical scaling parameters (e.g. the current I or the pinch parameter) had been found. The dependence on the I/N parameter was characterized by a relatively large spread that at that time was related to the conditioning and status of the first wall. The same behavior has been confirmed by analysis on RFX-mod [48]. The two profiles shown in figure 5.3 are an example of this transition, since the discharge 18280 is at $I/N \approx 4 \times 10^{-14}$ Am, while the discharge 18614 is at $I/N \approx 6 \times 10^{-14}$ Am.

Also in RFX-mod the trend is characterized by a significant spread, as it is possible to see on the right in figure 5.3; hence it is likely that there are other factors that contribute to determining the profile shape. The analysis confirmed that this spread is not due to any additional dependence of P on the current, density or on the plasma equilibrium. As an additional piece of information, we observed that the shape of density profiles in RFX-mod depends also on the LM position, since particularly high values of the peaking factor are measured when $280° < \phi_{\rm lock} < 360°$, i.e. when the distance between the interferometer and the locked mode ($\phi_{\rm interf} - \phi_{\rm lock}$) is in the range 0–100 toroidal degrees. This is shown in figure 5.4 for the largest set of discharges having similar values of I/N ($3 < I/N < 5 \times 10^{-14}$ Am), so that the dependence on I/N can be neglected. Unfortunately the lack of sufficient

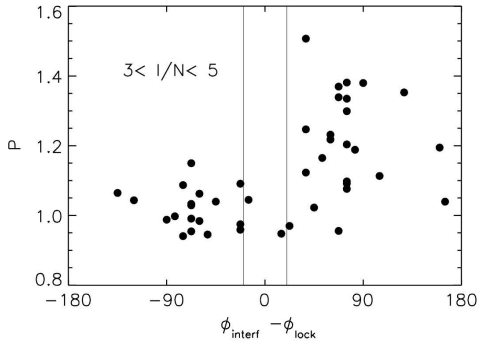

Figure 5.4: Peaking factor as function of the distance between the LM and the interferometer ($\phi_{\text{interf}} - \phi_{\text{lock}}$) for discharges at $3 < I/N < 5 \times 10^{-14}$ Am. The vertical lines define the region where the δ_1 deformation may affect the density measurement.

number of pulses with $\phi_{\text{interf}} - \phi_{\text{lock}} > 90°$ and with ϕ_{interf} - $\phi_{\text{lock}} < -90°$ and the dispersion of the available data do not allow the characterization of density profiles in this region. The region where the highest P values are measured extends beyond the region of 40°, delimited in the figure by the two vertical lines, where the toroidal angle of the maximum value of δ_1 is close to the interferometer and may influence its measurements. Therefore the strong PWI related to the δ_1 deformation cannot be at the origin of the asymmetry. In fact there is no correlation between the amplitude of m = 1 plasma deformation at the position of the interferometer $\delta_1(\phi_{\text{interf}})$ and the peaking factor. However the dependence of the shape of the profile on ϕ_{lock} has been found to be related to the plasma radius perturbation due to the m = 0 modes at the position of the interferometer $\delta_0(\phi_{\text{interf}})$. When $0° < \phi_{\text{interf}} - \phi_{\text{lock}} < 100°$, $\delta_0(\phi_{\text{interf}})$ is negative; hence the interferometer measures at a toroidal location where the plasma column is shrunk, while when $-100° < \phi_{\text{interf}} - \phi_{\text{lock}} < 0°$, $\delta_0(\phi_{\text{interf}})$ is positive; hence the interferometer measures at a toroidal location where the plasma column is enlarged.

The dependence of the profile shape on the plasma radius variation is best highlighted plotting P versus $\delta_0(\phi_{\text{interf}})$ for the discharges at I/N in the range $3 \div 5 \times 10^{-14}$ Am, as shown in figure 5.5. In that figure the red diamonds and the blue triangles represent, respectively, the peaking factor when the in interferometer measures where plasma cross section is shrunk ($\delta_0(\phi_{\text{interf}}) < -2$ mm) and when it is measuring in the bulging region ($\delta_0(\phi_{\text{interf}}) > 2mm$). The black dots represent the data for which $-20° < \phi_{\text{interf}} - phi_{\text{lock}} < 20°$.

It is interesting to note that the dependence of P on $\delta_0(\phi_{\text{interf}})$ exists for all the I/N values of our database, as shown in figure 5.6.

The separation between the two data sets confirms that the highest P

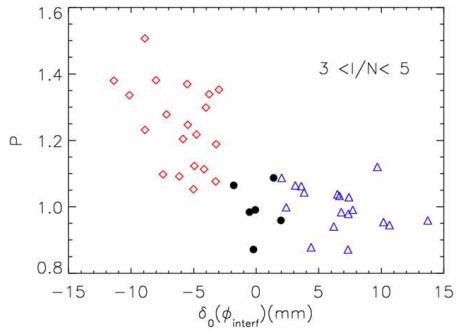

Figure 5.5: Peaking factor as function of the m = 0 deformation at the interferometer toroidal section $\delta_0(\phi_{\text{interf}})$. Red diamond are related to the shrunk cross section and blue triangle with bulging region. Black dots represents the zone closer than 40° to LM.

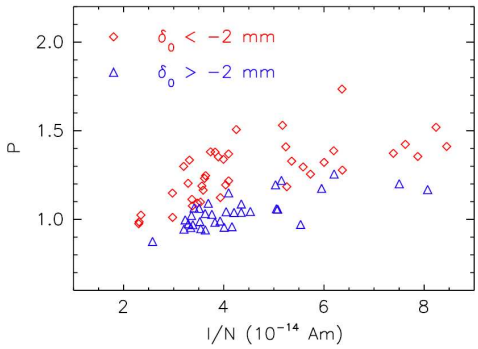

Figure 5.6: Peaking factor versus I/N in the largest range. Color and symbol are the same of figure 5.5.

values are measured when the plasma is shrunk at the diagnostic section, and this effect accounts for an important part of the spread present in the trend of P with I/N. In the subset $3 \div 5 \times 10^{-14}$ Am, the reconstruction of LCFS indicates that the average value of the plasma radius in the shrunk region is 0.432 m, about 1.3 cm smaller than the average value found for the bulging one. One could then make the hypothesis that the separation between the P values shown in figure 5.6 is due to a pure geometrical effect: when the plasma cross section is shrunk the outermost chord is measured in a region more external, and hence with lower density, resulting in higher P values. To clarify this point we determined the typical density profile of the enlarged and of the shrunk region. The interferometer measurements of the discharges with $3 < I/N < 5 \times 10^{-14}$ Am have been averaged, respectively, on the subset of discharges where the column bulges and shrinks at ϕ_{interf} (the classes represented by blue triangles and red diamonds). Then we inverted

the ensemble averaged data with the inversion code presented in paragraph 3.2.1.

The effect of the plasma radius deformation is modeled assuming r_p equal to the value of r_{LCFS} at ϕ_{interf} . The contribution of the non-axisymmetric shift is taken into account considering the plasma column shifted by the sum of the Shafranov shift S and of δ_1 calculated at ϕ_{interf} . The density profiles resulting from these inversions, which are plotted in figure 5.7, can be taken as representative of the average behavior in the regions where the plasma cross section is shrunk and enlarged. It is evident that a greater number

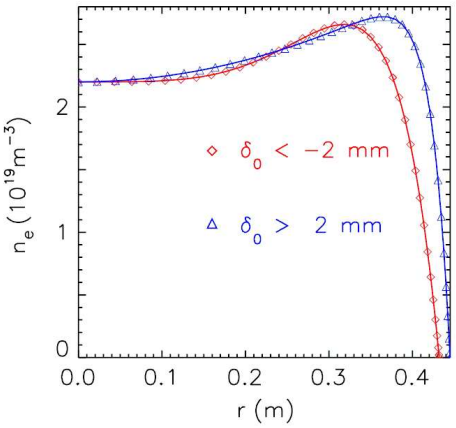

Figure 5.7: Inverted density profiles in the shrunk section of the plasma (red diamonds) and in the bulging one (blue triangles) as function of the plasma radius.

of particles is found in the plasma when the column is enlarged than when it is shrunk. On average about 15% more particles are confined when the plasma is bulging. The comparison between the two profiles plotted versus the radial coordinate normalized to r_{LCFS} (see figure 8(a)) confirms that the difference is far from being purely geometrical; the density profiles in the shrunk and bulging regions are different.

The two profiles are very similar as long as $r/r_{\mathrm{LCFS}} < 0.8$, while in the bulging region the maximum is more pronounced and the density gradient at the edge is steeper. The two ingredients that determine the density profile are the particle source and the particle transport. Since in these pulses no external fueling is applied to the plasma, the particle source is given by the ionization of atoms recycled at the wall. The atom influx, estimated from the measurements of the H_α radiation detector, has a toroidal distribution which is strongly correlated with the non-axisymmetric shift δ_1. As already reported in the case of the RFX machine, particularly high influxes are measured in RFX-mod in a region of about 40° around ϕ_{lock}. It is important underline that, outside this region, the influx does not exhibit any behavior

compatible with an asymmetry related to δ_0. We are then led to conclude that the difference between the density profiles is due to an asymmetry of the particle transport with respect to $\phi_{\rm lock}$. The greater amount of density and the steeper gradient found at $r/r_{\rm LCFS} > 0.8$ in the bulging region indicate that the transport is reduced with respect to the shrunk one. These results confirm the presence of an asymmetry with respect to $\phi_{\rm lock}$ in the particle transport determined by the locking in phase of large scale MHD m = 0 modes. It is worth noting that the effect of non-axisymmetric m = 1 perturbation on the reconstruction of density profiles is negligible, as confirmed by the average value of the local shift, equal to 4mm in both cases, which is analogous to the average value of the Shafranov shift.

5.3 Density and magnetic fluctuations.

Similarly to the density profiles, the fluctuation amplitude has an asymmetric behavior with respect to $\phi_{\rm lock}$ in VS discharges. An example of this dependence is given by the discharges 18330 and 18332 (figure 5.8), having the same density of 2.8×10^{19} m^{-3}. The time traces of this figure refer to the outermost chord of the interferometer (h/a = -0.74), which is the one where the phenomenon is most evident. A high pass filter with a cut-off frequency of 2 kHz has been applied to the density signal, sampled at 10 kHz, to remove the contribution of mechanical vibrations [71]. The fluctuation amplitude of the line-averaged density $\tilde{n}_e$ is higher when $\phi_{\rm lock}$ is in the range $280° \div 360°$, while it is reduced when the modes are locked elsewhere.

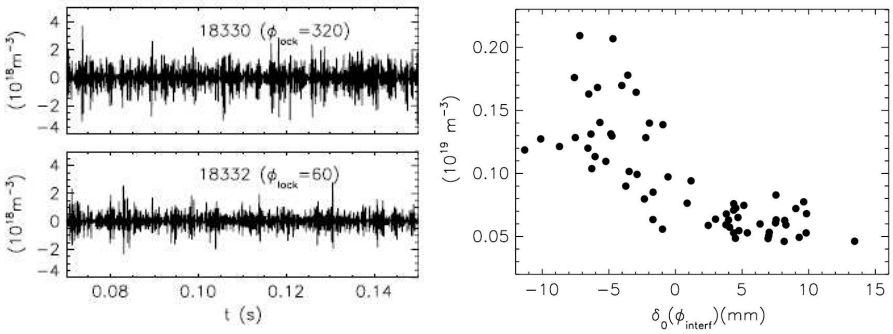

Figure 5.8: Left: time trace of density fluctuation in the shrunk zone (shot 18330) and in the bulging one (shot 18332).
Right: General trend of $\tilde{n}_e$ as a function of m = 0 deformation at the interferometer.

In figure 5.8 the amplitude of $\tilde{n}_e$ fluctuations during the current flat top in VS discharges is plotted versus the deformation of the LCFS owing to m = 0 LM. Two regimes of density fluctuations can be identified along the torus: one of high and one of low density fluctuations. The region of

enhanced fluctuations coincides with the region where the least steep edge density gradients are measured and $\delta_0 < 0$.

The density fluctuations measured by different interferometer chords are always positively correlated among them, but the highest correlation is found in the discharges where the plasma is shrunk at ϕ_{interf} . In these discharges the ensemble averaged correlation index between the outermost chord and the others has a value of about 0.8, which indicates a strong positive correlation. In the other discharges the value of the average correlation index is around 0.5 and corresponds to a medium level of positive correlation. The dependence of the fluctuation amplitude on the plasma shape characterizes all the interferometer chords. Figure 5.9(a) shows the average value of fluctuation amplitude versus the distance of the chords from the LCFS. The average values have been calculated, respectively, on the set of discharges with the plasma shrunk at ϕ_{interf} and on the discharges with the plasma bulging. Both curves show that the average density fluctuation profile n_e

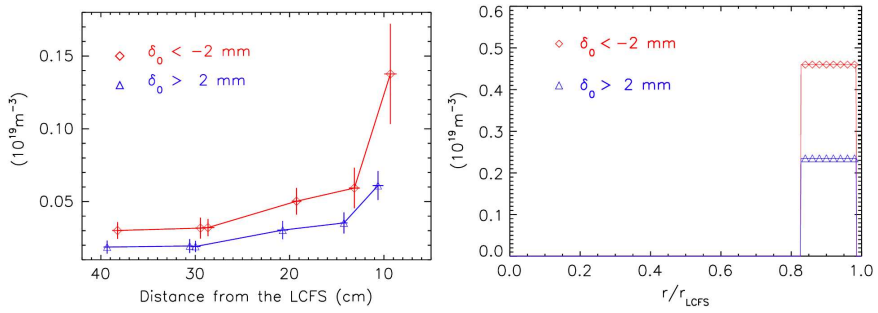

Figure 5.9: Left: average density fluctuation $\tilde{n}_e$ at f ¿ 2 kHz; Right: inverted density fluctuation radial profile compatible with data on the left. Red diamond represent the shrunk region ($\delta_0 < 0$) and blue diamond the bulging one ($\delta_0 > 0$).

is peaked at the edge; hence it can be reasonably assumed that the density fluctuation profile also is hollow. Assuming the fluctuations to be in phase and to have a constant amplitude in a corona, the profiles of figure 5.9(a) are compatible with the presence of fluctuations in a ring, as showing figure 5.9(b), located at $r/r_{\text{LCFS}} > 0.8$. Furthermore edge peaked n_e profiles have been found to correspond to hollow fluctuation profiles in the Madison symmetric torus (MST) [72]. The experimental profiles of figure 5.9(a) and the reconstruction of figure 5.9(b) show that the fluctuations in the shrunk region are enhanced in the outer region of the plasma, at $r/r_{\text{LCFS}} > 0.8$. It is instead more difficult to draw a conclusion on the plasma centre, because the high level of correlation between the core and edge chords may indicate that the measurements of the central chords are dominated by the increase in the edge fluctuations.

To investigate the high frequency behavior, we analyzed a subset of 25 discharges at 600 kA and the discharges at 800 kA, where density measurements sampled at 250 kHz were available. The average power spectra are obtained for toroidal region shrunk and bulging (figures 5.10(a) and (b)). In the frequency band 2–20 kHz the power spectrum is higher in the shrunk region than in the bulging one, for both current levels. In the band 3–10 kHz the difference between the two spectra is particularly large, due to the fact that the spectrum measured in the shrunk region displays a broad plateau, centered at f $\simeq$ 6 kHz. A direct comparison between the two currents is not

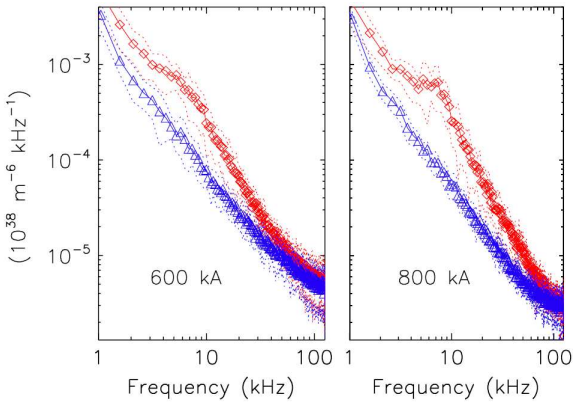

Figure 5.10: Power spectra of $\tilde{n}_e$, measured by the outermost interferometer chord, of discharges at 600 and 800 kA. Colors and symbols have the same meaning of the previous figure.

possible, because the discharges available at 800 kA are only a few and have a different magnetic equilibrium. However the fact that in these discharges the peak is more evident than at 600 kA may indicate that the effect scales with the current. In the same frequency band (3–10 kHz) the coherence between the outermost chords (inboard and outboard, respectively) turns out to be higher for the shrunk region than for the bulging one. This is shown in figure 5.11, where the two curves ($\delta_0 < -2$ mm and $\delta_0 > 2$ mm) are significantly different taking into account the respective uncertainty level shown by the dotted lines. Hence in the shrunk region the fluctuations have longer correlation lengths than in the bulging one. In the same figure we also show the relative phase between the two chords: in this frequency band the poloidal number of the fluctuations is equal to zero.

Such non-axisymmetric behavior around the $\phi_{\rm lock}$ position is also found when analyzing high frequency toroidal magnetic field fluctuations by means of the internal system of integrated sensors (ISIS) diagnostic installed in RFX-mod to investigate the edge of the plasma, introduced in paragraph 1.4.1. The 24 equally spaced pick-up coils are placed in a toroidal array covering the full toroidal circumference, at $\theta = 250°$.

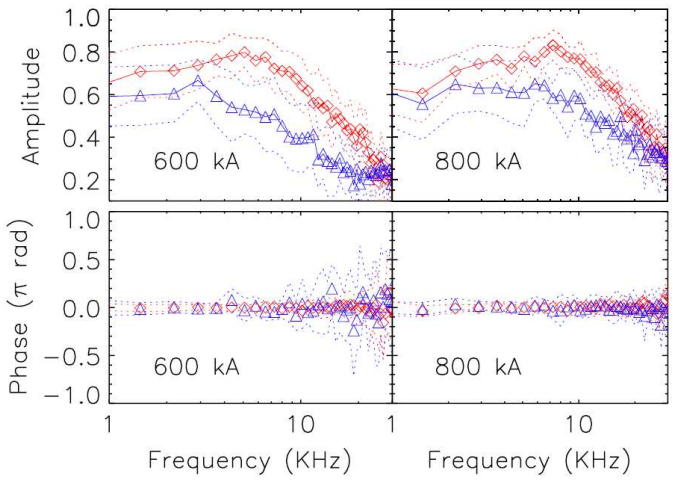

Figure 5.11: Coherence between the most external inboard 1A and outboard chords 8A. Colors and symbols have the same meaning of the previous figure.

In figure 5.12 the power spectra of the signals of a subset of the full ISIS diagnostic, averaged over the same set of discharges at 600 kA considered before, are shown. For each discharge the power spectrum of the probes located at $\phi = \phi_{\rm lock} + 45°$ and $\phi = \phi_{\rm lock} - 45°$ (which correspond, respectively, to shrunk and bulging regions) has been obtained.

The signals have been numerically integrated before processing in order to obtain the time behavior of the edge toroidal magnetic field. The difference between the two conditions is evident, as well as for the presence of a broad plateau around f $\simeq$ 6 kHz as for density fluctuation. In figure 5.13 we show a color-scale plot of the power spectrum calculated for each probe of the toroidal array, obtained for a single discharge. In the figure the position of the LM is indicated by a thick black line. Again it is clear that there is non-axisymmetric behavior of the fluctuation levels in the frequency band 2–20 kHz.

The enhancement of density and magnetic fluctuations can be interpreted as the signature of an instability located in the shrunk region. This is confirmed by the presence of the plateau at about f=6 kHz in both density and magnetic field fluctuation spectra for the shrunk zone, which is not observed in the enlarged one. Furthermore the spatial location of the density fluctuation enhancement indicates that the instability affects the plasma edge.

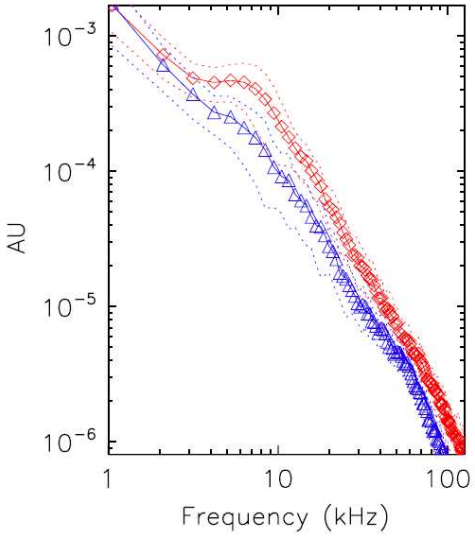

Figure 5.12: Power spectra of the toroidal magnetic field $\tilde{B}_T$. Diamonds are averages of the probe located in the shrunk region and triangles are averages of the probe located in the enlarged region.

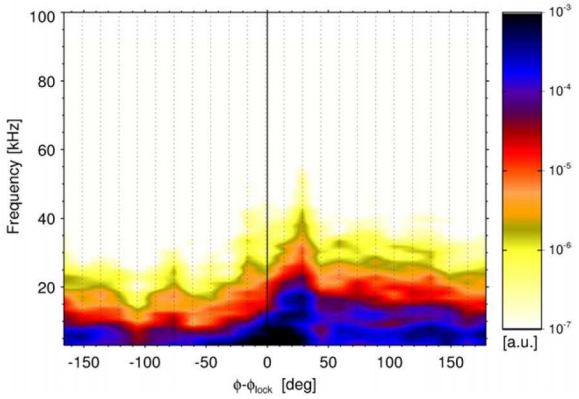

Figure 5.13: Contour plot of $\tilde{B}_T$ power spectra versus the toroidal distance between the LM and the ISIS probes. The vertical dark line in the plot marks the LM position.

Toroidal asymmetric transport properties owing to mode locking in RFX-mod.

CHAPTER 6

Confinement loss during Dynamo Relaxation Event in RFX-mod

The dynamo process that sustains the RFP magnetic configuration can take place either in a nearly continuous or in a discrete way: the so-called Dynamo Relaxation Event (DRE). The asymmetric behaviour presented in chapter 5 is highlighted also by the plasma reaction to DRE. In particular the confinement properties before and during the event are compared in these chapter, highlighting the negative effects on particle confinement due both to the increasing of MHD activity and to the creation of a preferential loss channel close to the LM position, when a DRE occurs. The results presented in this chapter have been published in [73].

In the general contest of seeking experimental evidence of toroidal asymmetry in RFP particle transport properties linked to the presence of the locked mode, the behaviour of electron density during *Dynamo Relaxation Event* (DRE) has been studied. The study of DREs is a topic of general interest because it allows to investigate how the MHD activity influences phenomena like the plasma-wall interaction or the particle and energy transport.

6.1 Dynamo Relaxation Event.

DREs have already been observed in RFX [74] though not very frequently since the machine was characterized by a more continuous dynamo process. The situation has now changed on RFX-mod, with the new magnetic boundary, thanks to the VS operation. In VS the plasma is characterized by a

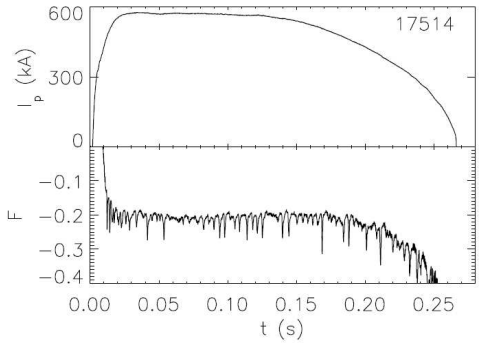

Figure 6.1: Time traces of plasma current and Reversal parameter F. The negative spikes in F correspond to the DRE.

discrete MHD activity with large DREs, similarly to the situation of other RFPs with close fitting thick shell such as the MST experiment.

When the reversal parameter F has values lower than about -0.1, the discharge alternates phases of continuous and discrete toroidal flux generation; in the latter case the generation of the flux is provided by the occurrence of large DREs. In the RFX-mod discharges the DREs are generally found in sequences with a period of 2-3 ms; an example of a typical time trace of the reversal parameter is shown in figure 6.1, together with the plasma current I_p.

The process of flux generation involves the increase of magnetic mode amplitudes. The $m = 1$ modes are destabilized following a cascading process that propagates from the innermost resonant harmonics to outer ones. As an example, in figure 6.2(a) we show the cascading process of the $m = 1$ toroidal field harmonics during a DRE. The process starts with the destabilization of the innermost resonant mode, having toroidal number n=-7 (the blue one in the figure) and then propagates in a sequential way to the harmonics with higher toroidal number. The cascading process lasts a few milliseconds and ends with the almost simultaneous destabilization of the m=0 modes figure 6.2(b) that re-generate the toroidal flux, as marked by the crash of F (figure 6.2(c)). After the crash the mode amplitude rapidly decreases and F recovers its initial value.

The increase in amplitude of MHD modes is associate to an increased deformation of the LCFS: figure 6.3 shows the toroidal profiles of δ_1 and of δ_0. The red profiles in the figure represent the plasma column deformation at t=96 ms (just before the event), plotted versus the toroidal angle relative to the position of the Locked Mode $\phi_{\rm lock}$. The blue profiles are calculated at t = 97.7 ms where the amplitude of the $m = 0$ modes reaches the maximum value and are representative of the DRE effect on the LCFS. The comparison between the profiles shows that the DRE enhances the perturbation of the plasma column without changing the position of the locked mode. The DRE

amplifies the localized helical deformation of the plasma column and modifies significantly the plasma radius in a wide region of about 200 toroidal degrees, shrinking the region where the column is already shrunk and enlarging the area that is bulging. Therefore a DRE can be seen as a strengthening of the locked mode and leads to an enhancement of the typical deformation of the Last Closed Flux Surface.

Statistical analysis has been performed on about 150 DREs. Each DRE has been chosen from one shot as representative of that shot. The whole set of plasma pulses have similar densities ($n_e = 1.5 - 3.0 \times 10^{19}$ m^{-3}), current ($I_p = 600$ kA) and equilibrium ($F = -0.2$). There is a wide experimental evidence that the mode phase-locking causes a localized, strong plasma-wall interaction (PWI) in the region of the LM [75] which is correlated to the deformation of the LCFS. This interaction affects the particle and energy confinement and produces an intense release of particles and impurities from the wall. In agreement with these results it has been observed that a DRE causes in RFX-mod an increase in the amount of neutral atoms released by the wall, as it is described in the following Section 6.2.

6.2 Effects of DRE on the particle influx.

Bursts of hydrogen atoms and impurities have been observed in correspondence of the F parameter crashes. Figure 6.4(a) shows the time trace of the H_α detector signal in a discharge where the neutral influx is correlated with the oscillations of the reversal parameter. However this correlation is

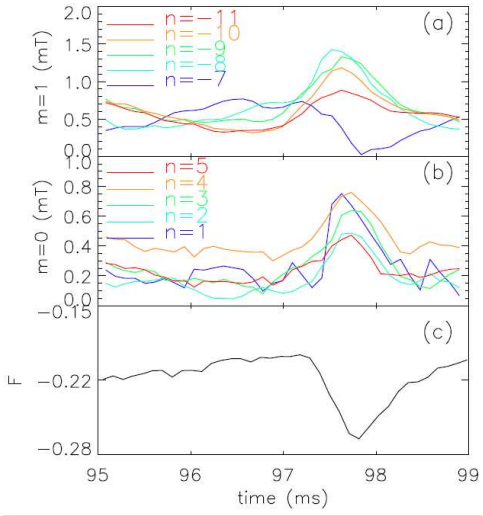

Figure 6.2: Mode dynamics during one single DRE: time trace of toroidal component of $m = 1$ modes (a), toroidal component of $m = 0$ modes(b), and reversal parameter (c).

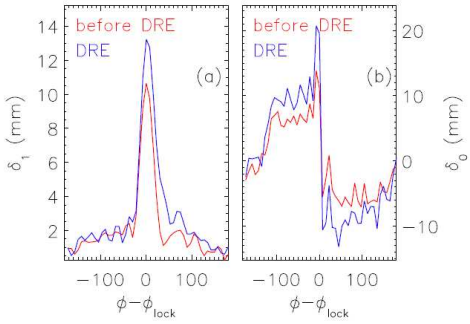

Figure 6.3: Toroidal profile of δ_1 and δ_0 deformations of the LCFS before (red) and during the DRE (blue). The DRE generates an enhanced distortion on the whole toroidal section of the plasma.

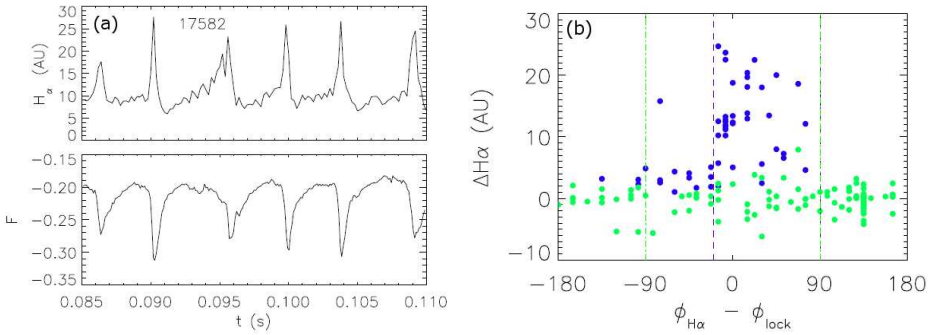

Figure 6.4: Spikes of H_α signal during the DREs, indicated by the crash of the reversal parameter (a).
ΔH_α versus $\phi_{H_\alpha} - \phi_{\text{lock}}$. The dots are blue when in the discharge at least 70% of F crashes induce H_α bursts, otherwise are green. The blue, dashed, vertical lines define the region where the highest influxes are measured (b).

not observed in all the discharges, hence the particle release is detected only in particular conditions. The difference ΔH_α between the H_α signal during and before the DRE has been evaluated for the DRE database and has been plotted in figure 6.4(b). In the graph ΔH_α has been plotted versus the distance $\phi_{H_\alpha} - \phi_{\text{lock}}$ between the toroidal position of the H_α detector and of the LM. In the picture the dots are blue when in the discharge at least 70% of F crashes induce H_α bursts, otherwise the green color is used. The graph shows that ΔH_α has a dependence on the locking position. During the F crashes increased particle influxes, represented by the blue dots in the graph, are measured in the region $-90 \lesssim \phi_{H_\alpha} - \phi_{\text{lock}} \lesssim 90$, defined by the green dashed-dotted vertical lines. Furthermore ΔH_α presents a left-right asymmetry with respect ϕ_{lock}: particularly high values (ΔH_α ¿ 10 in the

units of the graph) are measured only if $-20 \lesssim \phi_{H_\alpha} - \phi_{\rm lock} \lesssim 90$ while, if $-90 \lesssim \phi_{H_\alpha} - \phi_{\rm lock} \lesssim -20$, H_α is still correlated with the reversal parameter but lower values of ΔH_α are measured.

Looking at the distortion of the LCFS owing to the LM (figures 1.11 and 6.3), it emerges that the region of the LM ($\delta_1 > 0$ at $|\phi_{H_\alpha} - \phi_{\rm lock}| < 20$) is characterized by high values of ΔH_α. This is in agreement with the fact that during a DRE the deformation of the plasma column, and therefore the plasma-wall interaction as well, are enhanced in the LM region. The wall reacts desorbing an enhanced amount of neutral particles. The left-right asymmetry with respect to $\phi_{\rm lock}$, shown in figure 6.4(b), is likely to be related to the analogous asymmetry of the plasma radius deformation δ_0. We did not study this phenomenon in detail, hence we can only make some hypothesis concerning the influence of the plasma radius on ΔH_α. High values of ΔH_α are not only observed where $\delta_1 > 0$, but also at $20 < \phi_{H_\alpha} - \phi_{\rm lock} < 90$, where $\delta_1 \simeq 0$ and the plasma column is shrunk ($\delta_0 < 0$). An explanation can be found in the presence of the thick scrape-off layer, that allows the neutral particles (desorbed at the LM position where the power outflux is collected by the wall) to diffuse in this region before being ionized. Lower values of ΔH_α are instead measured at $-90 < \phi_{H_\alpha} - \phi_{\rm lock} < -20$, where $\delta_1 \simeq 0$ and the plasma column is enlarged ($\delta_0 > 0$). These influxes can be attributed to the particle losses due to the finite Larmor radius; these losses during the DRE are expected to be enhanced since the plasma radius in this region increases, as shown in figure 6.4(b).

6.3 Evolution of the electron density profile during the DRE.

During a DRE the electron density n_e generally increases: figure 6.5(a) shows a typical example of a negative correlation between the time trace of n_e and of the reversal parameter F. The density data are relative to the outermost chord (normalized impact parameter $h/a = 0.74$) of the interferometer, which is the chord where the density variation during the F crashes is more evident. However there are also cases where the density at the interferometer does not exhibit any particular behaviour related to the discrete dynamo events i.e. n_e is substantially unaffected. On the other hand there are a few discharges where the density decreases during the DRE: an example is shown in the graphs of the figure 6.5(b). Analogously to what done in section 6.2, the difference Δn_e between density during and before the DRE has been evaluated for the DRE database and has been plotted in figure 6.6. In this graph the green color is used if there is no correlation between the DRE and the density, while the blue and the red color highlight that the F crash is associated respectively to an increase ($\Delta n > 0$) or to a decrease of n_e ($\Delta n < 0$). The graph shows that the density increase during the DRE is not toroidally symmetric. The highest density peaks are observed at $0 \lesssim (\phi - \phi_{\rm lock} \lesssim 100$, in agreement with the fact that this is a region where

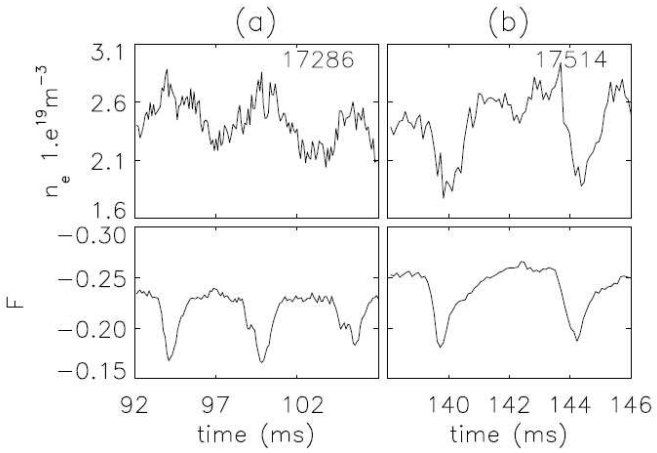

Figure 6.5: Times traces of the electron density n_e and of reversal parameter F: example of negative (discharge 17286) and of positive (discharge 17514) correlation between F and n_e. The density data are measured by the outermost chord.

high neutral influxes are observed during the DRE. Typically the density increases also in the rest of the plasma column; due to the toroidal transport this increase occurs also where the influx is not affected by the DRE. An interesting feature is that the density crashes are only observed in the proximity of the locked mode and that in the region $|\phi - \phi_{\rm lock}| \lesssim 30°$ the density peaks are observed only rarely, despite the large influxes. Hence in this region the occurrence of a DRE is accompanied by a particle loss that often balances, but sometimes even overcomes, the enhanced particle influx. In other words the results shown in figure 6.6 imply that local, non-axisymmetric transport phenomena are at work during the DREs. Figure 6.7 shows an example of the evolution of the local density profile during a DRE in the case of a density increase (shot 17286,$(\phi_{\rm interf} - \phi_{\rm lock}) \simeq -160$) and of a density crash (17514,$(\phi_{\rm interf} - \phi_{\rm lock}) \simeq -20$). In the former case the density profile, which is typically flat in the core and has the maximum value in the outer region [49], becomes even more hollow. During the DRE in fact the density increases mainly in the outer region of the plasma ($r/a \gtrsim 0.75$), in agreement with the picture of an additional particle source located at the edge. Neutral particles desorbed by the wall do not reach the plasma core since their penetration depth is about 5 cm, hence the particle source is localized at the plasma edge ($r/a \gtrsim 0.9$), as shown in [54]. Also in the case of a density crash the profile modification affects essentially the outer region of the plasma, where the outer peak that characterizes the density profile is substantially reduced resulting in the observed density decrease. In some cases the peak disappears, hence the profile flattens in the region $r/a \gtrsim 0.75$ as shown in figure 6.7. The picture suggested by these data is

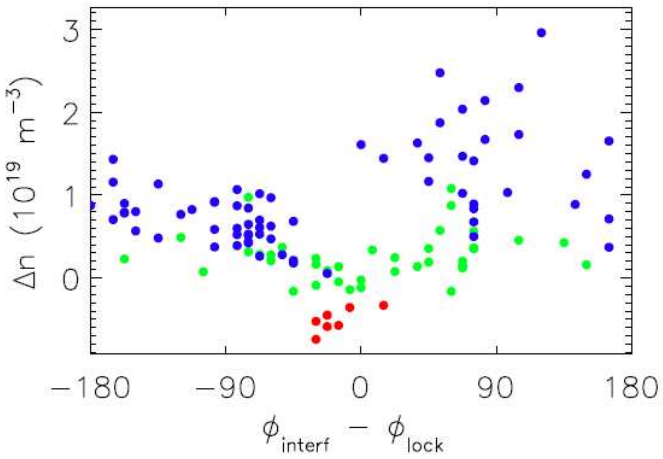

Figure 6.6: Difference Δn_e between the electron density during and before the DRE versus the toroidal distance between the locked mode and the interferometer. The blue dots indicates a negative correlation between Δn_e and F, the red a positive one, while the green means that there is no correlation.

that, at $\phi \simeq \phi_{\text{lock}}$, the DRE modifies the topology of the magnetic field in the region of the density peak ($r/a \gtrsim 0.75$). To explain the local particle loss we expect that, with respect to the pre-crash situation, an increased number of magnetic lines leaves the region of density peak and hits the wall, that acts as a sink of particles. In this way during the DRE an additional loss channel is created along the direction parallel to the magnetic field, that can explain the local enhanced particle loss and the flattening of the density profile.

6.4 Modification of the magnetic topology of the plasma edge by a DRE

The effect of the DRE on the magnetic topology has been investigated by means of the field line tracing code FLiT, presented in paragraph 3.2.4. The spectrum used in the computation includes the $m = 0$ modes with toroidal number $1 < n < 20$, and the internally resonant $m = 1$ modes with toroidal number $-20 < n < -1$. The main features of RFX-mod magnetic topology are shown in figure 6.8 by the Poincarè plot in the plane (r, ϕ) relative to the discharge 17514 at t=96 ms, far from the dynamo crash. The colors indicate the radial position of the starting point of the magnetic lines, gradually changing from dark blue for the innermost ones to red for the outermost ones. In that picture, the stochastization of the core of the plasma owing to the presence of MHD modes, is clearly visible:

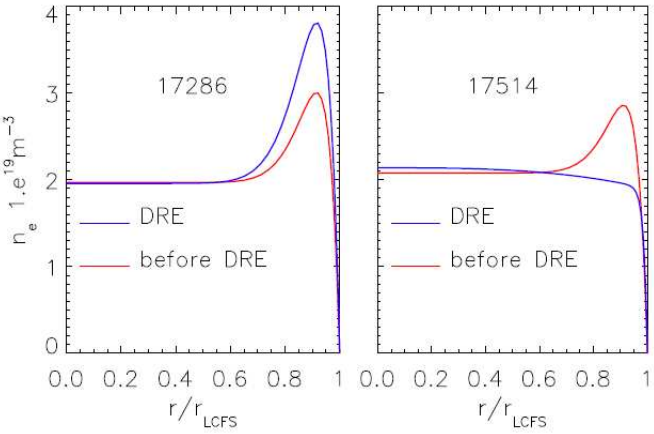

Figure 6.7: Evolution of density profiles during a DRE; example of a density increase (discharge 17286) and of a crash (discharge 17514).

several mode resonances inside the region of the reversal radius lead to the stochastization of the magnetic field. The volume up to $r \leq 0.33$ m (that is the resonance radius of the outermost $m = 1$ mode) is filled ergodically by the magnetic lines. The color of the lines whose starting point is in this region ranges from dark blue to light blue: since each line fills all this volume the colors are mixed and the volume appears to have a homogeneous color. Beyond $r \geq 0.33$ m the stochasticity of the field gradually decreases, as can be qualitatively inferred by the fact that in the plot appear regions having a dominant color, like the green region beside the chaotic one. In the region of the reversal radius, at $r \simeq 0.40$ m, the role of the $m = 0$ modes becomes dominant; this region is in fact characterized by the presence of a chain of $m = 0$ magnetic islands. The toroidal asymmetry of the island size is another effect of the particular phase relationship of the $m = 0$ modes, as has been already stated in chapter 5. The largest islands are in fact found on the left hand side of the locking mode position, indicated in the graph by the vertical line, in correspondence to the bulging of the LCFS (see chapter 5), while the smallest islands are found on the opposite side with respect to ϕ_{lock} where the plasma column is shrunk. The chaoticity of the magnetic lines due to the internally resonant modes disappears in the edge region, where good conserved magnetic surfaces (the red ones in the plot) are present. The phase locking of m=1 and m=0 modes deforms the magnetic surfaces of the non-stochastic layer formed by the m=0 island chain and by the conserved surfaces at the edge. The deformation is so strong that the outermost magnetic surfaces hit the wall in proximity of the LM. In figure 6.8 the thick red line, whose average radius is about 0.43 m, is the line which is tangent to the wall. The magnetic surfaces lying beyond

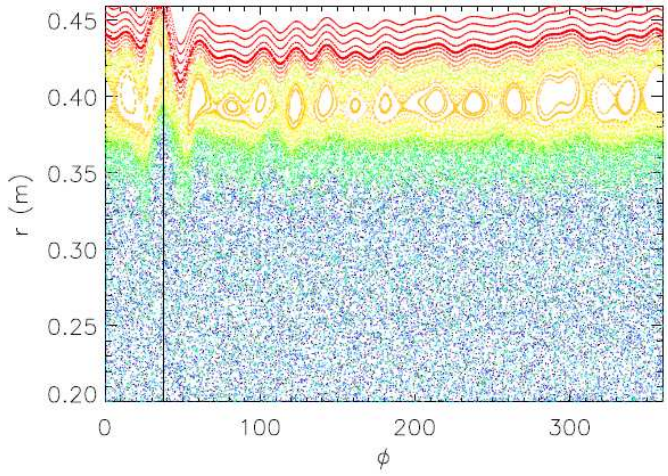

Figure 6.8: Magnetic topology of RFX-mod before the DRE: the stochastic magnetic field in central area of the torus and the characteristic $m = 0$ island chain are represented. The black line shows the position of the LM.

it, that are drawn in red as well but more spaced than the lines lying on the other side of the thick line, intercept the wall. According to this picture the chaotic magnetic lines of the plasma core do not go beyond the region of the $m = 0$ islands. This can be seen in detail in the plot 6.9(a): this is the Poincarè plot for the shot 17514 at t=96 ms obtained following magnetic lines with initial radius $r \leq 0.36$ m. Hence far from the dynamo crashes, only the edge is connected with the wall. The increase of the magnetic mode amplitude during the Dynamo Relaxation Event modifies several aspects of the magnetic topology. The relevant effect for the understanding of the the density behaviour is the modification of the interaction between the plasma and the wall. While, as shown before, between the crashes only the plasma edge is connected to the wall, during the crash the interaction with the wall involves, in the region of the LM, even more internal plasma regions. A typical example is given in figure 6.9(b) by the Poincarè plot of the shot 17514 during the crash at t=97.7 ms. The starting radius of the magnetic lines is in this case located even more internal ($r \leq 0.33$ m) than in the previous case. The plot shows that during a DRE a hole opens in the non-stochastic layer. Several lines are captured by this hole at the toroidal region of the LM (highlighted in Grey in the plot) and reach the wall after crossing the region of the density gradient (cfr. figure 6.5). Thus during the DRE the gradient region at ϕ_{lock} is connected to the wall with a connection length of about 10 m. Since in the outer region of an RFP the magnetic field is mainly poloidal, this length corresponds to some poloidal revolutions and to about 30 toroidal degrees. Hence the particle loss affects a region localized

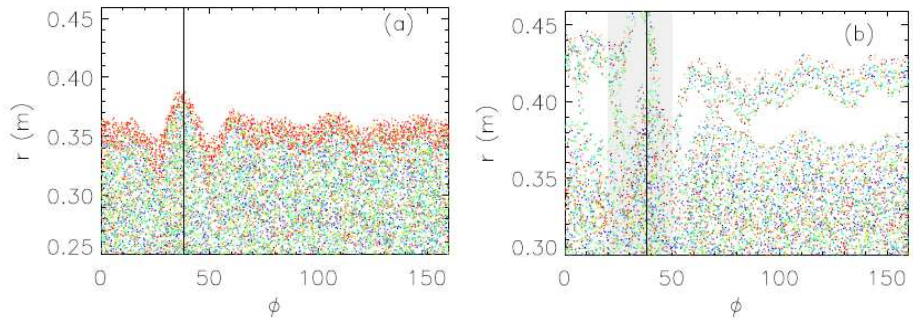

Figure 6.9: (a) Poincarè plot of the magnetic field lines in the (r, ϕ) plane relative to the discharge 17514 at t=96 ms, far from the dynamo crash. The vertical black line indicates the position of the LM.
(b) Poincarè plot of the magnetic field lines in the (r, ϕ) plane relative to the discharge 17514 at t=97.7 ms, during the dynamo crash. The Grey area highlights the toroidal region where the lines are connected to the wall.

in the toroidal direction. Furthermore a fast smoothing along the toroidal direction is hindered not only by the direction of the magnetic field, which as said before is mainly poloidal, but also by the presence of the $m = 0$ islands that are located in the gradient region. It is worth noting that the m=0 islands do not appear in figure 6.9(b), because the magnetic lines whose stating radius is outside the islands cannot enter them. Even though the DRE breaks somewhere the island chain (the aforementioned hole at ϕ_{lock} is an example of it) this structure survives during the DRE, as it is shown by the empty region in 6.9(b) between the core and the external magnetic lines.

It is interesting underline that, even though the phenomenology described in chapter 5 (the transport toroidal asymmetry owing to $m = 0$ phasing) is different from that presented in this chapter, both analysis show that the asymmetry is observed in the gradient region, enforcing the idea that the peculiar magnetic topology prevents in this region a fast toroidal transport.

The comparison between the magnetic topology before (see figure 6.8 and 6.9(a)) and during the DRE (see figure 6.9(b)) highlights another effect of the DRE that, even though it is not related to the phenomena presented in the analysis, it is anyway interesting and will be the subject of future work. Contrary to what happens far from the DRE, the external magnetic surfaces are not anymore conserved during the DRE. Since the harmonics used in the field line tracing are internally resonant, this is due to non-linear effects included in the computation. It can be seen that the non-linear coupling between the $m = 0$ and $m = 1$, $n < 0$ modes generate $m = 1$, $n > 0$

harmonics. The amplitude of these harmonics depends on the amplitude of the parent harmonics, thus it is higher during the DRE. Furthermore, due to the equilibrium change, more harmonics become resonant and the overlapping of their magnetic islands makes the external lines become slightly stochastic.

CHAPTER 7

Conclusion and future perspective.

7.1 Summary and experimental results

The RFP magnetic configuration is sustained by the *dynamo* mechanism that regenerates the toroidal flux lost through the resistive diffusion. The dynamo process is due to the interaction between magnetic and velocity perturbations. Hence the magnetic perturbations, also dubbed MHD modes, are unavoidable in RFP experiment and destroy the magnetic surfaces that guarantee the plasma confinement. Moreover the magnetic perturbations lead to a distortion of the whole plasma column, with a particularly strong toroidal localized deformation, the Locked Mode. The LM brings the plasma to collide with the first wall, with high heat and particle flux that influences the particle confinement via direct losses or indirect causes like the impurity influx. For these reasons, the particle transport in magnetic fusion devices is strongly influenced by the presence of MHD modes.

This thesis reports the analysis performed on particles confinement properties of two different Reversed Field Pinch experiments: RFX-mod and TPE-RX sited respectively in Padua, Italy and in Tsukuba, Japan. The density data have been collected by means of MIR interferometers, vibrations compensated by the two-color technique. The interferometric measurement is a reliable and not perturbing technique largely used in fusion plasma device to know the electron density with high temporal resolution.

Two kind of analyses have been carried out: the first on TPE-RX data aimed at evaluating the transport properties in discharges where the new six banks PPCD system is used, using the transport model developed at RFX (on the basis of the Rechester and Rosenbluth theory), detailed in point *a*. The second one studies the effect of LM in RFX-mod VS experiment, analyzing the density profile with respect to the distance from the LM position (point *b*) and the plasma behaviour when a DRE occurs (point *c*). The result of the performed analyses can be summarized as follow:

a) The PPCD technique, reducing the MHD perturbations, brings the plasma in a good confinement regime. During the PPCD, higher electron temperature, density increase and particle influx decrease have been observed. Moreover the LM structure almost disappears as highlighted by the strong reduction of asymmetry in toroidal influx. All these ingredients indicate that a higher particle confinement time characterizes the PPCD discharges with respect to the standard regime. This is confirmed by the calculation of the upper limit for the τ_p performed considering the presence of Molybdenum impurity.

   Furthermore for the first time a particle transport analysis has been carried on standard and PPCD pulses at TPE-RX. In standard discharges the core of the plasma is characterized by high stochasticity level and the confinement is mainly provided by the unperturbed surface outside the reversal radius. In PPCD discharges the damping of $m = 1$ dynamo modes heals the chaos in the centre and the confining region extends inward: the central diffusion coefficient is reduced by a factor 10 with respect to standard value.

   The particle confinement properties have been analyzed also during pellet injection experiments: the global perturbation to the discharge due to the pellet does not destroy the good regime induced by the PPCD. The electron density stabilizes at a value three times higher than in the standard pulse: most of the particles ablated from the pellet are confined inside the plasma up to the end of the discharge. The τ_p is lower than in PPCD pulses with no pellet injected but is still almost twice the standard confinement time of standard discharge.

b) The new saddle coils system installed at RFX-mod is aimed at damping the radial magnetic fields at the edge. The consequent better magnetic boundary, reducing the distortion of the plasma column, leads to longer and better performing plasma discharges. Because of the geometry of the system, a residual deformation of the LCFS is still present. In particular the VS is more effective on $m = 1$ mode than on $m = 0$, highlighting the $m = 0$, $n = 1$ distortion of the LCFS due to the $m = 0$ phasing. Hence, in VS pulses, it has been possible to identify two wide toroidal region of about $100°$. In one region the plasma is bulging and in the other the column is shrunk. The shrunk region is characterized by milder density gradient and higher magnetic and density high frequency fluctuations: both are sign of enhanced transport. Moreover the power spectra of the fluctuations in the shrunk region show a plateau at $\sim 6\,\mathrm{kHz}$ that can be interpreted has the sign that an instability is acting in the shrunk zone, degrading the local confinement properties.

   With this analysis the first experimental evidence of asymmetric par-

ticle transport properties owing to LM has been found.

c) The dynamo in VS RFX-mod discharges has a discrete nature: the regeneration of the toroidal flux is followed by period of relative quiet MHD activity. During the DREs an enhanced transport is observed. The electron density behaviour highlighted that also the transport enhancement associated to DREs has a local, non-axisymmetric nature. During the DRE a particularly enhanced particle loss is observed in the region of the Locked Mode. In a toroidal region of about 60 degrees centered at the LM position, despite a strong enhancement of the particle influx, the density does not increase and in some cases even decreases. This non-axisymmetric behaviour is related to the phase-locking of the MHD modes, that strengthens during DREs. In the pre-crash phase the stochastic region in the plasma core is surrounded by a layer of conserved flux surfaces and a chain of m=0 islands, where the density gradients develop. The situation changes during the crash: several magnetic lines from the core punch through the density gradient region and are diverted towards the wall through 'holes' which open at LM position.

   The application of the VS in RFX-mod leads to a decrease of the mode amplitude that prevents the formation of the holes. The plasma core and the edge are generally separated and enter in contact only in correspondence of the DREs.

7.2 Concluding remarks and future perspective

In this thesis we showed that the magnetic perturbations to the equilibrium magnetic field of the RFP configuration enhance the particle transport. The analyses have been carried out studying the evolution of the density:

$$\frac{\partial n}{\partial t} = -\nabla \cdot \Gamma + S$$

Two actors contribute to the density evolution: the internal flux Γ owing to the transport mechanisms acting in the plasma and the particle source S. The first term Γ is strongly related to the magnetic topology of the configuration i.e. to the presence of conserved magnetic surfaces that confine the charged particles, whereas the second term depends essentially on capability of the first wall of absorbing the particles outflux, if no extra particle source are provided (e.g. pellet, gas puffing, plasma gun, etc.) .

Future works will be aimed to study advanced magnetic regime obtained when a single mode grows in the plasma: the so-called *Quasi Single Helicity* regime (QSH). This regime is characterized by a helical distortion of the plasma column with conserved helical magnetic surfaces. Moreover a recent work [76] has demonstrated that the VS in high current discharges with

OPCD [77] induces the transition to a new magnetic topology (theoretical predicted in [78]), characterized by a QSH state with a single helical magnetic axis, dubbed Single Helical aXis (SHeX). The SHeX topology provides magnetic chaos healing and enhanced thermal content of the plasma. The understanding of particle confinement properties of these advanced regimes will be carried out in the future. In particular, since the good confinement region will be close to the plasma centre, i.e. far from the particle source, an active control of the central S term will be needed: the pellet injection technique will provide particle source in the plasma core. The idea is to inject a known quantity of matter inside the confining structure and study the confinement time. Preliminary studies have already been performed with TED and they show that most of the particle ablated should be confined inside the structure for time longer the usual RFX-mod particle confinement time. In this type of discharge the density profile would be poloidally asymmetric: the confining structure is not homogeneous in the poloidal cross section. The present inversion code assumes symmetric 1D profiles, for this reason the developing of a new 2D density reconstruction code has already been started.

To perform detailed transport analyses one would control both terms in the density continuity equation: the flux, via the magnetic topology, and the source term. As already stated the central S can be provided by pellet injection. The edge source is slightly more complicated: it depends on the particle outflux and on the condition of the first wall. To this end, a more performing first wall conditioning technique will be implemented at RFX-mod: encouraging results have been obtained in many tokamak [79, 80] using Lithium. Indeed first wall covered by some monolayers of Lithium presents a low recycling, reducing the S term from the wall, hence highlighting the effects of the magnetic configuration.

List of Figures

Bibliography

[1] `http://www.iter.org`.

[2] `http://www.fusion-eur.org`.

[3] R.J. Goldston and P.H. Rutherford. ***Introduction to Plasma Physics***. Institute of Physics, 1995.

[4] J.D.Lawson. **Some criteria for a power producing thermonuclear reactor**. In *Proc. Phys. Soc. B*, volume 70, 1957.

[5] H.A.B.Bodin. **The Reversed Field Pinch**. *Nuclear Fusion*, 30(9):1717–1737, 1990.

[6] Jeffrey P. Freidberg. ***Plasma Physics and Fusion Energy***. Cambridge Press, 2007.

[7] Harold P. Furth, John Killeen, and Marshall N. Rosenbluth. **Finite-Resistivity Instabilities of a Sheet Pinch**. *Physics of Fluids*, 6(4):459–484, 1963.

[8] J.Wesson. ***Tokamaks***. Claredon Press, 1987.

[9] S. Ortolani and D.D. Schnack. ***Magnetohydrodynamics of Plasma Relaxation***. World Scientific, Singapore, 1993.

[10] J. B.Taylor. **Relaxation of Toroidal Plasma and Generation of Reverse Magnetic Field**. *Phys. Rev. Lett.*, 33(19):1139–1141, 1974.

[11] Teruo Tamano, Wayne D. Bard, Cheng Chu, Yoshiomi Kondoh, Robert J. La Haye, Paul Ss Lee, Milton Saito, Michael Jj Schaffer, and Peter Ll Taylor. **Observation of a new toroidally localized kink mode and its role in Reversed Field Pinch plasmas**. *Phys. Rev. Lett.*, 59(13):1444, Sep 1987.

[12] R. Bartiromo and RFX team. **Recent progress in reversed field pinch research in the RFX experiment**. *Nuclear Fusion*, 39(11Y):1697–1705, 1999.

[13] P Zanca and S Martini. **m = 0 perturbations of the magnetic surfaces in an RFP**. *Plasma Physics and Controlled Fusion*, 43(2):121–135, 2001.

[14] H. Ji, A. F. Almagri, S. C. Prager, and J. S. Sarff. **Time-Resolved Observation of Discrete and Continuous Magnetohydrodynamic Dynamo in the Reversed-Field Pinch Edge**. *Phys. Rev. Lett.*, 73(5):668–671, Aug 1994.

[15] P.R. Brusnell. **Initial Result from the Rebuilt EXTRAP-T2R RFP Device**. *Plasma Phys. and Control. Fusion*, 43:1457–1470, 2001.

[16] R. Dexter, D. Kerst, T. Lovell, S. Prager, and J. Sprott. **The Madison Symmetric Torus**. *Fusion Technol.*, 19:131, 1991.

[17] Y. Yagi, S. Sekine, H. Sakakita, H. Koguchi, K. Hayase, Y. Hirano, I. Hirota, S. Kiyama, Y. Maejima, Y. Sato, T. Shimada, and K. Sugisaki. **Design concept and confinement prediction of TPE-RX reversed-field pinch device**. *Fusion Engineering and Design*, 45(4):409, 1999.

[18] P. Sonato, G. Chitarin, P. Zaccaria, F. Gnesotto, S. Ortolani, A. Buffa, M. Bagatin, W.R. Baker, S. Dal Bello, P. Fiorentin, L. Grando, G. Marchiori, D. Marcuzzi, A. Masiello, S. Peruzzo, N. Pomaro, and G. Serianni. **Machine modification for active MHD control in RFX**. *Fusion Engineering and Design*, 66:161, 2003.

[19] G.Rostagni. **RFX: an expected step in RFP research**. *Fusion Engineering and Design*, 25:301–313, 1995.

[20] A. Alfier and R. Pasqualotto. **New Thomson scattering diagnostic on RFX-mod**. *Review of Scientific Instruments*, 78(1):013505, 2007.

[21] P. Innocente and S. Martini. **A two color multichord infrared interferometer for RFX**. In *Proceedings of the 9th topical conference on high temperature plasma diagnostics*, volume 63, pages 4996–4998. AIP, 1992.

[22] P. Innocente, S. Martini, A. Canton, and L. Tasinato. **Upgrade of the RFX CO_2 interferometer using in-vessel optics for extended edge resolution**. In *Proceedings of the eleventh topical conference on high temperature plasma diagnostics*, volume 68, pages 694–697. AIP, 1997.

[23] L. Carraro, E. Casarotto, R. Pasqualotto, M.E. Puiatti, F. Sattin, and P. Scarin. **Impurity influx studies in the RFX reversed field pinch**. *Journal of Nuclear Materials*, 220 - 222:646 – 649, 1995.

[24] G. Serianni, T. Bolzonella, R. Cavazzana, G. Marchiori, N. Pomaro, L. Lotto, M. Monari, and C. Taliercio. **Development, tests, and data acquisition of the integrated system of internal sensors for RFX**. *Review of Scientific Instruments*, 75(10):4338–4340, 2004.

[25] Andrea Murari, Paolo Franz, Luca Zabeo, Rosario Bartiromo, Lorella Carraro, Gianni Gadani, Lionello Marrelli, Piero Martin, Roberto Pasqualotto, and Marco Valisa. **An optimized multifoil soft x-ray spectrometer for the determination of the electron temperature with high time resolution**. *Rev. Sci. Instrum.*, 70(1):581, 1999.

[26] Paolo Franz, Lionello Marrelli, Andrea Murari, Gianluca Spizzo, and Piero Martin. **Soft X ray tomographic imaging in the RFX reversed field pinch**. *Nucl. Fusion*, 41(6):695, 2001.

[27] A.Canton, Y.Hirano, P.Innocente, H.Koguchi, H.Sakakita, S.Sekine, T.Shimada, and Y.Yagi. **Analysis of the Behaviour of Electron Density in the TPE-RX Reversed Field Pinch and Comparison with RFX**. In *28th EPS Conference on Plasma Phys.*, number p1.034 in 25C, 18 - 22 June 2001.

[28] H. Koguchi, T. Shimada, T. Asai, Y. Yagi, Y. Hirano, and H. Sakakita. **Soft x-ray tomography system for the toroidal pinch experiment-RX reversed-field pinch**. *Review of Scientific Instruments*, 75(10):4004–4006, 2004.

[29] Y. Yagi et al. *Bull. Electrotech. Lab.*, 53:270, 1988. (in Japanese).

[30] J. Sheffield. **The physics of magnetic fusion reactors**. *Rev.Mod.Phys.*, 66(3):1015–1103, 1994.

[31] A.B. Rechester and M.N. Rosenbluth. **Electron heat transport in a tokamak with destroyed magnetic surfaces**. *Phys.Rev.Lett.*, 40(1):38–41, 1978.

[32] Harvey, R. W., McCoy, M. G., Hsu, J. Y., Mirin, and A. A. **Electron Dynamics Associated with Stochastic Magnetic and Ambipolar Electric Fields**. *Phys. Rev. Lett.*, 47(2):102–105, Jul 1981.

[33] D. Gregoratto, L. Garzotti, P. Innocente, S. Martini, and A. Canton. **A Behaviour of Electron Density Profiles and Particle Transport Analysis in the RFX Reversed Field Pinch**. *Nuclear Fusion*, 38(8):1199–1213, 1998.

[34] Thomas H. Stix. **Magnetic Braiding in a Toroidal Plasma**. *Phys. Rev. Lett.*, 30(18):833–835, Apr 1973.

[35] F. D'Angelo and R. Paccagnella. The stochastic diffusion process in reversed-field pinch. *Phys.Plasmas*, 3(6):2353–2364, 1996.

[36] J. S. Sarff, S. A. Hokin, H. Ji, S. C. Prager, and C. R. Sovinec. **Fluctuation and transport reduction in a reversed field pinch by inductive poloidal current drive**. *Phys. Rev. Lett.*, 72(23):3670–3673, Jun 1994.

[37] B. E. Chapman, A. F. Almagri, J. K. Anderson, T. M. Biewer, P. K. Chattopadhyay, C.-S. Chiang, D. Craig, D. J. Den Hartog, G. Fiksel, C. B. Forest, A. K. Hansen, D. Holly, N. E. Lanier, R. O'Connell, S. C. Prager, J. C. Reardon, J. S. Sarff, M. D. Wyman, D. L. Brower, W. X. Ding, Y. Jiang, S. D. Terry, P. Franz, L. Marrelli, and P. Martin. **High confinement plasmas in the Madison Symmetric Torus reversed-field pinch**. *Phys.Plasmas*, 9(5):2061–2068, 2002.

[38] R. Bartiromo, P. Martin, S. Martini, T. Bolzonella, A. Canton, P. Innocente, L. Marrelli, A. Murari, and R. Pasqualotto. **Core Transport Improvement during Poloidal Current Drive in the RFX Reversed Field Pinch**. *Phys. Rev. Lett.*, 82(7):1462–1465, Feb 1999.

[39] Y. Yagi, H. Koguchi, Y. Hirano, T. Shimada, H. Sakakita, S. Sekine, B. E. Chapman, and J. S. Sarff. **Increased confinement improvement in a reversed-field pinch using double-pulsed poloidal current drive**. *Phys.Plasmas*, 10(7):2925–2931, 2003.

[40] L. Marrelli, A.Alfier, T. Bolzonella, F. Bonomo, P. Franz, G. Manduchi M. Gobbin, G. Marchiori, P.Martin, R.Pasqualotto, P.Piovesan, and G.Spizzo. **Experiments of active control of internal resistive MHD modes in RFX-mod**. In *33rd EPS Conference on Plasma Phys.*, number p5.092 in 30I, 19 – 23 June 2006.

[41] Paolo Zanca, Lionello Marrelli, Gabriele Manduchi, and Giuseppe Marchiori. **Beyond the intelligent shell concept: the clean-mode-control**. *Nuclear Fusion*, 47(11):1425–1436, 2007.

[42] S.L. Milora, W.A. Houlberg, L.L. Lengyel, and V. Mertens. **Pellet fuelling**. *Nuclear Fusion*, 35(6):657–754, 1995.

[43] P. B. Parks and R. J. Turnbull. **Effect of transonic flow in the ablation cloud on the lifetime of a solid hydrogen pellet in a plasma**. *Phys. Fluids*, 21:1735–1741, 1978.

[44] B. Pegourie, J.-M. Picchiottino, H.-W. Drawin, A. Geraud, and M. Chatelier. **Pellet ablation studies on TORE SUPRA**. *Nuclear Fusion*, 33(4):591–600, 1993.

[45] L.R. Baylor, A. Geraud, W.A. Houlberg, D. Frigione, M. Gadeberg, T.C. Jernigan, J. De Kloe, P. Kupschus, B.V. Kuteev, P. Lang, A.A.M. Oomens, A.L. Qualls, K.N. Sato, and G.L. Schmidt. **An international pellet ablation database**. *Nuclear Fusion*, 37(4):445–50, 1997.

[46] M. A. Heald and C. B. Warton. ***Plasma Diagnostic with Microwaves***. Wiley, New York, 1965.

[47] P. Innocente, S. Martini, and A. Schio. **Development of a Vibration-compensated Interferometer for the RFX experiment**. *Review of Scientific Instruments*, 61:2885, 1990.

[48] A.Canton, R.Lorenzini, F.Auriemma, L.Carraro, P.Innocente, and S.Martini. **Density profiles and particle confinement in the modified RFX Reversed Field Pinch**. In *32nd EPS Conference on Plasma Phys.*, number p4.027 in 29C, 27 June – 1 July 2005.

[49] R. Lorenzini, D. Terranova, F. Auriemma, R. Cavazzana, P. Innocente, S. Martini, G. Serianni, and M. Zuin. **Toroidally asymmetric particle transport caused by phase-locking of MHD modes in RFX-mod**. *Nuclear Fusion*, 47(11):1468–1475, 2007.

[50] A. Canton, Y. Hirano, P. Innocente, H. Koguchi, and R. Lorenzini. **Electron density behaviour in the TPE-RX reversed field pinch experiment and comparison with the particle transport model of the RFX experiment**. *Plasma Phys. Control. Fusion*, 46, 2004.

[51] R. Lorenzini, L. Garzotti, B. Pégourié, P. Innocente, and S. Martini. **Analysis and modelling of plasma response to pellet injection in RFX**. *Plasma Physics and Controlled Fusion*, 44(2):233–252, 2002.

[52] ***Atomic Data and Analysis Structure Database***, 1994. (JET Joint Undertaking Report, JET-IR(94)-06).

[53] K.L. Bell et al. **Recommended Data on the Electron Impact Ionization of Light Atoms and Ions**. *Journal of Physical and Chemical Reference Data*, 12:891, 1983.

[54] R. Lorenzini and F. Auriemma and A. Canton and L. Carraro. **Particle transport in reversed field pinch helium plasmas**. *Physics of Plasmas*, 13(11), 2006.

[55] M.H. Hughes and D.E. Post. **A Monte Carlo Algorithm for Calculating Neutral Gas Transport in Cylindrical Plasma**. *Journal of Computational Physics*, 28:43–55, 1978.

[56] Atomic Data for Fusion, editor. ***Collision of H, H_2, He and Li Atoms and Ions with Atoms and Molecules***, volume 1. C.F. Barnet, 1990.

[57] J. P. Biersack and L. G. Haggmark. **A Monte Carlo computer program for the transport of energetic ions in amorphous targets**. *Nucl. Instrum. Methods*, 174:257, 1980.

[58] Paolo Zanca and David Terranova. **Reconstruction of the magnetic perturbation in a toroidal reversed field pinch**. *Plasma Physics and Controlled Fusion*, 46(7):1115–1141, 2004.

[59] P. Innocente, A. Canton, R. Lorenzini, D. Terranova, A. Alfier, E. Martines, F. Bonomo, and R. Pasqualotto. **Particles and energy stochastic transport in the RFX-mod reversed field pinch experiment**. In *34th EPS Conference on Plasma Phys.*, number p2.051 in 31F, 2 – 6 July 2007.

[60] M. Giubbilei, P. Martin, and S. Ortolani. **A Mechanism for Plasma Heating in Driven Relaxing Magnetic Field Configuration**. *Plasma Phys. Control. Fusion*, 34(5):405–411, 1990.

[61] L.Carraro, S.Costa, M.E.Puiatti, F.Sattin, P.Scarin, and M.Valisa. **Reconstruction of the radiation emitted by the intrinsic impurities in the RFX reversed field pinch**. *Plasma Phys. Control. Fusion*, 42(6):731–741, 2000.

[62] C. DeMichelis and M. Mattioli. **Spectroscopy and impurity behaviour in fusion plasmas**. *Rep.Prog.Phys.*, 47:1233, 1984.

[63] L Frassinetti, K Yambe, S Kiyama, Y Hirano, H Koguchi, and H Sakakita. **Turbulence and particle confinement in a reversed-field pinch plasma**. *Plasma Phys. Control. Fusion*, 49(3):199–209, 2007.

[64] F. Auriemma, D. Terranova, H. Koguchi, Y. Hirano, P. Innocente, S.Kiyama, R. Lorenzini, and H. Sakakita. **Interaction of pellets with plasma in standard and advanced regimes at TPE-RX reversed field pinch experiment**. In *34th EPS Conference on Plasma Phys.*, number p4.156 in 31F, 2 – 6 July 2007.

[65] P. Innocente, B. Boscolo, S. Martini, and L. Garzotti. **Three-dimensional time-resolved H pellet trajectory reconstruction in RFX by position sensitive detector H_α diagnostic**. *Proceedings of the 12th topical conference on high temperature plasma diagnostics*, 70(1):943–946, 1999.

[66] P. Zanca and S. Martini. **Reconstruction of the plasma surface in a RFP in the presence of non-axisymmetric perturbations**. *Plasma Physics and Controlled Fusion*, 41(10):1251–1275, 1999.

[67] G. Spizzo, S. Cappello, A. Cravotta, D. F. Escande, I. Predebon, L. Marrelli, P. Martin, and R. B. White. **Transport Barrier inside the Reversal Surface in the Chaotic Regime of the Reversed-Field Pinch**. *Physical Review Letters*, 96(2):025001, 2006.

[68] P. Zanca and F. Sattin. **An equilibrium model for RFP plasmas in the presence of resonant tearing modes**. *Plasma Physics and Controlled Fusion*, 45(1):1–26, 2003.

[69] Lipschultz B. et al. *Nucl. Fusion*, 24:977, 1984.

[70] Valisa M. et al. In *Proc. 21st Int. Conf. on Fusion Energy*, 2006.

[71] Roca Ch.F., Innocente P., and Martini S. **Experiments of active control of internal resistive MHD modes in RFX-mod**. In *20th EPS Conference on Plasma Phys.*, 17C, 26 – 30 July 1993.

[72] N. E. Lanier, D. Craig, J. K. Anderson, T. M. Biewer, B. E. Chapman, D. J. Den Hartog, C. B. Forest, S. C. Prager, D. L. Brower, and Y. Jiang. **An investigation of density fluctuations and electron transport in the Madison Symmetric Torus reversed-field pinch**. *Physics of Plasmas*, 8(7):3402–3410, 2001.

[73] R. Lorenzini, F. Auriemma, P. Innocente, E. Martines, S. Martini, and D. Terranova. **Confinement loss during Dynamo Relaxation Event in RFX-mod**. *Plasma Phys. and Control. Fusion*, 50(3), 2008. accepted for publication.

[74] P. Innocente, T. Bolzonella, S. Cappello, and D. Terranova. **Magnetic relaxation and discrete dynamo action in RFX**. In *27th EPS Conference on Plasma Phys.*, number p4.026 in 24B, 12 - 16 June 2000.

[75] M. Valisa, T. Bolzonella, L. Carraro, E. Casarotto, S. Costa, L. Garzotti, P. Innocente, S. Martini, R. Pasqualotto, M. E. Puiatti, R. Pugno, and P. Scarin. **Locked modes induced plasma-wall interactions in RFX**. *Journal of Nuclear Materials*, 241 - 243:988–992, 1997.

[76] R. Lorenzini, D. Terranova, A. Alfier, P. Innocente, E. Martines, R. Pasqualotto, and P. Zanca. **Single helical axis states in reversed field pinch plasmas**. *Phys. Rev. Lett.*, -(-):–, -. submitted to PRL in January 2008.

[77] T. Bolzonella, P. Martin, S. Martini, L. Marrelli, R. Pasqualotto, and D. Terranova. **Quasistationary Magnetic Fluctuation Control in**

the Reversed Field Pinch: A Proof of Principle Experiment. *Phys. Rev. Lett.*, 87(19):195001, Oct 2001.

[78] D. F. Escande, R. Paccagnella, S. Cappello, C. Marchetto, and F. D'Angelo. **Chaos Healing by Separatrix Disappearance and Quasisingle Helicity States of the Reversed Field Pinch**. *Phys. Rev. Lett.*, 85(15):3169–3172, Oct 2000.

[79] J.A. Snipes, E.S. Marmar, J.L. Terry, M.G. Bell, R.V. Budny, K.W. Hill, Di. Jassby, D.K. Mansfield, D.M. Meade, H.K. Park, J.D. Strachan, B.C. Stratton, E.J. Synakowski, G. Taylor, D.N. Ruzic, and M. Shaheen. **Wall conditioning with impurity pellet injection on TFTR**. *Journal of Nuclear Materials*, 196 - 198:686 – 691, 1992.

[80] M.L. Apicella, G. Mazzitelli, V. Pericoli Ridolfini, V. Lazarev, A. Alekseyev, A. Vertkov, R. Zagórski, and FTU Team. **First experiments with lithium limiter on FTU**. *Journal of Nuclear Materials*, 363 - 365:1346 – 1351, 2007.

Acknowledgments

Acknowledgments... sarà l'ultima parola in inglese che troverete scritta in questa tesi, da adesso userò solo l'italiano, lingua che sicuramente padroneggio meglio e che decisamente è più familiare alle persone alle quali sono rivolti questi ringraziamenti. Una tesi di dottorato non è semplicemente l'ultimo atto di un periodo di formazione professionale di 3 anni ma è uno dei passaggi nel più ampio percorso della Vita. Per tale motivo dico *GRAZIE* non solo a chi è stato direttamente coinvolto nel lavoro ma anche a tutte quelle persone care con le quali ho condiviso l'Amicizia.

Per quanto riguarda la mia vita ad RFX, voglio innanzitutto ringraziare i colleghi con cui ho lavorato a più stretto contatto, dai quali sto imparando a fare ricerca: Stefano, capogruppo, tutor ed ingegnere da interpellare ogni qual volta non capivo qualcosa di fisica(!), si è letto tutta la tesi, contribuendovi con consigli preziosi. Rita, amica e collega che mi ha "preso per mano" 5 anni fa al mio arrivo ad RFX per la tesi di laurea e con la quale ho ottenuto i migliori successi professionali. David, maestro in materia di pellet ... e di cucina giapponese, a lui il merito di avermi portato per *isakaia* ad abbuffarmi di *sakè, sushi e ramen*! Paolo che ha preso da poco il timone del gruppo FC e si è già fatto apprezzare per il polso con cui ci guida. Alessandra che ha provato con tutte le sue forze a farmi diventare un po' più sperimentale... con ottimi risultati, visto da dove partivo! Oltre ai colleghi del gruppo FC, ad RFX c'è tutto un felice gruppo di amici, l'asilo (come ci chiama Gian ;-), ma solo perché conserviamo quella freschezza ed allegria che certi vecchi hanno perso!), con i quali ho avuto il privilegio di vivere gli anni di dottorato tra caffè, viaggi, gite, cene, feste, skypate e... giornate di lavoro. Federica che ci mantiene sempre sull'attenti (spero che il Fedometro segni *bel tempo* quando leggerà queste righe) che è un'amica e confidente preziosa. Gobbins, il mio punto di riferimento politico-culturale, grazie a lui ho imparato ad amare la natura incontaminata che circonda RFX e che trova la sua massima espressione nel *boschetto* (rigorosamente il lunedì, mercoledì e venerdì, poi cicca!). Il buon Takkons *L'INNNGEGGGNERE*, anche lui uno dei *boschettieri*, grazie per l'amicizia, l'affetto e per averci mostrato che si può essere sereni anche quando non tutto gira per il meglio. Magostini, cueo picoeto e spacamaroni, il mio diretto concorrente la mattina per

l'entrata ad RFX, è lui che per primo è riuscito a timbrare alle 8.59! Brombins, Pizzi, Ritu, Bigi, Luca e i follets, grazie ad ognuno di voi le giornate ad RFX non sono mai banali.

Un grande grazie alla mia famiglia, da diversi anni non sono più *in casa* ma ogni volta che torno a Thiene mi sento *a casa*! grazie per avermi sempre sostenuto ed incoraggiato, per aver gioito dei successi e confortato nelle sconfitte e perché mi avete permesso di gustare la Libertà nella vita! Grazie a Marco, fratello per nascita ma oggi vero amico, con il quale ci vediamo poco, a volte sembra che ci si perda di vista ma poi basta ritrovarsi attorno ad un tavolo (o magari su una barca a vela!!) ed è come se il tempo non fosse passato! Tra i tanti amici, voglio ringraziare Chiara e Giancarlo con le piccole Francesca e Mariachiara, per l'affetto, le cene organizzate anche all'ultimo momento, i momenti di gioco, i progetti, le ciacole... casa vostra è sempre aperta! Paolo che guida il coro come un vero maestro ma che è soprattutto il segno di un'amicizia che cresce e si solidifica nel tempo. Luca e Valentina, con i quali ho vissuto passioni divertenti (la vela, il calcetto, la Puglia, lo scooter, GP3, Assassin'S...) e progetti, come il trasferimento nelle nostre rispettive nuove case. Grazie a Pata, Venrico, Cuzo, Chain, I'rene e Endri, Moretto, Elisa e il piccolo Leo, con i quali ho condiviso gli anni dell'università e del dottorato. Un pensiero speciale per Pata che, in qualità di compagna di appartamento, mi ha sopportato in questi mesi di tesi e non solo! Dai Pata, è finita e adesso ricomincia il *tourbillon* di feste e cene...e magari riusciamo anche a mangiare insieme una o due volte (basta che poi non mi porti al cinema ;-))!! Grazie alla *ragazza del Giovedì*... Dico grazie anche a tutti i ragazzi (o meglio le ragazze) del coro del Duomo (il pollaio!!), un 'esperienza che è rinata da un paio d'anni e che diventa per me luogo di divertimento ma soprattutto di servizio "nutriente" e che solo grazie alla vostra presenza è possibile. Per tutti dico grazie a don Stefano che ci sostiene con la sua gioia ed il suo entusiasmo. Grazie a suor Silvia e suor Marta, due amiche e guide che da anni mi accompagnano con la preghiera, l'amicizia, i suggerimenti illuminati :-). Grazie agli amici e fratelli della comunità neocat. Grazie Giorgio e Judy per gli aperitivi al Barabba che si concludono sempre ben dopo cena, spesso a casa vostra (quella vecchia, ma aspettiamo quella nuova!!), per le mezz'ore rubate alla pausa pranzo, giusto per farsi due chiacchiere e aggiornarci sulla vita, per la Messa a san Massimo (quando ci riusciamo!), insomma perché siamo e resteremo amici. L'ultimo sincero grazie ad Eli, per il tempo meraviglioso passato insieme, per l'allegria e la leggerezza che ha portato nella mia vita, per essere la persona tenera avvolta da una scorza croccante (come il tronky!!) che mi sta accanto: continuiamo a crescere insieme, amore mio!

Ovviamente due paginette non sono sufficienti a dire grazie a tutte le persone che lo meriterebbero, ringrazio Dio che ci ha fatto incontrare, che ci ha messo in questo meraviglioso giardino che è Terra e che ci ha reso amici.